Measurements of the Semileptonic Decay of the Neutral Charmed Meson $D^0 \rightarrow K^- \mu^+ \nu_\mu$

by

Will E. Johns

B. S., University of Illinois , 1987

A thesis submitted to the

Faculty of the Graduate School of the

University of Colorado

in partial fulfillment of the requirements for the degree

Doctor of Philosophy

Department of Physics

1995

Johns, Will E. (Ph.D., Physics)

Measurements of the Semileptonic

Decay of the Neutral Charmed Meson $D^0 \to K^-\mu^+\nu_\mu$

Thesis directed by Professor John P. Cumalat

Measurements of the branching ratio of the neutral charmed meson in the mode $D^0 \to K^-\mu^+\nu_\mu$ relative to the modes $D^0 \to K^-\pi^+$ and $D^0 \to K^{*-}\mu^+\nu_\mu$ are presented. The form factors and pole mass governing the decay $D^0 \to K^-\mu^+\nu_\mu$ are also measured. The data used for these analyses were obtained in the Fermilab high energy photoproduction experiment E687.

We determine the D^0 branching ratios to be :

$$\frac{BR(D^0 \to K^-\mu^+\nu_\mu)}{BR(D^0 \to K^-\pi^+)} = 0.852 \pm 0.034 \text{ (statistical)} \pm 0.028 \text{ (systematic), and}$$

$$\frac{BR(D^0 \to K^{*-}\mu^+\nu_\mu)}{BR(D^0 \to K^-\mu^+\nu_\mu)} = 0.62 \pm 0.11 \text{ (statistical)} \pm 0.02 \text{ (systematic).}$$

The f_+ pole mass is measured to be

$$M_{pole} = 1.87^{+0.11}_{-0.08} \text{ (statistical)}^{+0.07}_{-0.06} \text{ (systematic)} GeV/c^2$$

and the ratio of form factors is measured to be

$$f_-/f_+ = 2.3 \pm 1.9 \text{ (statistical)} \pm 1.8 \text{ (systematic).}$$

These results represent the world's best measurement of these quantities and a 5 fold increase in statistics compared to previous measurements of this mode. Our ratios of rates agree with the old world averages of

$\frac{BR(D^0 \to K^-\mu^+\nu_\mu)}{BR(D^0 \to K^-\pi^+)} = 0.8 \pm 0.1$, $\frac{BR(D^0 \to K^-e^+\nu_e)}{BR(D^0 \to K^-\pi^+)} = 0.95 \pm 0.04$ and $\frac{BR(D^0 \to K^* l^+\nu_l)}{BR(D^0 \to K l^+\nu_l)}$ $= 0.6 \pm 0.06$. Previous measurements of the pole mass either used the information from the decay $D^0 \to K^-e^+\nu_e$ or mixed the electron and muon modes. We present a measurement of the pole mass measured exclusively using the decay $D^0 \to K^-\mu^+\nu_\mu$. Our pole mass measurement agrees with the previous best measurement of 2.00 ± 0.12 (statistical) $\pm\, 0.18$ (systematic). The ratio f_-/f_+ for the decay $D^0 \to K^-\mu^+\nu_\mu$ is measured for the first time in this thesis and is in agreement with theoretical predictions.

To generations hence.

ACKNOWLEDGMENTS

All who have touched my life deserve mention, for a man is the sum of all his experiences. I'll pay heed, as I may, to all who pop into mind this day. Bob Bertsche, Gordon Babcock, Kathy Ponelight, Dan Hagan, Larry Myers, Mike Horton, Jeff Haller, Ayhan Mertogul, Ken Gengler, Jim Bury, Arnold Ewert, the "Coach", "Whitey", Walt Harris, Sam Barone, Tom Trumpinski, Fred Cogswell, Steve Errede, Sampa Bhadra, Fred Brown, Jan Lauber, David Dargon, Don Spencer, Tom Cronk, Paul Williams, Raphael Tello, Jonathan Kofler, Barry Bruce, Gan Zhou(and the other members of the Society of the Unit Cusp). Eric, Gary, Mark, J.R., Spence, Owen, Bob, Carl, Linda, Norma, Vivian, Delores, Judy, Kathy O.(if that is your name!), Tim, Marge, Sue, Larry, Dale, Rita, Cris, Jim, Rob, Bill, and Gale.

My teachers in Graduate school: Carl Iddings, Tom Degrand, John Wahr, Jim Shepard, Paul Beale, Uriel Nauenberg and John Cumalat.

Everyone that gave cold fusion a try here at Colorado.

At Fermilab, the E687 collaboration, the PASS1 crewers, the E683 Collaboration, the Operations group, Ron Currier, Roy Justice, Margaret Votava, the Computing division, the Research Division and all the taxpayers who support us.

Mentors who have guided this work(and others): John Cumalat, Joel Butler, Jim Wiss, Luigi Moroni, Danielle Pedrini, Dario Menasce, Brian O'Reilly, Steve Culy, Vittorio Paolone, Art Kreymer, Shekhar Shukla, Harry Cheung, Carlo Dallapiccola, Matt Nehring, John Ginkel, Ray Culbertson, Derrell Durrett and Doug Johnson.

Fellow Travellers: Brian O'Reilly, Vittorio Paolone, John Cumalat, Joel Butler, Steve Culy, Matt Nehring, Byung Gu Cheon and Art Kreymer.

Confidants: Brian O'Reilly, Matt Nehring, Luca Cinquini, Carlo Dallapiccola, Jan Lauber, John Cumalat and Gary Grim.

Advisor and tireless inquisitor: John Cumalat.

Those who renewed my quest for magic in life: Susan Johns and Keesha Davis.

My strength and love, my family: Bonnie(curiosity), Jared(dedication), R. Bryan(essence), Susan(talent), Alice(heart) and attendant spouses, nieces, nephews and family no longer with us.

CONTENTS

FIGURES

Figure

TABLES

Table

CHAPTER 1

INTRODUCTION

1.1 Overview

The study of particle physics is one of reduction. We try to take complicated objects or interactions and turn them into simple ones. As an example, consider a human body.

A human being is composed mostly of water. Water is a molecule of matter that contains 2 hydrogen atoms and one oxygen atom. Each hydrogen atom is an electron and a proton. The proton is made of three quarks, and this is as far as we can go since quarks and electrons are fundamental objects. That is, we have no evidence that there are constituent objects inside the electron or the quark.

There are four fundamental forces that bind and shape the fundamental objects and their various manifestations: gravity, the weak nuclear force, electromagnetism and the strong nuclear force.

Gravity is by far the weakest force, but since we feel the gravitational force from so many objects, this force seems strong. It holds us to the earth, holds the earth about the sun and holds the sun in a spiral arm of the Milky Way.

The weak nuclear force is responsible for the carbon–14 beta decay:

$$ {}^{14}_{6}C \rightarrow {}^{14}_{7}N + e^{-} + \overline{\nu}_e \tag{1.1.1} $$

Since an organism ceases to absorb carbon–14 when it dies, we use this decay, which occurs about every 5700 years for a typical carbon–14 atom, to find out when a very old organism perished. This is accomplished by comparing the amount of carbon–14 left in the organism to the amount of the stable atom, carbon–12, in the organism, and one can count electrons from the carbon–14 decay to determine the amount of carbon–14 in the sample. The weak force is stronger than gravity, but weaker than the electromagnetic force.

The electromagnetic force is part of our everyday lives. This thesis is being written on a machine that uses electricity. Lightning is a dramatic example of the electromagnetic force, and the chemical reactions in our body are not possible without this force.

The strong nuclear force is perhaps the darkest player in this quartet. A fairly benign example of the strong force in action is a smoke detector. An atom of Americium–241 has an unstable nucleus and will emit a helium nucleus(2 protons and 2 neutrons) and become Neptunium–237. This occurs about every 50 years on the average for an atom of Americium–241. Since helium nuclei readily ionize particles in the atmosphere, any sudden decrease in the number of ionized particles coming from the helium nuclei produced by a sample of many Americium–241 atoms indicates that combustion by–products are inhibiting the ionization process. In a smoke detector the number of ionized particles is measured as a current, and a decrease in current triggers an alarm. The strong force is used to generate nuclear power through uranium fission and used to make nuclear weapons.

Of these forces, the most accessible for laboratory studies is the electromagnetic force. We use it to measure and record the effects of all the other forces. The model of the interactions resulting from this force, Quantum Electrodynamics, is very accurate. It is the basis of the models for all the other forces except gravity. Gravity still eludes a successful quantum description.

We use the word quantum when a discrete particle, or quantum, is exchanged in a process. For the electromagnetic force the quanta is a photon(light), the weak force exchanges 3 massive quanta, the W^+,the W^- and the Z^0 particle and the strong force exchanges gluons. The photon is experimentally known to be essentially massless. The gluon is expected to be massless, but experiment has not ruled out a mass of a few MeV or less for this particle.

The particles that interact only via the weak and electromagnetic force are called leptons. The electron(e^-) is the most recognizable of these particles. Five leptons are known to exist and the sixth(ν_τ) will almost certainly be discovered within the next 20 years. We arrange the leptons in three families, each with a charged particle and a neutrino(ν) partner:

$$\begin{pmatrix} \nu_e \\ e^- \end{pmatrix}, \begin{pmatrix} \nu_\mu \\ \mu^- \end{pmatrix}, \begin{pmatrix} \nu_\tau \\ \tau^- \end{pmatrix}. \tag{1.1.2}$$

The neutrino is a massless lepton and will be discussed shortly.

The particles that can react strongly, weakly, or electromagnetically are called hadrons. These particles are composed of constituent particles we call quarks. Quarks are arranged in doublets like leptons,

$$\begin{pmatrix} u \\ d \end{pmatrix}, \begin{pmatrix} c \\ s \end{pmatrix}, \begin{pmatrix} t \\ b \end{pmatrix}. \tag{1.1.3}$$

Unlike the leptons, the sixth quark(t, for top) may have already been discovered.[1] Each hadron has either a quark and anti–quark, or a combination of three quarks. The quark model will be discussed in more detail later.

In this thesis, we investigate the strong force using the weak and electromagnetic forces. Many reactions involving the decay of a strongly interacting particle are difficult to calculate, and new techniques are being used to find a complete model. Our job will be to make the best measurements possible such that theorists can use the results in the pursuit of the correct model.

We will study a reaction that is part weak and part strong. A hadron containing a c(charm) and a u(up) quark decays part of the time to a lepton, its neutrino partner and a hadron containing both an s(strange) quark and a u(up) quark. The well understood weak potion of the decay will allow us to separate strong and weak effects.

1.2 Thesis Content

We present a measurement of the form factors and the rate of the decay $D^0 \to K^-\mu^+\nu_\mu$ relative to the decays $D^0 \to K^-\pi^+$ and $D^+ \to K^{*0}\mu^+\nu_\mu$. We will trace the history of weak decays and discuss the measurement to be made with the data.

The data for this thesis were collected during two separate running periods of the Fermi National Accelerator Laboratory(Fermilab) Experiment E687 between February 1990 and January 1992.

The experiment studies interactions of a high energy photon beam in a beryllium target. In Chapter 2 we discuss how the beam is delivered to the experiment and how the experimental apparatus works. In Chapter 3 we describe the reconstruction of the data. The final analysis of the reconstructed data is in Chapter 4, and the systematic error of the final analysis is detailed in Chapter 5. We combine the results of Chapter 4 and Chapter 5 in Chapter 6 to get a final result to compare to other experiments.

1.3 Beta Decay

In the 1920's scientists wondered why there was an apparent non–conservation of energy in nuclear beta decays. In these kinds of decays an atom emits an electron and a neutrino and the nuclear properties of the atom change. One example of a nuclear beta decay studied by these scientists, besides Carbon–14, is the decay of Boron–12:

$$^{12}_{5}B \rightarrow ^{12}_{6}C + e^{-} + \overline{\nu}_e \tag{1.3.1}$$

When measurements of beta decay were made, the early researchers could not detect the presence of the neutrino and could not explain the continuous energy spectrum of the emitted electron. In a 1930 letter[2] Wolfgang Pauli suggested that a neutral non–interacting particle could balance the energy equation. Enrico Fermi[3] used this assumption to show that energy is conserved in the decay and that the energy spectra of the electron can be explained given a few simple assumptions.

Since the rate of nuclear beta decay is small and the physical difference between the initial and final state of the nucleus is small, we can deduce that whatever is causing the decay is a small perturbation on the system (the rate of a reaction is related to the strength, or coupling, of the interaction causing the perturbation and the difference between the initial and final states of the system). Using the neutrino hypothesis and borrowing from the theory of electromagnetic interactions, Enrico Fermi was able to calculate the physical change(difference between initial and final states) in the system, but he left the strength or coupling of the interaction causing the reaction as an experimentally determined quantity.

Specifically, he modified the matrix element, or physical change, for the charged current–current electromagnetic interaction of a proton and an electron (using Dirac notation) from(see Figure 1.3.1):

$$M = (e\overline{u}_p\gamma^\sigma u_p)\left(-\frac{g^{\sigma\delta}}{q^2}\right)(-e\overline{u}_e\gamma_\delta u_e) \tag{1.3.2}$$

to:

$$M = \mathrm{G_F}(\overline{u}_n\gamma^\sigma u_p)(\overline{u}_\nu\gamma_\sigma u_e) \tag{1.3.3}$$

where $\mathrm{G_F}$(the coupling) is to be determined by experiment.

His calculation reproduces the beta decay energy spectrum of the electron quite adequately. Energy conservation was saved, and since the strength of the force was much smaller than the electromagnetic and the nuclear forces but much larger than the gravitational force, there was an argument for another fundamental force of nature to go with the electromagnetic, strong(or nuclear), and gravitational forces. We have already mentioned this force: it is called the *weak* force, therefore, nuclear beta decay is a *weak* decay.

In the period between Pauli's suggestion and the mid–1950's, it became apparent that there were myriad particles in the universe besides the proton and the electron. One of these particles, the kaon, which decays with a small rate like beta decay, was seen to have some unusual properties. It was observed that the kaon can decay into two pions and three pions as well as other possibilities. One can make an interesting comparison between the two and three pion case by studying the angular decay distribution of the three pion decay. If the kaon decays into 3 pions in an entirely random way, the kaon has no angular momentum or spin, and the parity(behavior under reflection) of the a)

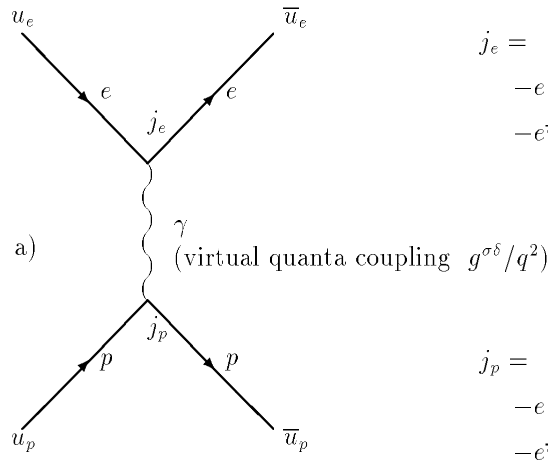

$j_e =$
$-e(p_e^{initial} + p_e^{final})_\delta$ (EM)
$-e\overline{u}_e\gamma_\delta u_e$ (Dirac)

$j_p =$
$-e(p_p^{initial} + p_p^{final})^\sigma$ (EM)
$-e\overline{u}_p\gamma^\sigma u_p$ (Dirac)

b)

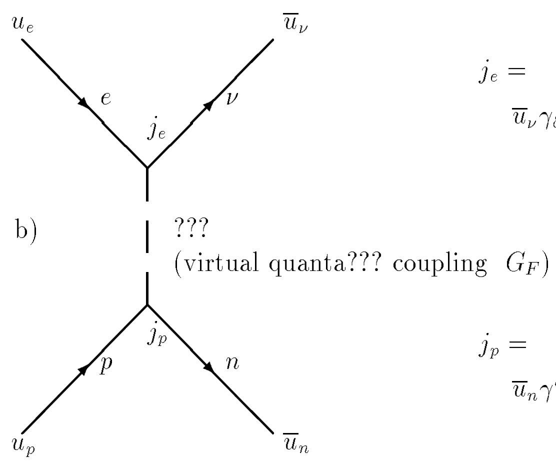

$j_e =$
$\overline{u}_\nu\gamma_\delta u_e$ (Dirac)

$j_p =$
$\overline{u}_n\gamma^\sigma u_p$ (Dirac)

Figure 1.3.1 Diagram of the modification Fermi made to the electromagnetic interaction. The electromagnetic current is in a), and the weak current is in b).

kaon is that of its decay products. It was observed that the three pion decay was random, therefore, the kaon has no spin, and since the parity of the pion is odd(-1), we expect that the kaon has odd parity too($(-1)^{3(pions)} = -1$). We know that the kaon decays into two pions as well, so we expect the kaon to have even($((-1)^{2(pions)} = 1)$ parity (see Figure 1.3.2)! The investigators[4] considered the possibility that weak decays do not respect parity. Several experiments were suggested to confirm or deny the hypothesis that parity was violated for weak decays.

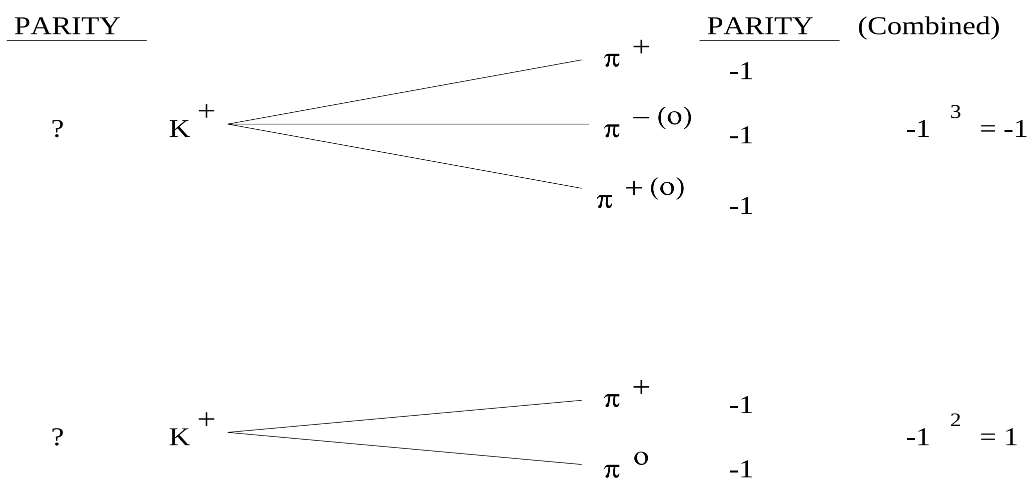

Figure 1.3.2 Diagram of K^- decay into 2 and 3 pions.

The experiment performed first was designed to determine whether parity was conserved in nuclear beta decay.[5] Cobalt–60 atoms were cooled and the spins of the atoms were aligned. The decay of the Cobalt–60 atom involves an angular momentum change of one unit. The spins of the emitted electron and neutrino lie along the direction of the Cobalt–60 atom to conserve angular momentum(see Figure 1.3.3).

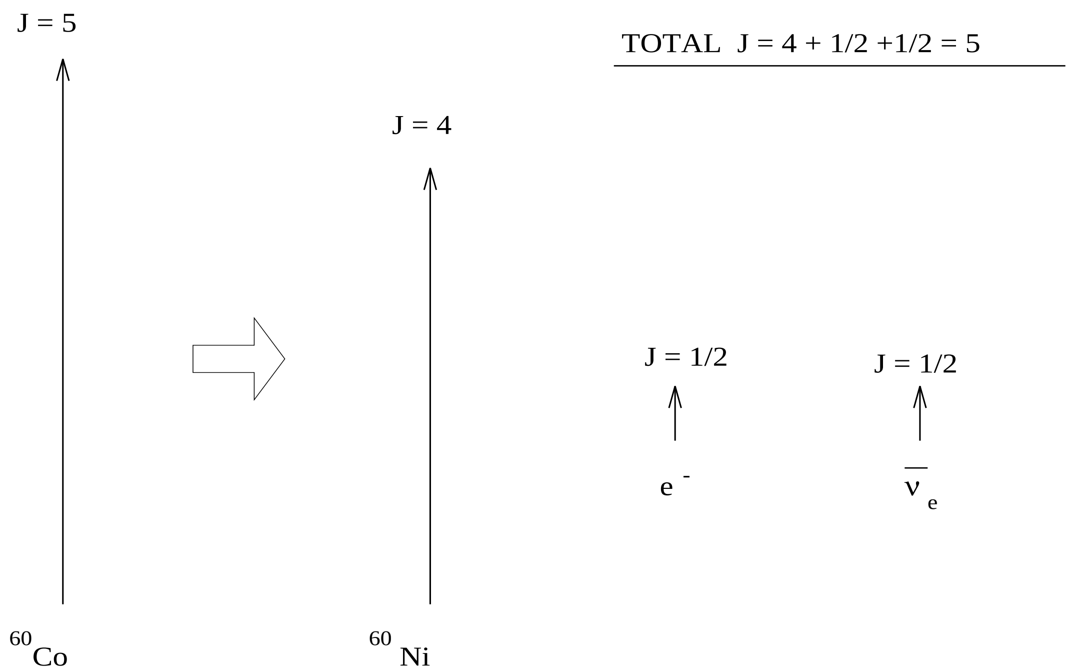

Figure 1.3.3 Diagram showing conservation of angular momentum in the beta decay of Cobalt–60.

The emitted electron can exist in two spin 1/2 states: one state in which the spin of the electron is generally along the electron momentum and one where the spin of the electron is generally opposite to the electron momentum. Both of these states can contribute to the decay. If both of these states are present in equal quantities, the sum of the two states gives the emitted electrons a symmetric distribution (see Figure 1.3.4), and the behavior under reflection(parity) is the same. If one of these states is emitted more often than the other, the sum of the two states gives the electrons emitted a non–symmetric distribution, and the behavior under reflection(parity) is different. The emitted electron distribution was measured, the spin of the Cobalt–60

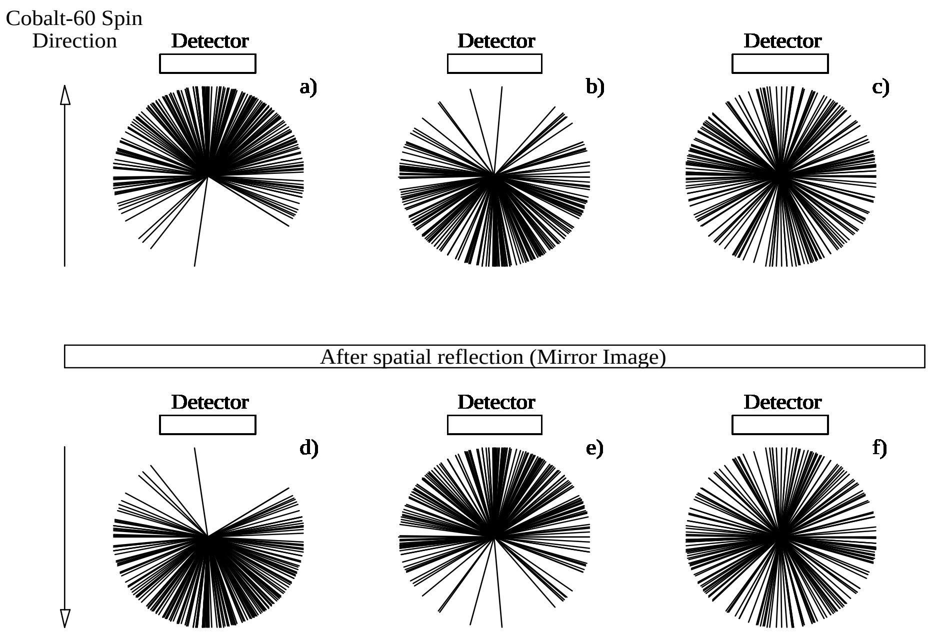

Figure 1.3.4 Diagram of detailing the parity conserving and non–conserving aspects of the emitted electron in the beta decay of Cobalt–60. In a) the electron is emitted preferentially along its spin, in b) away form its spin and in c) shows no preference(equal mixture of a) and b)). In d)–f) we have reversed the polarization of the Cobalt–60 atom to affect a spatial reflection of the decay. If a) is preferred, the detector will count less electrons (d)). If b) is preferred, the detector will count more electrons(e)). If equal mixtures of both states are present, the detector sees no difference(f)) and a spatial reflection does not alter the outcome of the experiment. The experiment of Wu[5] implied that case b) is highly favored.

atom was reversed relative to the experimental setup, and the emitted electron distribution was measured again. It was discovered that the electron was emitted preferentially opposite to the direction of the aligned spin (see Figure 1.3.4) of the Cobalt atoms. Thus, the behavior under reflection was different, and parity was not conserved for this decay.

A subsequent experiment[6] confirmed that parity was always violated for beta decay and another[7] determined that the neutrino was always created with its spin opposite(left–handed) to its direction of travel.

We have to modify Fermi's prescription to choose only left–handed neutrinos:

$$M = \mathrm{G_F}(\overline{u}_n(\gamma^\sigma)(1-\gamma^5)u_p)(\overline{u}_\nu(\gamma_\sigma)(1-\gamma^5)u_e) \qquad (1.3.4)$$

where $\gamma^\mu\gamma^5$ picks out the left–handed part of u_ν. So far we have been careful to choose transitions where the initial and final states containing nucleons are almost the same. What happens to the expression for M if we have a large change between the initial and final states or the particles are not spin 1/2 objects like the proton and the neutron?

Another particle that was known to react only weakly or electromagnetically was discovered in the mid 1930's. It is 200 times more massive than the electron, so the process of this particle, called the muon, decaying into two neutrinos and an electron represents a large physical change. We modify the expression for M:

$$M = \mathrm{G_F}(\overline{u}_\nu(\gamma^\sigma)(1-\gamma^5)u_\mu)(\overline{u}_\nu(\gamma_\sigma)(1-\gamma^5)u_e) \qquad (1.3.5)$$

and the measured value of G_F agrees with the nuclear beta decay experiments. Now we look at decays with particles that have integral spin and do not blend easily into our theory.

It was observed that a strongly interacting pion decays into a muon or an electron. Unfortunately, there is no convenient picture of a current with pion decay (Figure 1.3.5 a)). A description of the strong force might help.

From scattering experiments we infer that the strong force has a range on the order of 10^{-15}m(called a Fermi, short for femtometer) and has a large coupling which renders it unsuitable for many perturbative calculations, especially if there is a large physical change in the system. In 1935, H. Yukawa[8] suggested that the strong force is analogous to the electromagnetic force except that a virtual particle with mass is exchanged as a quanta instead of a photon. Such a virtual particle exists only within the confines of the uncertainty principle:

$$\Delta \mathrm{E}\ \Delta \mathrm{T}\ \geq \hbar \tag{1.3.6}$$

and, the mass for such a virtual particle moving the speed of light(c) is:

$$mass \sim \hbar/(c \times (1 \rightarrow 2\ fermi)) \sim 100 \rightarrow 200\ MeV/c^2 \tag{1.3.7}$$

thus a natural choice for a quanta to carry the strong force is the pion(mass$\sim$ 139.6 MeV/c^2). If we think that the pion, or any massive particle, conveys a force, we have to modify the $\frac{1}{q^2}$ term in the current. In the first Born approximation, the $\frac{1}{q^2}$ behavior of the scattering is just the Fourier transform of the perturbing potential. To get an idea of the form the $\frac{1}{q^2}$ term has for massive quanta we take the Fourier transform of the Yukawa potential(the actual replacement is a bit more complicated):

$$\begin{aligned} F(\mathbf{q}) &= \int V(r) e^{i\mathbf{q}\cdot\mathbf{r}} d^3x \\ &\propto \frac{1}{q^2}, \qquad V(r) = \frac{1}{r}\ (\mathrm{EM}) \\ &\propto \frac{1}{q^2+m^2}, \quad V(r) = \frac{e^{-r/m}}{r}\ (\mathrm{YUKAWA}) \end{aligned} \tag{1.3.8}$$

This approach gets complicated quickly as there are many particles available as quanta.

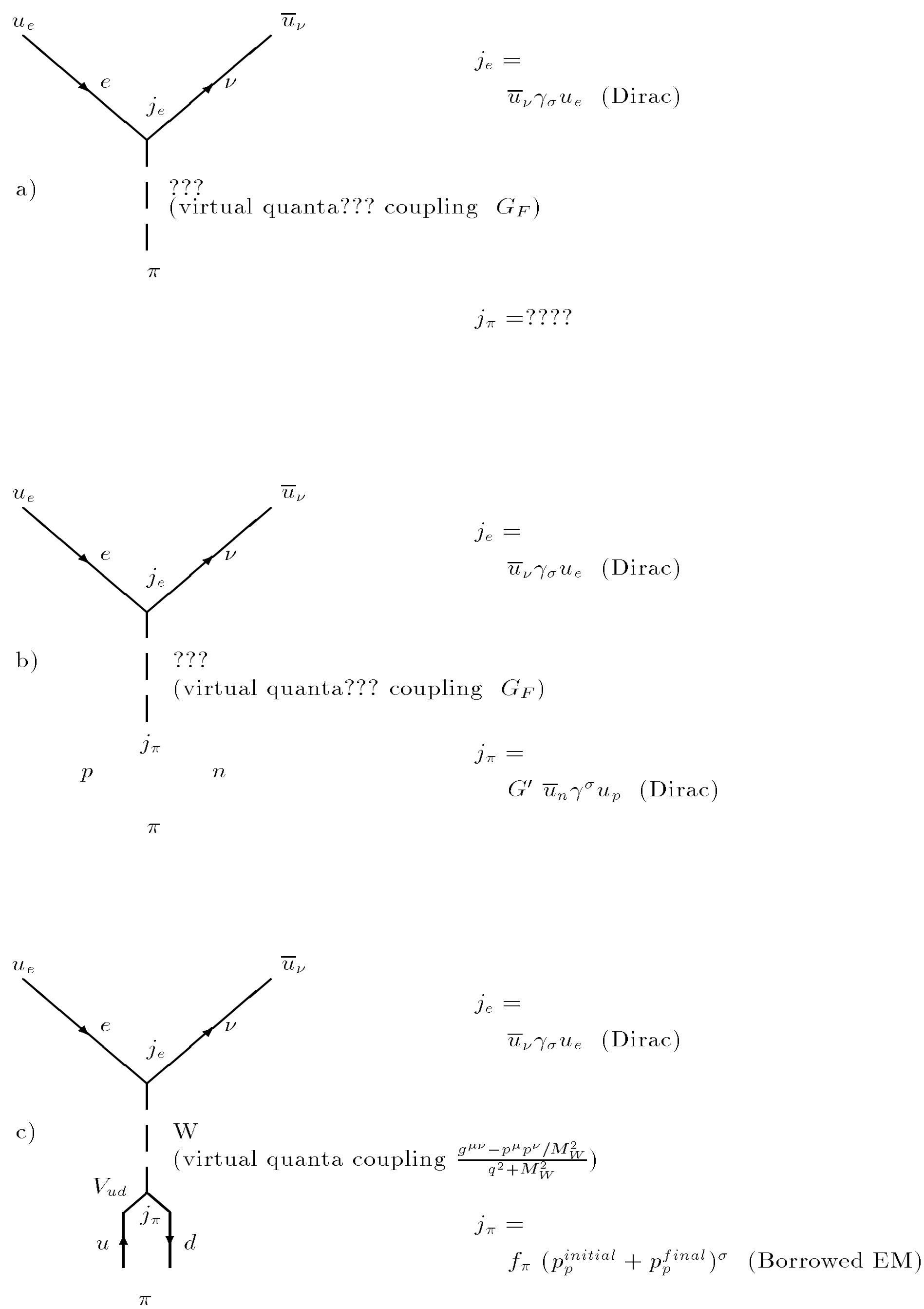

Figure 1.3.5 Diagram of pion decay. Shown are a), the Fermi method, b), a particle exchange model and c), the spectator quark model.

As an example, we know that the charged pion decays into a muon and a neutrino. The easiest approach is to assume that the muon and the neutrino couple to a neutron and a proton generated by the strong field around the pion. We need only measure the coupling of the pion to the neutron and the proton(Figure 1.3.5 b)). We know that the flavor of the muon side does not affect the coupling since the ratio of rates of the electron and muon decays of the pion(and kaon) agree with the calculation where the coupling is reduced to a constant for the pion(or kaon) "current." Part of the burden of choosing which strongly interacting particles to couple to, or how to proceed perturbatively, is eased by using a classification scheme for strongly interacting particles.

1.4 Enter the Quark

In the 1960's it was clear that electron–proton scattering experiments had some unusual data. The results of these experiments could be explained if the proton had structure. This view of the proton being made of constituent particles agreed with a classification scheme[9,10] which had already seen success in predicting the existence, as well as the mass and decay modes of the Ω^- particle.

The idea is that every strongly interacting particle is made of constituent particles called quarks. Each quark has spin 1/2 and charge +2/3 or -1/3(the electron has charge -1). Quarks with the same charge but different mass have different flavors. These flavors are conserved in strong interactions but change in weak interactions. For instance, the difference between the kaon and the pion is the flavor of the charge 1/3 quark. Each quark also has extra degrees of freedom called color. There are 3 colors and 3 anti–colors. Color is needed to explain why three spin 1/2 particles do not apparently violate the Pauli exclusion principle in the Δ^{++} particle. Color exchange via a gluon is the basis for the latest model of the strong force(called Quantum Chromodynamics). Particles, which we have been calling hadrons, that contain two quarks are called mesons, and particles with three quarks are called baryons. Quarks have never been observed to exist outside of these two classifications, and we can only roughly estimate some of their properties.[11] Table 1.4.1 is a list of the quarks and their properties.

Table 1.4.1 Quark Properties

Quark	$\sim$ Mass	Charge	Flavor
up u	0.005 (GeV/c^2)	$2/3 \mid e \mid$	isospin$(I_z) = 1/2$
down d	0.01	-1/3	isospin$(I_z) = -1/2$
strange s	0.2	-1/3	strangeness$(S = -1)$
charm c	1.3	2/3	charmness$(C = 1)$
bottom b	4.3	-1/3	bottomness$(B = -1)$
top t??	170	2/3	topness$(T = 1)$

Table 1.4.2 is a list of some particles mentioned in this thesis and their quark content.

Now we can classify our couplings using quarks instead of other hadrons and assign a strength corresponding to the particular flavor change for each decay(Figure 1.3.5 c)). By convention, the flavor changing numbers are combined as a unitary matrix that rotates the charge -1/3 quark vector for proper combination with the charge 2/3 quark vector.[12,13]

Table 1.4.2 Quark Content of some Particles

Particle	Mass	Charge	Spin	Flavor	Quark content
units	(GeV/c^2)	$\mid e \mid$	$\hbar$	1	1
proton	0.938	1/2	1/2	0	uud
neutron	0.939	0	1/2	0	udd
anti–proton	0.939	-1/2	1/2	0	$\overline{u}\overline{u}\overline{d}$
kaon(k^+)	0.494	1	0	S	$u\overline{s}$
kaon(k^-)	0.494	-1	0	-S	$\overline{u}s$
pion(π^+)	0.140	1	0	0	$u\overline{d}$
D^0 meson	1.865	0	0	C	$c\overline{u}$
J/Ψ	3.097	0	1	0	$c\overline{c}$

$$\begin{pmatrix} d' \\ s' \\ b' \end{pmatrix} = \begin{pmatrix} V_{ud} & V_{us} & V_{ub} \\ V_{cd} & V_{cs} & V_{cb} \\ V_{td} & V_{ts} & V_{tb} \end{pmatrix} \begin{pmatrix} d \\ s \\ c \end{pmatrix} \tag{1.4.1}$$

The matrix is called the Cabibbo–Kobayashi–Maskawa mixing matrix, and we can use the coupling numbers from other decays or interactions to determine couplings we haven't measured yet using the unitarity constraint.

We combine the quark model and the mixing convention to make a practical theory of the weak interactions called the spectator quark model.

1.5 Spectator model

In the spectator model, we assume that all the action in a weak decay is contained in the flavor changing part of the current. We illustrate the form of the current for the beta decay of a kaon into a pion in Figure 1.5.1. We have included a new particle, the W, to convey the weak force(the $\frac{g^{\mu\nu}}{q^2}$ factor in the electromagnetic current becomes $\frac{g^{\mu\nu}-p^{\mu}p^{\nu}/M_W^2}{q^2-M_W^2}$ when the quanta is massive). Since the weak force is small, M_W is large, and for our purposes we use the Fermi constant instead of a $\frac{Constant}{M_W^2}$ term in the current.

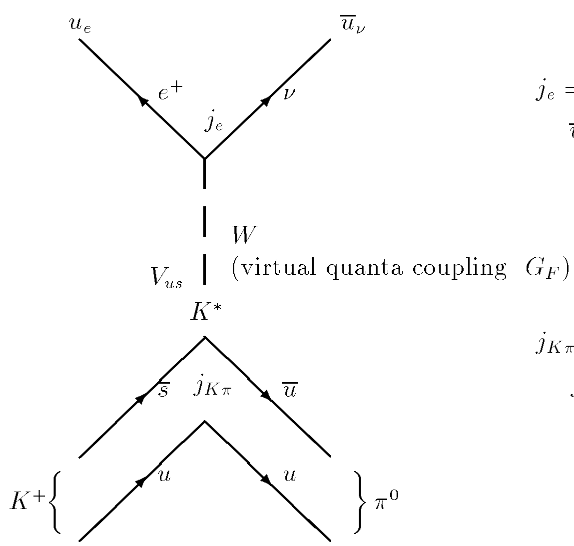

$$j_e = \overline{u}_\nu \gamma_\sigma u_e$$

$$j_{K\pi} = f_+(q^2)(p_K + p_\pi)^\sigma + f_-(q^2)(p_K - p_\pi)^\sigma$$

Figure 1.5.1 Diagram of kaon decay in the spectator quark model.

To test the viability of the spectator model we compare kaon and pion decays. Table 1.5.1 is a list of decay rates for kaons and pions calculated using the spectator model(no form factors are used) and the rate we measure in the laboratory. Also shown is the coupling used from the mixing matrix for the flavor change.

Agreement is not very good, but we weren't trying to take into account any strong force contributions. If we try to remove the strong contributions by taking ratios, we find the results in Table 1.5.2. Calculations are shown for the spectator model with and without the coupling term.

Table 1.5.1 Calculated and Measured decay rates

Decay	Spectator Model(sec^{-1})	Measured(sec^{-1})	Coupling
$K^+ \to \mu^+\nu_\mu$	2.0×10^9	5.13×10^7	$V_{us} = .22$
$K^+ \to \pi^0 e^+\nu_e$	7.3×10^6	3.9×10^6	$V_{us} = .22$
$\pi^+ \to \pi^0 e^+\nu_e$	0.22	0.4	$V_{ud} = .975$
$\pi^+ \to \mu^+\nu_\mu$	2.2×10^9	3.84×10^7	$V_{ud} = .975$

Table 1.5.2 Calculated and Measured decay rates in ratio

Ratio	Spectator Model	Measured	Spectator w/o coupling($V_x = 1$)
$\frac{K^+\to\mu^+\nu_\mu}{\pi^+\to\mu^+\nu_\mu}$	0.91	1.33	18.8
$\frac{K^+\to\pi^0 e^+\nu_e}{\pi^+\to\pi^0 e^+\nu_e}$	3.3×10^7	0.975×10^7	68.2×10^7

The calculation agrees with experimental results much better when the couplings from the mixing matrix are used in the estimate, but we still have to account for strong interactions. We use the decay $K^+ \to \pi^0 e^+\nu_e$ as an example of estimating the contribution of the strong force.

1.5.1 The Decay $K^+\to\pi^0 e^+\nu_e$

We adopt a meson exchange approach(Figure 1.5.1), and the exchanged meson has the properties of the us vertex, the strong interaction and couples to the W meson. The lowest mass strange meson resonance is the $K^*(892)$ vector meson. Including a term for the massive K^* propagator in addition to the term for the massive W propagator, our parameterization of the current becomes:[14]

$$M = \mathrm{G_F}\ f_K\ (p_K + p_\pi)^\sigma \left[\frac{g^{\sigma\delta} - p^\sigma p^\delta / M_{K^*}^2}{q^2 - M_{K^*}^2}\right] (\overline{u}_\nu \gamma_\delta (1-\gamma^5)\gamma u_e) \tag{1.5.1}$$

which can be written:

$$M = \mathrm{G_F}\ \frac{f_K}{q^2 - M_{K^*}^2}\left[(p_K + p_\pi)^\sigma - \frac{M_K^2 - M_\pi^2}{M_{K^*}^2}(p_K - p_\pi)^\sigma\right] (\overline{u}_\nu \gamma_\sigma (1-\gamma^5) u_e) \tag{1.5.2}$$

A more general approach is usually taken where one defines the hadronic current in terms of the form factors f_+ and f_-:

$$M = \mathrm{G_F}\ \left[f_+(q^2)(p_K + p_\pi)^\sigma + f_-(q^2)(p_K - p_\pi)^\sigma\right] (\overline{u}_\nu \gamma_\sigma (1-\gamma^5) u_e) \tag{1.5.3}$$

and comparing to the parameterization (1.5.2):

$$\frac{f_-(0)}{f_+(0)} = -\frac{M_K^2 - M_\pi^2}{M_{K^*}^2} = -0.3 \tag{1.5.4}$$

and since the effect of the K^* resonance is small we Taylor expand $\frac{1}{q^2 - M_{K^*}^2}$ to define:

$$f_\pm(q^2) = f_\pm(0)[1 + \lambda_\pm(q^2/M_\pi^2)] \tag{1.5.5}$$

The latest experimental data on Kaon decays are consistent with this description but favor a meson mass of about 840 MeV/c^2.[11] We will apply this approach to the study of the neutral charm meson called the D^0.

1.5.2 The Decay $D^0 \to K^- \mu^+ \nu_\mu$

Using the modification to the spectator quark model described for kaon decays, we find that the nearest vector resonance for the decay $D^0 \to K^- \mu^+ \nu_\mu$ (see Figure 1.5.2) is the D_s^{*+} at a mass of 2.11 GeV/c^2. Since this pole mass is closer to the available q^2 space for the charm meson decay, $q^2_{max} \sim 1.88\ GeV^2$, we have an opportunity, in principle, to measure the q^2 behavior as well as to test the consistency of the vector meson approach. Again, there are 2 form factors, and our expression for M becomes:

$$M = \mathrm{G_F}\ V_{cs} \left[f_+(q^2)(p_D + p_K)^\sigma + f_-(q^2)(p_D - p_K)^\sigma \right] (\overline{u}_\nu \gamma_\sigma (1-\gamma^5) u_\mu) \quad (1.5.6)$$

which leads to a decay rate in the D^0 center of mass:[15]

$$\begin{aligned}
\frac{d^2,}{dE_K\ dE_\mu} =& \frac{\mathrm{G_F}^2}{4\pi^3} |\ V_{cs}\ |^2 \\
& \Big(|\ f_+(q^2)\ |^2 \Big[M_D (2E_\mu (M_D - E_\mu - E_K) - M_D (E_K^{max} - E_k)) + \\
& \frac{1}{4} M_\mu^2 (E_K^{max} - E_k) - M_\mu^2 (M_D - E_\mu - E_K) \Big] + \\
& Re\{ f_-(q^2)/f_+(q^2) \} \Big[M_\mu^2 ((M_D - E_\mu - E_K) - \frac{1}{2}(E_K^{max} - E_k)) \Big] + \\
& |\ f_-(q^2)\ |^2 \Big[\frac{1}{4} M_\mu^2 (E_K^{max} - E_k) \Big] \Big)
\end{aligned} \quad (1.5.7)$$

where we parameterize the form factors:

$$f_\pm(q^2) = \frac{f_\pm(0)}{1 - q^2/M_{D^*}^2}, E_K^{max} = \frac{M_D^2 + M_K^2 - M_\mu^2}{2M_D} \quad (1.5.8)$$

and using the K^+ decay as an example we predict:

$$f_-(0)/f_+(0) = -\frac{M_D^2 - M_K^2}{M_{D^*}} = -0.7 \quad (1.5.9)$$

Other variations of the form factors, $f_\pm$, are possible, but their derivation and utility will not be discussed.

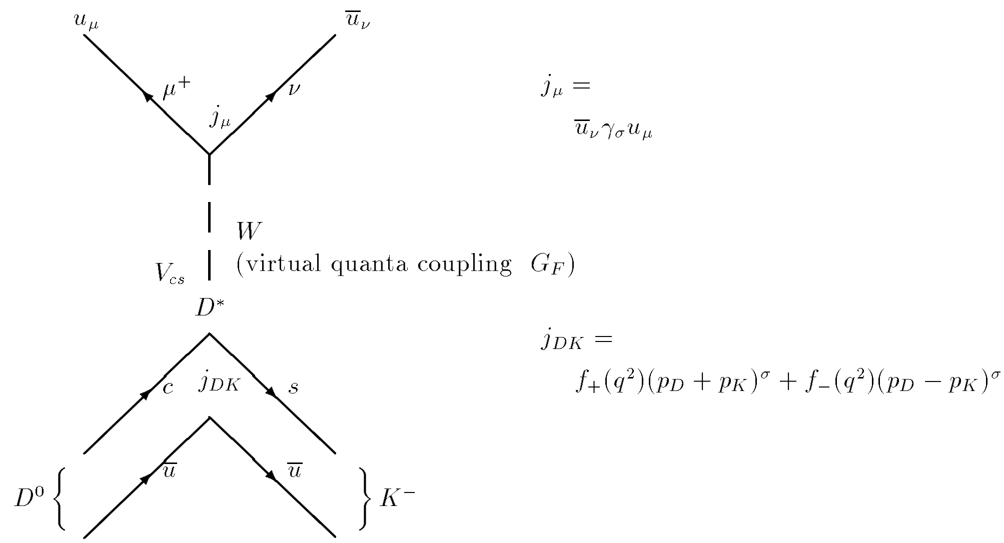

Figure 1.5.2 Diagram of D^0 decay in the spectator quark model. We also show the vector meson propagator D^*.

If we replace the muon with an electron, the terms with an $f_-(0)$ are vanishingly small, and we get an idea of the gross behavior of the decay. To examine the $f_+(q^2)$ behavior we integrate our rate over the electron spectrum to get an expression that involves only the energy of the kaon, $E_K(q^2 = M_D^2 + M_K^2 - 2M_D E_K)$. We see that the information about $f_+(q^2)$ will come from measuring the E_K, or q^2, dependence of reconstructed events.

$$\frac{d^2,}{dE_K \; dE_\mu} = \frac{\mathrm{G_F}^2}{16\pi^3} | \; V_{cs} \; |^2 | \; f_+(q^2) \; |^2 M_K \big(E_K^2 - M_K^2\big)^{\frac{3}{2}} \tag{1.5.10}$$

1.6 Scope of the Thesis

We will use the decay $D^0 \to K^- \mu^+ \nu_\mu$ to measure the strength of the $f_\pm(0)$ form factors, the pole mass associated with the vector meson model and determine the rate of the decay relative to the decay $D^0 \to K^- \pi^+$.

There will be a separate measurement to determine the decay rate of $D^0 \to K^- \mu^+ \nu_\mu$ relative to $D^0 \to K^{*-} \mu^+ \nu_\mu$ using isospin invariance and the decay $D^+ \to K^{*0} \mu^+ \nu_\mu$.

A description of the apparatus used to make the measurement, the methods used to reconstruct the data obtained by the apparatus, a study of sources and contributions to the uncertainty in the results, and a comparison of our results to other experiments will also be presented.

CHAPTER 2

APPARATUS

The equipment used to create, detect and analyze high energy physics processes is complex. This is especially true in a high rate experiment like E687.

Earlier in this century, investigators found ample physics with a few plates of photographic emulsion exposed to cosmic rays. Today, experiments continue to refine, test and add to the physics that resulted from these early ventures. To accomplish the task, modern experiments acquire a lot of data. Large quantities of data allow the investigator to refine previous measurements and to make discoveries of processes too rare to have been seen previously.

In this chapter we will discuss the mechanics involved in producing charm particles, the detection of the remnants of charm decay and the storing of the information we need to study charm decays.

2.1 Coordinate System

In the explanation of the detector and the subsequent chapter on event reconstruction, we refer to coordinate systems that are defined using physical locations within the apparatus. Figure 2.1.1 diagrams the coordinate systems and terminology used to describe locations within the experiment.

Figure 2.1.2 is the diagram of the E687 spectrometer during the 1990 running period. This spectrometer is largely described in reference [16], but we will discuss some of the detectors used in the $D^0 \rightarrow K^-\mu^+\nu_\mu$ analysis.

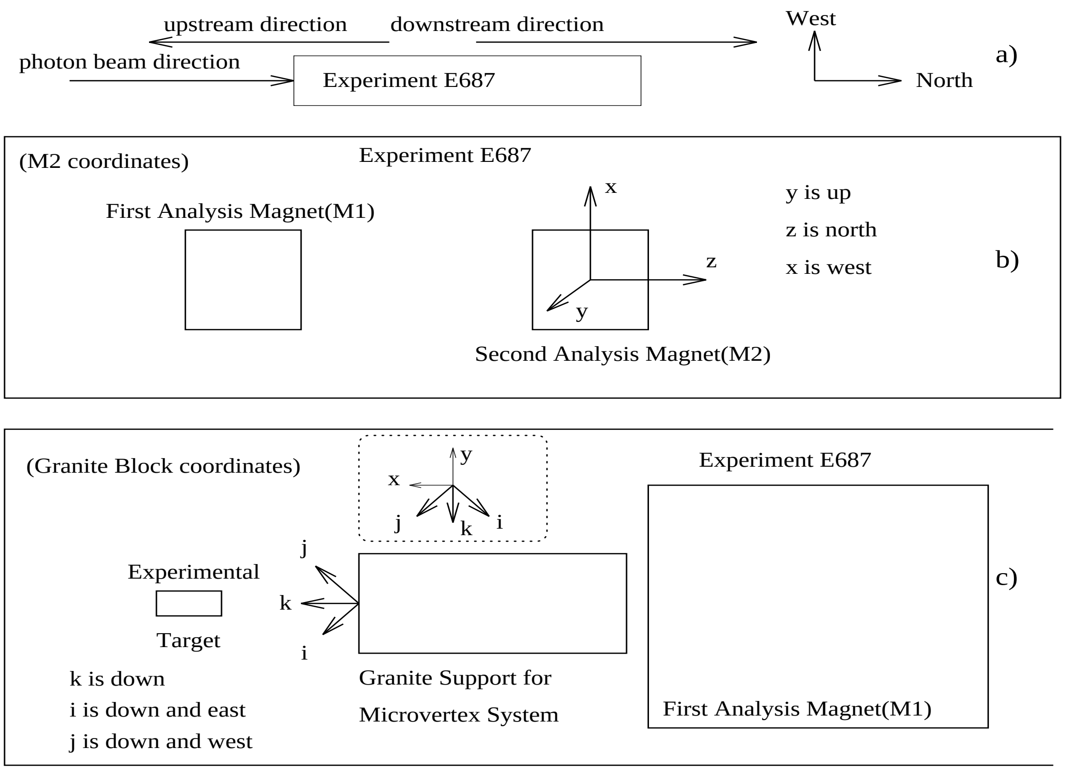

Figure 2.1.1 Idealized view of Experiment E687. We are looking down from above in all cases except the inset view of c). In a) we diagram some basic terminology. In b) we show the M2 coordinate system which has its origin in the bend center of the second analysis magnet. In c) we show the granite block coordinate system which has its origin at the upstream end of the granite block supporting the microvertex system. The inset diagram in c) shows the relationship between the M2 x and y coordinates and the granite block j, k and i coordinates. The view in the inset diagram is looking north or in the z direction.

2.2 Beamline

Protons are delivered from the Fermilab Tevatron and converted into photons. This process is described in the subsequent sections.

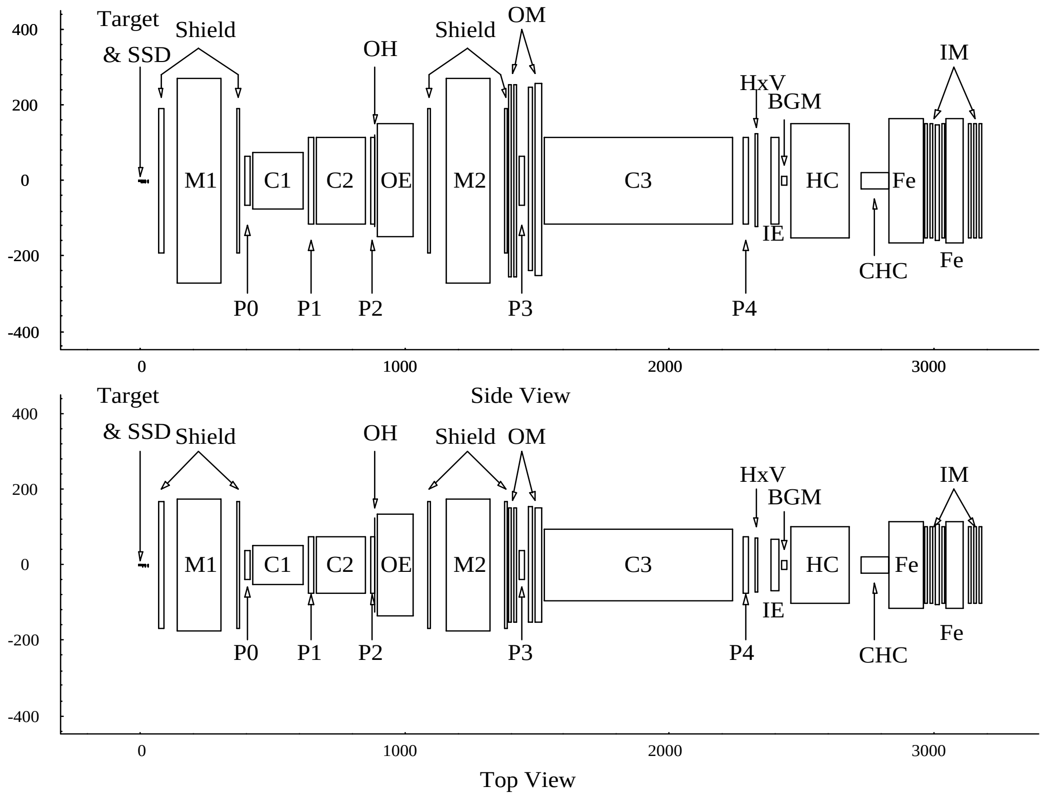

Figure 2.1.2 The 1990 configuration of the E687 spectrometer. SSD is the microvertex detector, M1 is the first analysis magnet, M2 is the second analysis magnet(operated with field opposite to M1), P0, P1, P2, P3 and P4 are Multiwire Proportional Chambers, C1, C2 and C3 are Čerenkov counters, OE and IE are electromagnetic calorimeters, OM and IM are muon identification counters, CHC and HC are hadron calorimeters, and OH and HxV are arrays of trigger counters.

2.2.1 Proton Beam

Ionized hydrogen is accelerated to 750 KeV using a Cockcroft–Walton voltage multiplier as a pre–accelerator. These hydrogen ions are accelerated to 200 MeV using a linear accelerator. The electrons are stripped from the protons using a carbon foil, and the protons are accelerated to 8 GeV in a synchrotron of diameter 500 feet. The protons are fed into a larger synchrotron(radius 1 kilometer) and attain an energy of 150 GeV. These protons are injected into the superconducting synchrotron, called the Tevatron, which sits directly below the conventional ring used to accelerate the protons to 150 GeV. In the Tevatron the protons reach the ultimate energy of 800 GeV.

To get the beam from the Tevatron, protons are given a slightly eccentric orbit, extracted from the Tevatron and fed into a beamline for fixed target experiments. Figure 2.2.1 is an idealized view of the proton accelerator and proton extraction.

2.2.2 Photon Beam

To create photons the proton beam interacts in a liquid deuterium target. The target material is chosen to maximize the number of hadronic interactions. Since at this stage of charm particle creation we are not concerned with multiple Coulomb scattering effects, we base our choice of target material on the number of nucleons relative to the number of electrons:

$$\frac{\sigma(Hadronic)}{\sigma(electromagnetic)} \propto \frac{(\ Number\ of\ Protons\ and\ Neutrons\ (A)\ )}{(\ Number\ of\ Electrons(Z)\ )^2} \quad (2.2.1)$$

and the accessibility of the target material.

Figure 2.2.2 is a diagram showing the process of creating the photon beam from the proton beam. We refer to the figure in the following description.

After some of the protons interact there is a beam containing primarily protons, but also photons(from $\pi^0 \to \gamma\gamma$), charged and neutral kaons, neutrons, pions and other particles(probably ν_τ's too!). We can use a magnet to direct the charged particles away from the neutral particles(Figure 2.2.2 Step 1.).

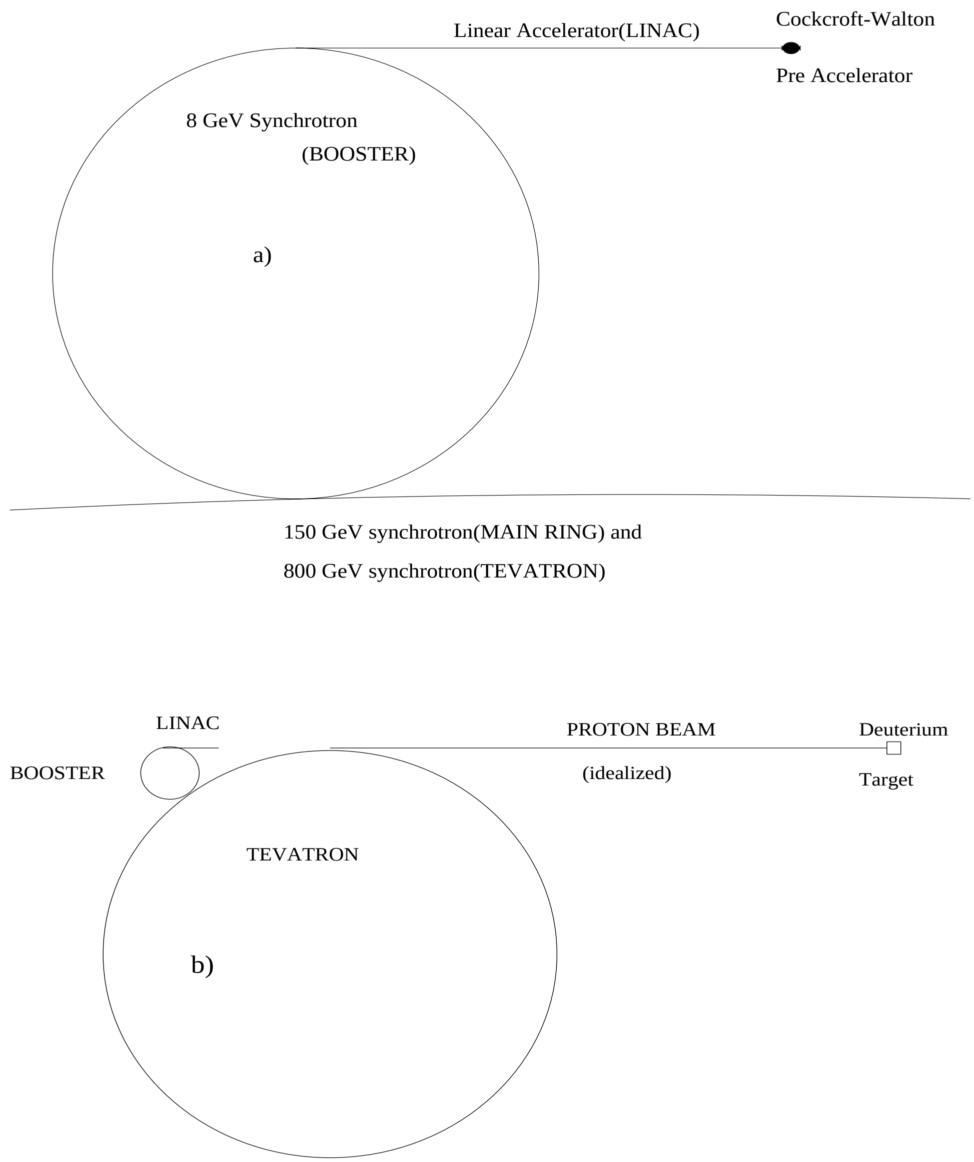

Figure 2.2.1 Idealized view of the proton accelerator in a) and the proton extraction in b).

The neutral beam is directed into a lead foil to convert the photons into electrons and positrons. Since photon interaction in matter is dominantly electromagnetic and hadron interaction in matter is mainly hadronic,

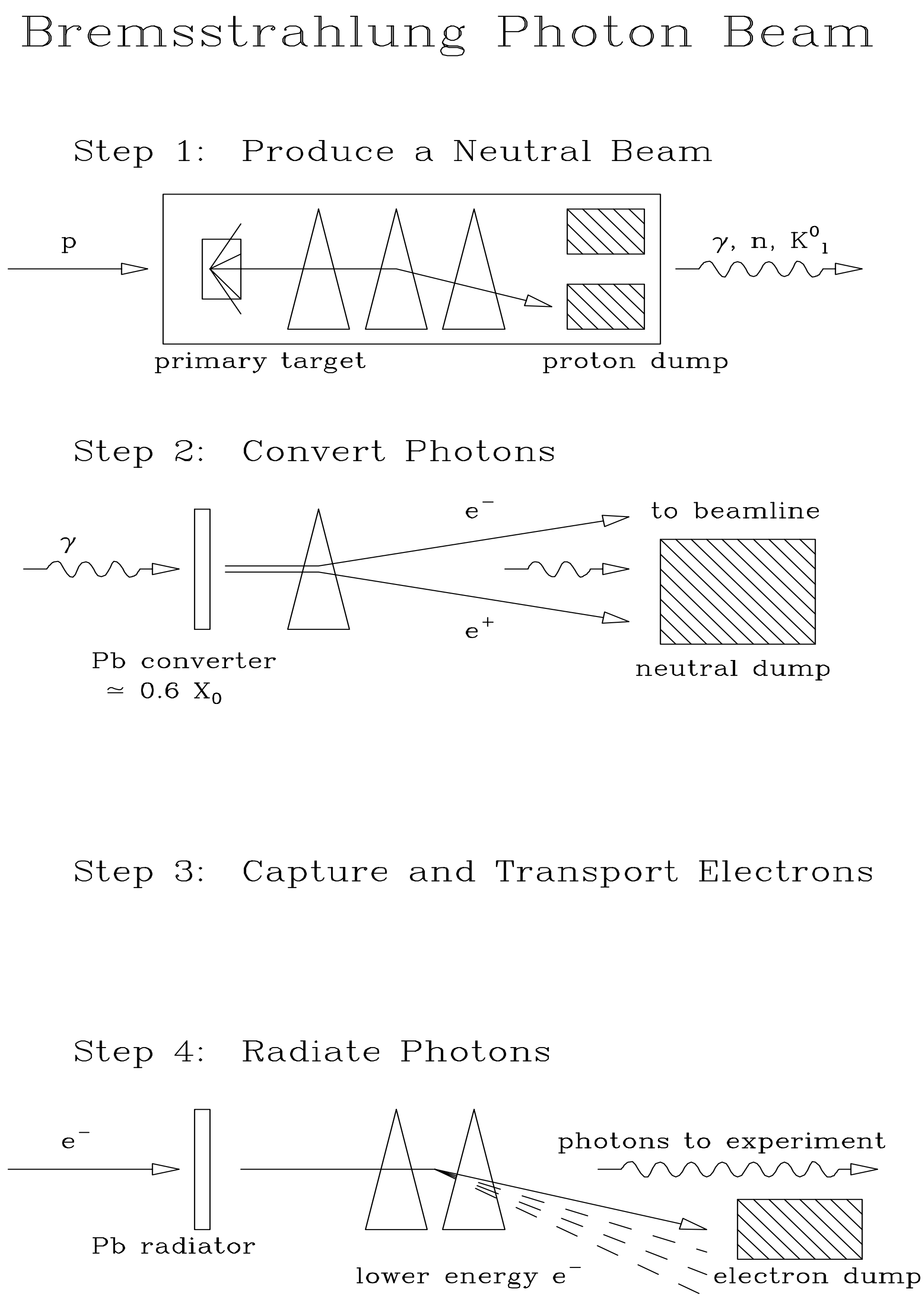

Figure 2.2.2 Diagram showing the process of creating photons from protons

we exploit the inverse of (2.2.1) by choosing lead(large Z^2/A). The charged beam(primarily electrons and positrons) produced by interactions in the foil is swept out of the neutral beam and saved, but the neutral beam is now absorbed using a block of steel(Figure 2.2.2 Step 2.).

Since the magnets used to direct the charged beam have apertures and specific field strengths, we select a specific momentum range for the charged beam in the process of bending it around the steel block. At this point, we choose to direct the positively charged beam into a steel block since the proton contamination is high. We are left with a beam of electrons with which we produce photons again.

When we create photons from the electron beam, we use a lead(large Z^2/A) converter. Before the electron beam radiates, we measure the momentum of the incoming electron(s). After the electron(s) radiate, we measure the electron(s) again to see how much energy it lost in producing the photon via bremsstrahlung radiation(Figure 2.2.2 Step 4.). The system used to measure the beam energy is described in reference [17].

Some of these photons, with some small neutral hadron contamination, interact in the experimental target and produce charm particles. The physical characteristics of the beam and the beam production are listed in Table 2.2.1.

2.2.3 Charm Production

The main reason to study charm particles in a fixed target environment is statistics. In e^+e^- colliding ring machines, the signal to noise is relatively high, but the production rate is small. To produce high statistics charm in a fixed target experiment, several types of beams have been employed. We choose a photon beam rather than a hadron beam mainly to suppress background.

Table 2.2.1 Beam Properties

Property	Value
Primary Target	Liquid D_2
Primary Target Length	3.5 m
Primary Target Proton Interaction Length	1.0
Photon Converter	Pb
Photon Converter Radiation Length	$\sim$50%
Electron Radiator	Pb, Si and other
Electron Radiator Radiation Length	20% Pb, 1.6% Si, $\sim$3% other
Horizontal spot size at production target	$\delta x = \pm 1$ mm
Vertical spot size at production target	$\delta y = \pm 1$ mm
Geometric horizontal angle accepted	$\delta\theta_x = \pm 1.0$ mrad
Geometric vertical angle accepted	$\delta\theta_y = \pm 0.75$ mrad
Geometric solid angle accepted	$\Delta\Omega = 6.0$ μsterad
Momentum bite accepted	$\Delta p/p \approx \pm 15\%$
Effective acceptance	$\Delta\Omega \times \Delta p/p \approx 96$ μster$\cdot$%
Horizontal spot at experimental target	$\delta x = \pm 1.25$ cm
Vertical spot at experimental target	$\delta y = \pm 0.75$ cm
Horizontal divergence at experimental target	$\delta\theta_x = \pm 0.6$ mrad
Vertical divergence at experimental target	$\delta\theta_y = \pm 0.5$ mrad

Most of the particles created in photon interactions are easy to filter. The main background in photoproduction is from e^+e^- production. These particles are produced at low invariant mass and pass through the experiment in a predictable fashion. Thus, we can filter out these events before we analyze the data. This is accomplished by discarding those events which deposit no hadronic energy in the hadron calorimeter(see the sections “Hadron Calorimeter” and “Triggers”). The main source of background in hadroproduction is from hadronic interactions which tend to be high multiplicity events and are most effectively filtered during analysis. A photon beam produces non–charm hadronic background as well, but at a smaller rate than hadroproduction.

Since the number of particles created during the charm fragmentation for photon gluon fusion is smaller(Figure 2.2.3) than the number of particles created during charm fragmentation from hadroproduction, the event reconstruction will produce cleaner signals for charm created with a photon beam.

One disadvantage of using a photon beam is that a long target is required to produce copious charm. A long target induces multiple Coulomb scattering for particles created in it, and, most importantly, generates backgrounds from the secondary hadronic interaction of particles created either during the fragmentation process or during the decay of a charm particle.

Another disadvantage of using a photon beam is that the beam size at the target is large. This is because we selected a spread of electron momenta to a get more photons. The large beam size forces the target positioning and beam tuning to be done carefully, and forces us to increase the acceptance of the detector at the cost of resolution.

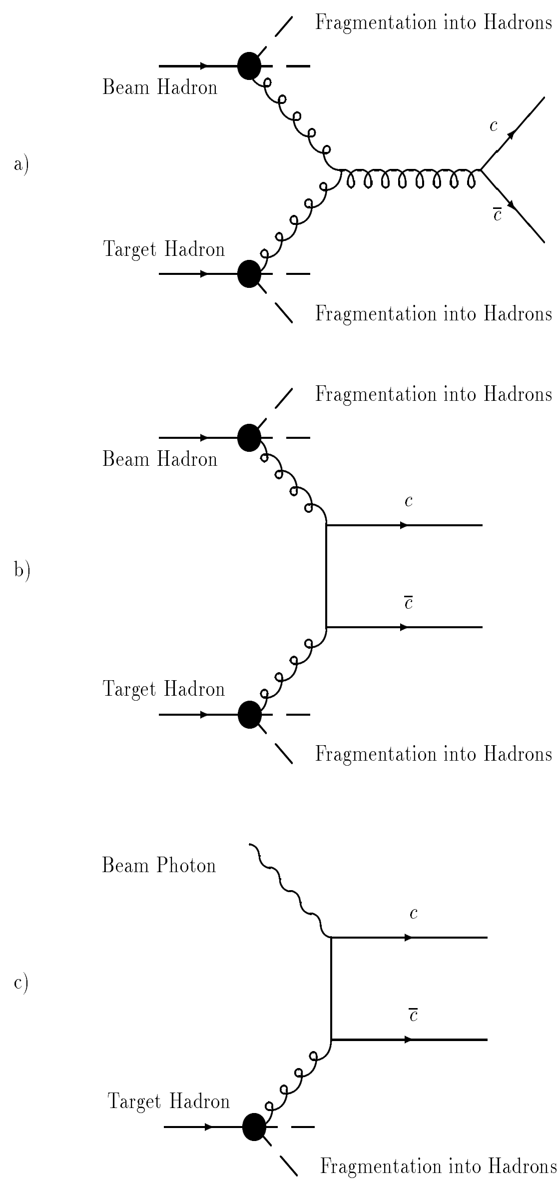

Figure 2.2.3 Leading order diagrams for charm production in hadroproduction a), b) and photoproduction c). Note that hadroproduction has two sources of fragmentation compared to photoproduction.(The crossing diagrams have been excluded for brevity.)

2.2.4 Target

Ideally, we want to maximize the number of hadronic interactions with the choice of target material, but we have to be careful to choose a material that minimizes multiple Coulomb scattering effects and does not hamper the resolution of the experiment by its physical dimensions.

Our choice of material for the charm production target is beryllium. It is denser than liquid deuterium, and the loss in hadronic yield is compensated by the reduction in multiple Coulomb scattering, by the reduction in the number of secondary hadronic interactions(since more of the charm decays occur outside the target for beryllium) and by the resolution gained by keeping the target smaller. Beryllium is also a more manageable material.

The actual physical dimensions and position of the target changed during the course of the run. For the first 3/4 of the 1990 run the target was a 3.6 cm long(z) by 2.54 cm by 2.54 cm block of beryllium rotated 45° in the x, y plane. For the rest of data taking the target length was increased to 4.4 cm.

2.3 Charged Tracking

There are two detector systems used to mark the location of the passage of a charged track. The microvertex detector is used to reconstruct the decay of a charm particle and the location where the charm particle was produced by using highly segmented strips of metal deposited on thin silicon wafers. This system is the essential detector of the experiment, and no precision charm measurements are possible without it. Strips on either side of the silicon are biased with voltage, and the ionization caused by the passage of the charged particle is attracted to the strips were it can be amplified and recorded. The Multiwire Proportional Counters work by a similar principle. Planes of wires are biased with voltage. The gas that the planes reside in is ionized by the passage of a charged particle, and the ionization travels to the wire planes where it can be amplified and discriminated. We describe some physical properties of each system in the subsequent sections.

2.3.1 Microvertex

The 12 silicon planes of the microvertex detector are arranged in 4 stations of three planes each. Each station has planes that measure the i, j, or k dimension(see Figure 2.1.1). The channel segmentation is twice as dense in the center of a plane to resolve low angle tracks. The amount of ionization, if any, deposited in each of the 8,256 channels is read out for each event for later analysis. Figure 2.3.1 is a diagram of the system.

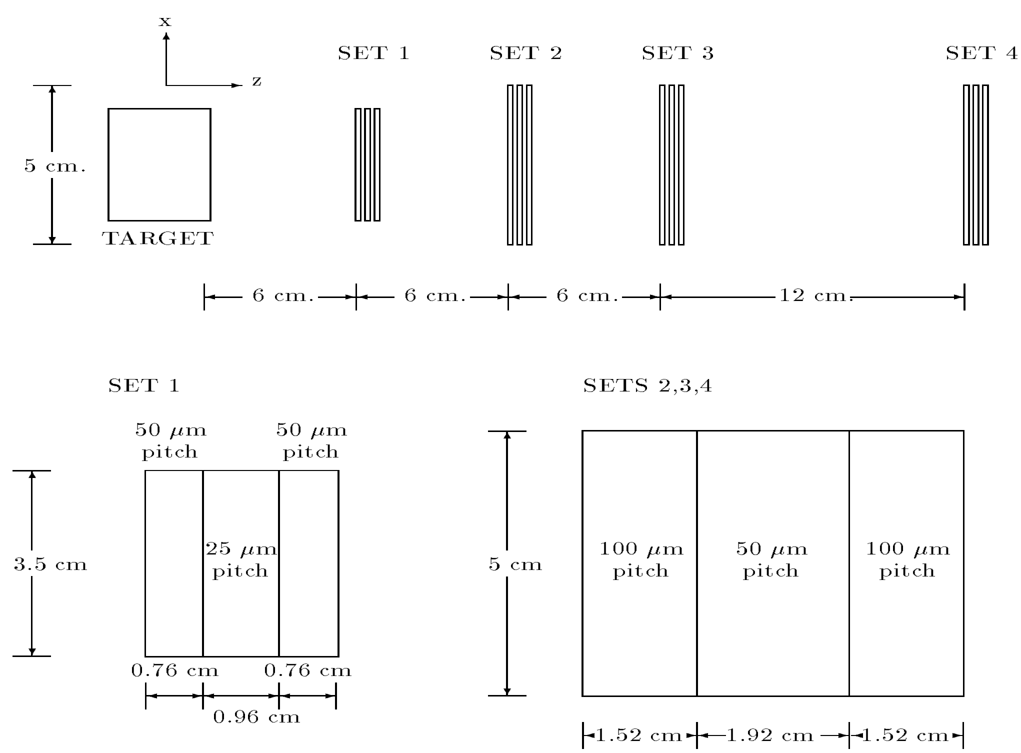

Figure 2.3.1 Microvertex layout showing positions in z and strip widths.

2.3.2 Multiwire Proportional Chambers (PWC's)

The 20 planes of the Multiwire Proportional Chambers are arranged in 5 stations of 4 planes each. Each station, or chamber, has planes that measure the x, y, u or v dimension (see Figures 2.3.2 and 2.1.1). Three chambers, P0, P1 and P2, are located between the analysis magnets, and two chambers, P3 and P4, are located downstream of the second analysis magnet(M2). The chambers not located directly downstream of a magnet, and thus not limited in acceptance by a magnet aperture, P1, P2 and P4, are larger to increase acceptance. The physical properties of each chamber are summarized in Table 2.3.1.

Table 2.3.1 PWC Physical Properties

Property	P0	P1	P2	P3	P4
Aperture (in^2)	30×50	60×90	60×90	30×50	60×90
Wire Spacing (mm)	2.0	3.0	3.0	2.0	3.3
No. X–view Wires	376	512	512	376	512
No. Y–view Wires	640	768	768	640	768
No. U/V–view Wires	640	832	832	640	832
Gas used	Argon–Ethane(65/35) Bubbled through 0° C ethyl alcohol				
Voltage Plateau	2–4 kilovolts				

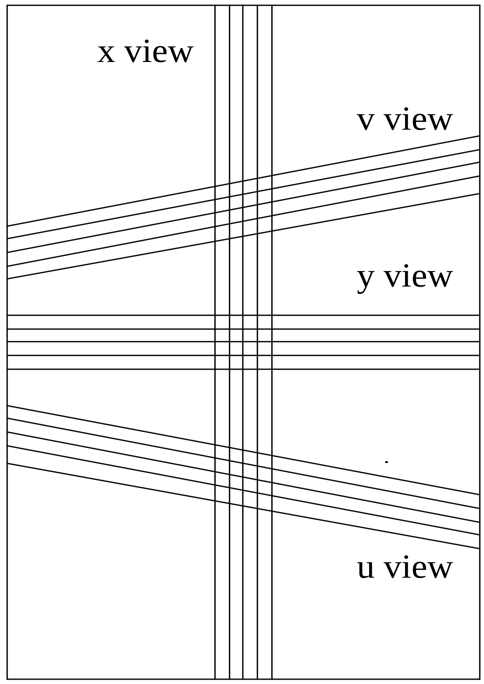

Figure 2.3.2 The four views in a proportional wire chamber. The u and v planes are rotated 11.3° with respect to the horizontal. The point of view is looking downstream.

2.4 Calorimetry

The electromagnetic calorimeters OE and IE were not used in this analysis. The hadronic calorimeters HC and CHC are used in this analysis as trigger counters only and will be described in that mode. The other calorimeters in the experiment, the BGM, 1991 CHC, and the beam calorimeter, will be mentioned only briefly.

2.4.1 Hadron Calorimeter(HC)

The hadron calorimeter consists of 28 planes of iron and 28 planes of detector. Each detector plane is a layer of proportional grooves read out capacitively in a concentric pad geometry. The signals from all the pads are summed and sent into a flash analog to digital converter(FADC). The integrated signal is used to determine the amount of hadronic energy present in a given event.

2.4.2 Central Hadron Calorimeter(CHC)

In the 1990 configuration of the experiment, the CHC was located behind the HC and measured hadronic energy that passed through the 17 cm radius hole in the HC. The energy measured was added to the HC pad sum.

2.4.3 New Central Hadron Calorimeter(NCHC)

The experiment was modified in the 1991 run to allow the passage of a beam through the experiment. The new central hadron calorimeter was constructed to allow beam to pass through yet still measure off axis hadronic energy. It also provided shielding for the inner muon system. The energy measured by this device was not added to the HC pad sum.

2.4.4 Beam Calorimeter(BC)

This calorimeter measures the part of the beam that passed through the new central hadron calorimeter. It is not used in this analysis.

2.4.5 Outer Electromagnetic Calorimeter(OE)

This calorimeter measures the wide angle electromagnetic particles that pass outside the acceptance of the second analysis magnet. It is 18.4 radiation lengths deep, and it is located in front of the second analysis magnet.

2.4.6 Inner Electromagnetic Calorimeter(IE)

This calorimeter measures the electromagnetic particles that pass through the second analysis magnet. It is located in front of the HC and consists of 100 alternating layers of lead and and plastic fiber scintillator. The 30 cm long detector is 25 radiation lengths deep. A more complete description of this detector is located in reference [18].

2.4.7 Beam Gamma Monitor Calorimeter(BGM)

This calorimeter measures the electromagnetic energy that passes through the hole in the inner electromagnetic calorimeter. It is 25 radiation lengths deep and is located behind the IE. It is specially designed to operate at high rates. It was removed for the 1991 running.

2.5 Charged Particle Identification

By determining the identity of a particle, we assign it a mass. By combining other identified particles, we reconstruct the kinematic history of a decay.

The calorimetry can be used to identify electrons, charged hadrons, muons and neutral particles. Since the information from our reconstruction was incomplete in the reduced data set used for this analysis, we exclude these detectors from our discussion.

The detectors we use to identify particles in this analysis are the Čerenkov counters and the inner muon system.

2.5.1 Čerenkov Counters

When a charged particle exceeds the speed of light in a medium, photons are emitted along the path of a particle and form a wave front of photons like the pressure front created when a plane exceeds the speed of sound.

The conical front of emitted light is focused, using mirrors, onto phototubes, and the signals from the phototubes are stored for later use.

Light is emitted if(units $c = 1$):

$$\beta = \frac{P}{E} \geq \frac{1}{n_{material}} \tag{2.5.1}$$

and for a given particle mass:

$$P_{threshold} = \frac{(M/n)}{\sqrt{1 - 1/n^2}} \tag{2.5.2}$$

which lets us identify particles based on their momentum and the index of refraction in the Čerenkov counter by checking for signals in the phototubes. With a number of different Čerenkov counters, a broad range of momentum coverage is possible. We also know the angle of the emitted radiation:

$$cos(\theta) = \frac{1}{n\beta} \tag{2.5.3}$$

So we check the pattern of emitted photons as well.

The physical characteristics of the three Čerenkov counters, C1, C2 and C3, are summarized in Table 2.5.1.

Table 2.5.1 Čerenkov Counter Properties

Counter	Cells	Gas	Length (cm)	Thresholds (GeV/c) pion	kaon	proton
C1	90	50% He, 50% N_2	187.90	6.6	23.3	44.3
C2	110	N_2O	187.96	4.5	16.2	30.9
C3	100	He	711.20	17.0	61.0	116.2

2.5.2 Outer Muon System(OM)

The outer muon system consists of two planes of proportional tubes and two planes of scintillation counters. The system uses the second analysis magnet as a hadron filter. The performance of this system is still being investigated. It is not used in this analysis.

2.5.3 Inner Muon System

The inner muon system is located at the end of the spectrometer. The system uses the shielding provided by the electromagnetic and hadron calorimetry to filter out electrons and hadrons. Additional shielding is placed around the CHC and we add steel downstream of the CHC to reduce shower fragments from pions or kaons that are late to interact in the calorimetry. The system is separated into two stations. The first station consists of a scintillator array that measures the vertical view(IM1H), a scintillator array that measures the horizontal view(IM1V), a proportional tube array that measures the horizontal view(IM1X) and a proportional tube array that measures the vertical view(IM1Y). The second station is located behind additional shielding and is identical to the first station except that no horizontal view scintillator array is used. Table 2.5.2 lists the physical characteristics of the shielding used in the simulation of the system, and Table 2.5.3 lists the physical properties of the counters used in the planes.

In 1990, a readout error limited the utility of this system. Roughly 45% of the 1990 data was affected, and we do not use this data.

In 1991 the muon system was altered to allow the passage of the photon beam through the detector. A cell(Figure 2.5.1) of 8 counters was removed from each proportional tube array, and the arrays were shifted so that the resultant gap would be centered on the beam. The frame supporting the H scintillator counters had to be modified and holes were cut in the scintillator planes. Figure 2.5.2 diagrams the changes to the system. The changes made to the system reduced its acceptance by approximately 40%. In Figure 2.5.3 we show the layout of the inner muon planes and shields.

Table 2.5.2 Materials in the Downstream Spectrometer

Material	Muon Energy Loss(GeV)	Radiation Length
IE	0.510	25.0
BGM	0.510	25.0
HC	1.459	72.08
CHC(1990)	1.347	194.8
SHIELDING BLOCKS	0.582	12.8
SHIELD 1	1.480	72.72
SHIELD 2	0.740	36.36
IE PAIR SHIELD(1991)	0.135	18.14
NCHC(1991)	1.53	75.04

Table 2.5.3 Physical Characteristics of the Inner Muon System

Plane	Channels(1990/1991)	Counter size(cm^2)	Gas
IM1V	21/21	30x100	none
IM1H	20/20	30x100	none
IM1X	64/56	5x256	(80/20)$ArCO_2$
IM1Y	96/88	5x276	(80/20)$ArCO_2$
IM2H	20/20	30x100	none
IM2X	64/56	5x256	(80/20)$ArCO_2$
IM2Y	96/88	5x276	(80/20)$ArCO_2$

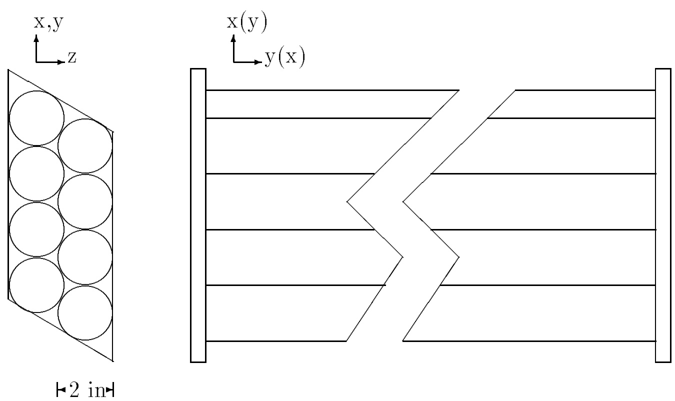

Figure 2.5.1 A propotional tube cell of 8 proportional tubes.

2.6 Trigger

As stated previously, the microvertex system is the crucial detector in the spectrometer. As we will see in future chapters, the ability to reconstruct the location where a charm particle decays and the location where it was created will give us the best signature for discriminating events containing charm from background events.

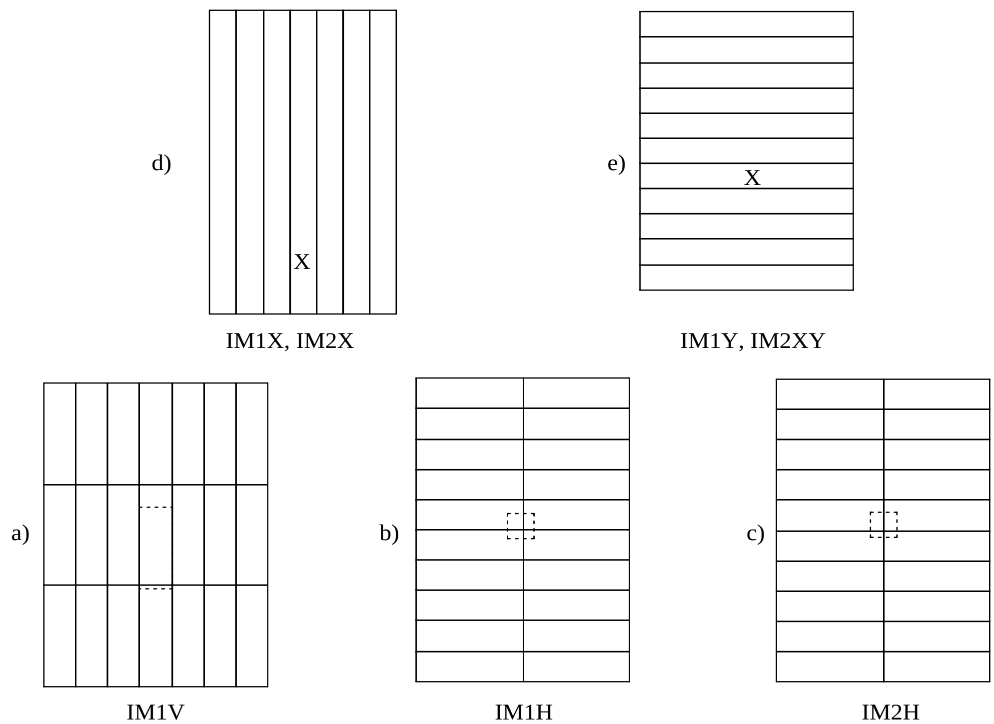

Figure 2.5.2 Diagram of inner muon scintillators(V and H) and proportional tube cells(X and Y). The dashed boxes in a, b, and c are the locations of the holes made in the scintillators for the 1991 system. The X's in d) and e) indicate which muon cells(see Figure 2.5.1) were removed for the 1991 system.

We want to record all events where a photon interacts in the target hadronically. We discard the event if a charged particle, from contamination in the photon beam, interacts in the target or the photon interacts electromagnetically. The event must have at least one charged particle that passes through the microvertex, and hadronic energy must be present in the event. All of these considerations go into choosing a filter, or trigger, to select the good events.

While we are recording an event on tape, or making a decision about an event in hand, we cannot test other events. We freeze the information we have

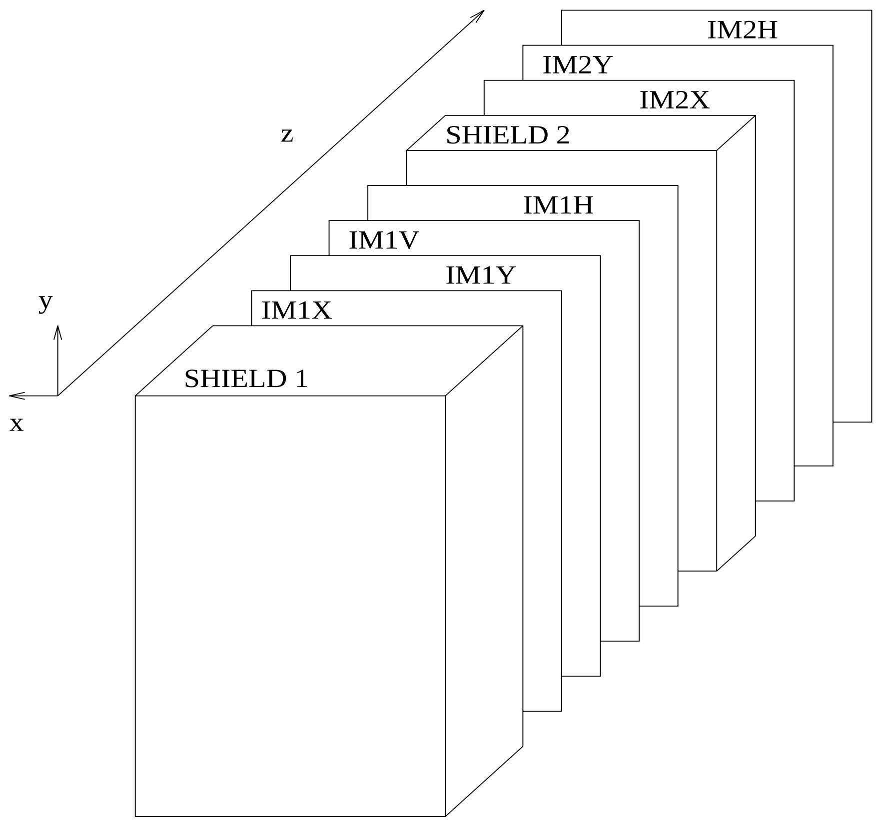

Figure 2.5.3 Expanded view of 1990 inner muon system configuration.

until we decide to keep the event or to look for another. Some decisions can be made quickly, while others take time.

To ensure that a photon interacted in the target and a charged particle passed through the microvertex four scintillation counters are used in coincidence(see Figure 2.6.1). Two scintillation counters(A0, A1) are placed in the photon beam upstream of the target to veto incident charged particle contamination. A scintillation counter(TR1) is placed between the target and the microvertex to detect the charged particles that come from interactions in the target. Another scintillation counter(TR2), placed directly downstream of the microvertex, is used to make sure the charged particles pass through the microvertex.

Figure 2.6.2 is a diagram of the scheme used to discard events from $\gamma \rightarrow e^+e^-$ conversions. Electrons and positrons produced in the target travel parallel to the z direction until they are bent in the y dimension by the first analysis magnet and refocused to a location in front of the IE by the second analysis magnet. Some of these particles lose energy in the magnets, lose energy in material downstream of the initial interaction or don't pass through the second magnet, hence, there is a swath of particles that extends in the y dimension. In hadronic events we expect particles to be created at wider angles than $\gamma \rightarrow e^+e^-$ conversions. We place counters downstream of the analysis magnets which allow the swath of e^+e^- to pass through undetected while detecting particles outside of the swath. Downstream of M1, there is an array of trigger counters(OH) that has a gap(see Figure 2.6.3) to allow the $\gamma \rightarrow e^+e^-$ to pass through. Downstream of M2, there are two arrays of trigger counters(H and V) with a gap that are used in coincidence to detect particles that strike the array. In 1991 we added a plane of scintillators(VPRIME) behind the IE and a lead bar in front of the IE that covers the region expected for e^+e^- events. The VPRIME counters work with the H counters(in place of V), the IE and the lead bar to filter out the e^+e^- events.

Sometimes, there is charged contamination that comes from muon production in the steel block we use to filter out neutral particles created by the protons interacting in the deuterium target. This contamination enters the experiment outside the acceptance of the A0 and A1 counters. We place two large scintillation counters(TM1 and TM2) directly downstream of the A1 counter to veto this off–axis muon contamination. In practice though, we find the inclusion of these counters in the trigger unnecessary, and for most of the running they were not included in the trigger.

These scintillation counters are the trigger elements that are used to make fast decisions. The combination of the signals from these counters goes into a fast trigger we call the Master Gate or first level trigger. Figure 2.6.1 shows the trigger counter locations in the microvertex region of the spectrometer. Figure 2.6.3 shows the physical layout of the counters used to make the H, V, VPRIME and OH arrays, and Figure 2.6.2 shows the principle that motivates the gap in the trigger counters and the relationship between the lead bar, IE and VPRIME.

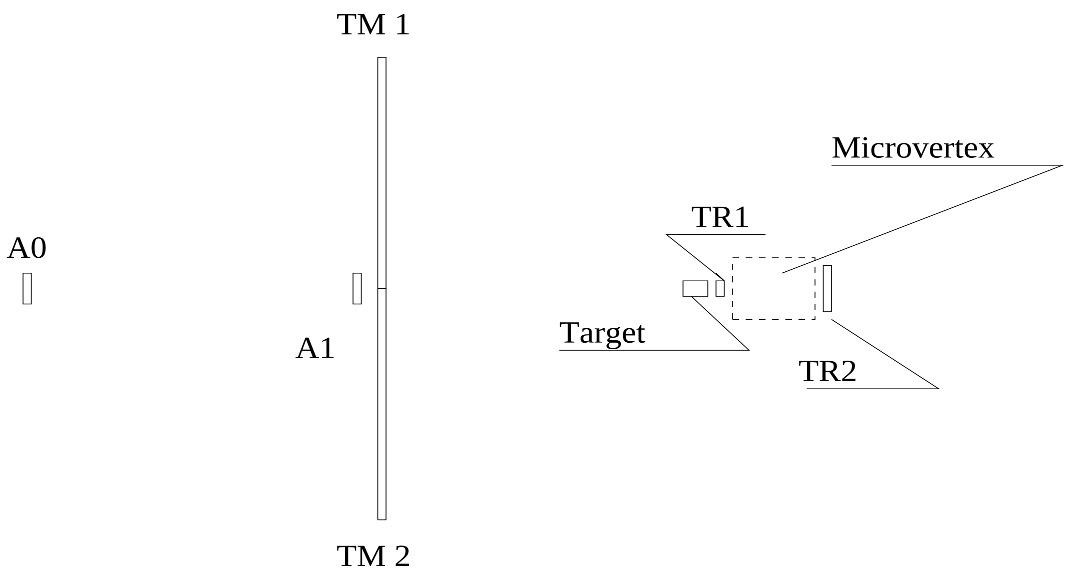

Figure 2.6.1 Diagram of the upstream trigger counters. A0, A1, TM1, and TM2 are veto counters. TR1 and TR2 detect charged tracks that pass through the microvertex.

The slower components of the trigger require time to sum energies or hits. The HC pad sum takes time to finish, and the FADC must have time to integrate. We also sum up the number of hits that occur outside the e^+e^- region in the chambers P1 and P0. The slower components are used to create a 2nd level trigger.

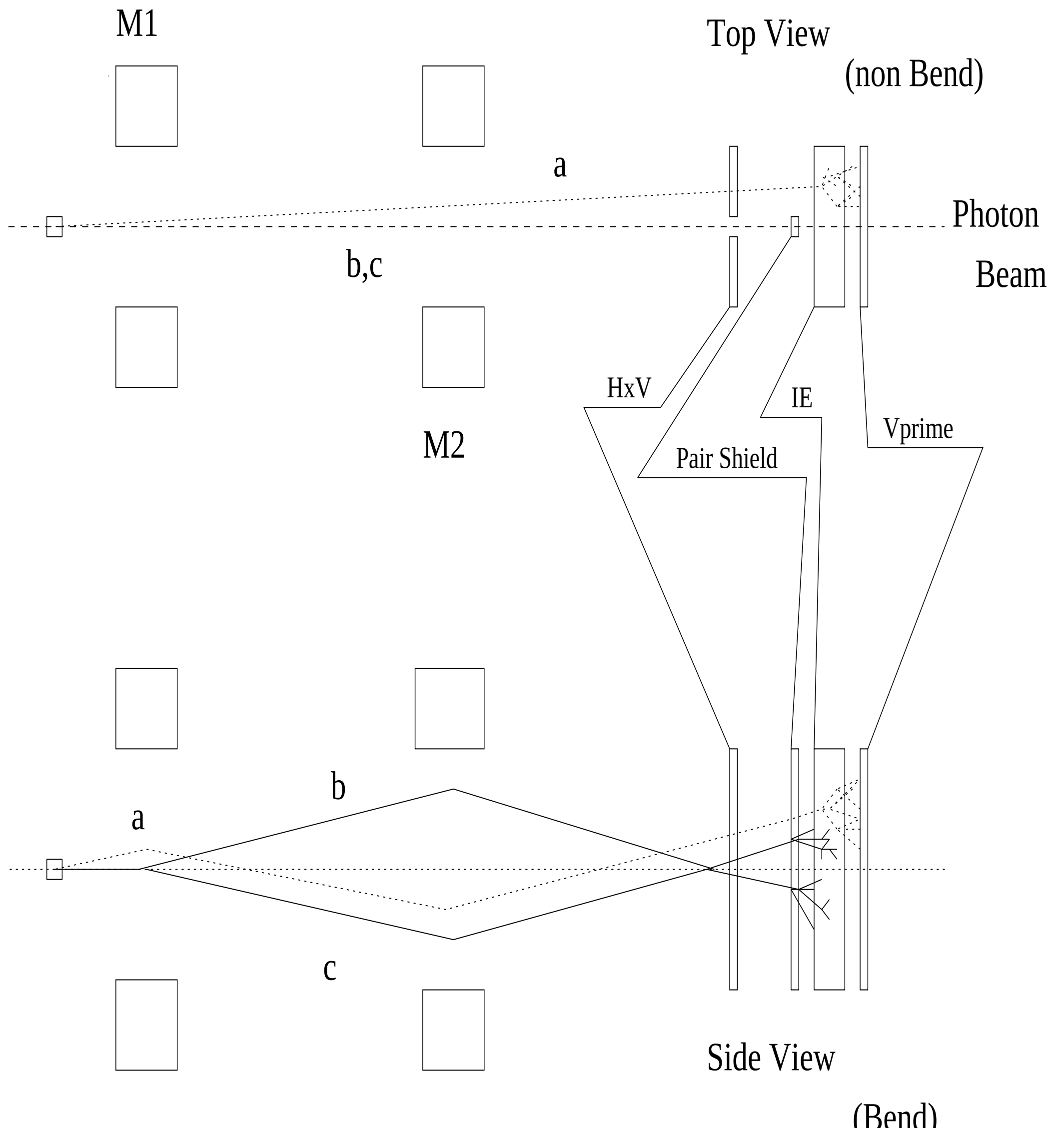

Figure 2.6.2 Diagram detailing the principle behind the combination of VPRIME and the IE pair shield. An electron(a) from a charm particle decay exits the target at an angle, is bent through the magnet(Side View) and penetrates the 25 radiation lengths of the IE to fire the VPRIME counter(efficiency for detecting electrons is momentum dependent). A Bethe–Heitler e^+e^- pair(b,c) exits the target along z, passes through the H and V gap and interacts in the lead pair shield. The extra 18 radiation lengths in the pair shield prevent showers from penetrating the IE to fire the VPRIME, and VPRIME is safe from IE *albedo* and soft particle contamination.

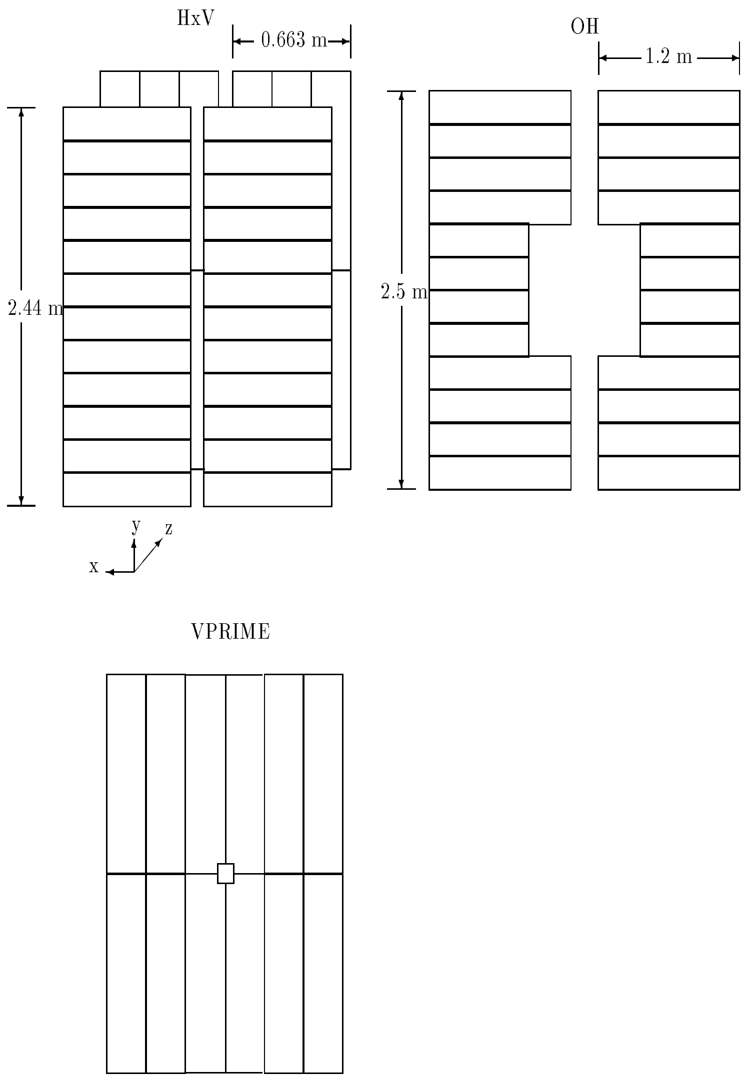

Figure 2.6.3 Counters of the H, V, VPRIME and OH arrays.

2.6.1 Master Gate

The on/off information from H and V(VPRIME in 1991) is used in coincidence to determine the number of particles that strike the arrays. If two particles (2body) strike the H and V(VPRIME), or one particle(1body) strikes the H and V(VPRIME) and one particle strikes the OH, we say that the event is consistent with the signature of an hadronic interaction.

In 1990 the Master Gate:

$$\mathrm{MG} = \mathrm{TR1} \cdot \mathrm{TR2} \cdot (\mathrm{H} \times \mathrm{V})_{\mathrm{2body}} \cdot \overline{(\mathrm{A0} + \mathrm{A1})} \tag{2.6.1}$$

was used for 26% of the run, and the Master Gate:

$$\mathrm{MG} = \mathrm{TR1} \cdot \mathrm{TR2} \cdot \Big[(\mathrm{H} \times \mathrm{V})_{\mathrm{2body}} + \big(\mathrm{OH} \cdot (\mathrm{H} \times \mathrm{V})_{\mathrm{1body}}\big)\Big] \cdot \overline{(\mathrm{A0} + \mathrm{A1})} \tag{2.6.2}$$

was used for the remainder of 1990.

In 1991 the Master Gate:

$$\mathrm{MG} = \mathrm{TR1} \cdot \mathrm{TR2} \cdot \Big[(\mathrm{H} \times \mathrm{V})_{\mathrm{2body}} + \big(\mathrm{OH} \cdot (\mathrm{H} \times \mathrm{V})_{\mathrm{1body}}\big)\Big] \cdot \overline{(\mathrm{A0} + \mathrm{A1})} \tag{2.6.3}$$

(with and without TM counters) was used for about 8% of the run, the Master Gate:

$$\mathrm{MG} = \mathrm{TR1} \cdot \mathrm{TR2} \cdot \Big[(\mathrm{H} \times \mathrm{V})_{\mathrm{2body}}\Big] \cdot \overline{(\mathrm{A0} + \mathrm{A1})} \tag{2.6.4}$$

was used for about 5% of the run, and the Master Gate:

$$\begin{aligned} \mathrm{MG} =& TR1 \cdot TR2 \cdot \\ & \Big[(H \times VPRIME)_{2body} + \big(OH \cdot (H \times VPRIME)_{1body}\big)\Big] \cdot \overline{(A0 \cdot A1)} \end{aligned} \tag{2.6.5}$$

was used for 86% of the run.

Other combinations were tried and their contribution to the overall data set is small.

2.6.2 2nd Level Trigger

The second level trigger(Trigger 7) used for this analysis was composed of:

$$\text{Trigger 7} = (\text{Multiplicity trigger} > 3) \cdot (\text{Pad sum energy} > 50\ GeV) \quad (2.6.6)$$

2.7 Data Acquisition

If the master gate is satisfied, an interesting event has occurred. The information from each detector is stored and the second level trigger is checked to confirm that a good event has occurred. If the second level trigger is satisfied, the event is stored in buffer memories for subsequent readout on magnetic tape.

While the 2nd level trigger decision is being made, there are $2\mu s$ for which we do not check the master gate. If the 2nd level trigger is satisfied, there is an additional $1.3ms$ wait for the event to read out to the buffer memories. If the 2nd level trigger is not satisfied, we clear the memories holding the detector information and the system waits for another master gate.

Since photons are delivered to the experiment for 20 seconds out of every 65 seconds, the buffer memories can fill during the photon delivery times and empty while the photon beam is off. During the 20 seconds of beam we average about 2×10^6 master gates and 3000 2nd level triggers. This corresponds roughly to 8 seconds of the 20 seconds of beam for which the experiment was not checking master gates. In 1991, the inclusion of the VPRIME and lead shield reduced the number of master gates by 1/2 with no loss in data quality. This corresponds to 2 extra seconds of beam for every 65 second cycle or 10% more data over the course of the 1991 run.

Experiment E687 wrote about 500 million events to tape during the 1990 and 1991 runs. Of this data, $\sim 70\%$ contained trigger 7's(there were other triggers as well, but they will not be discussed).

CHAPTER 3

RECONSTRUCTION

We can fully reconstruct an event using only a small amount of information. Tracks are formed from the information stored as pulse heights from the planes of the microstrip detector and as arrival times from the PWC's. Each hit is a point on a line, and in principle we need only connect the dots. We can gain some insight on the identity of a particle by the amount of light it creates in the Čerenkov counters; by the energy, width and length of a shower measured from the calorimetry information; by the invariant mass and location where a particle decays; and by the amount of shielding a particle can penetrate.

In this chapter we will describe how we recreate an event. In turn we will discuss the track reconstruction, the Čerenkov identification algorithm, the muon identification and, briefly, the calorimetry.

We will mention the main data reconstruction package and the code we use to reduce the amount of data for the final analysis.

Finally, the simulation of the physics processes and the detector response will be explained. Particular attention will be paid to the muon simulation.

3.1 Track Reconstruction

We take hits from planes that measure the same dimension, or view, and form two dimensional tracks, called projections, which are then formed into 3 dimensional tracks using projections from other views. Some or all projections or tracks can be used to find vertices. We use projections that measure slope changes in the bend view of the magnet to find particle momenta. Using the momenta and vertex location, we can reconstruct particles that decayed. A thorough explanation of the track reconstruction can be found in reference [16].

3.1.1 Microstrip Tracks

A charged particle passing through a silicon plane deposits energy in that silicon plane. The pattern of deposited energy in the microstrip detector is checked for clusters of deposition that result from secondary particle production(mainly δ rays) and/or leakage of the deposited ionization into other channels. The measured ionization is balanced so that the most likely position of a single "hit" is located and multiple possibilities are reduced. This aids the reconstruction process as the number of possible tracks that can be created is reduced.

Of the 4 planes in each view, we require a minimum of 3 planes to form a projection. A projection is formed by testing the hypothesis that a line is consistent with a given group of hits. We allow projections to share hits unless the projection is perfect(i.e. 4 planes have matched hits) in which case we do not share hits in the last three planes.

We group the projections together and test the hypothesis that they form a track. If the χ^2 per degree of freedom(DOF) for the hypothesis is less than 8, we say the projections form a track. Shared projections are arbitrated on the basis of the resultant track χ^2. Hits not used to make any tracks are combined to make space hits to search for wide angle tracks.

Clusters of tracks created due to the loose arbitrations employed in forming the projections and the tracks are further reduced to single equivalent tracks based on the shared hits and the degrees of freedom of the tracks.

The Monte Carlo determined efficiency of the algorithm is 96% and about 3% of all tracks reconstructed are spurious.

The resolution for a given microstrip track is a function of momentum, due to multiple Coulomb scattering, and a function of dimension, since the information from the microstrip system is biased to give redundant Y position information. We determine the resolution for tracks that pass through the high resolution region of the microvertex detector to be:

$$\begin{aligned} \sigma_x &= 11\mu m\sqrt{1+\left(\frac{17.5\ GeV/c}{p}\right)^2} \\ \sigma_y &= 7.7\mu m\sqrt{1+\left(\frac{25\ GeV/c}{p}\right)^2} \end{aligned} \tag{3.1.1}$$

3.2 Vertex Reconstruction

We need some rough vertexing information we can use later as a constraint for some types of particle reconstruction. To test the hypothesis that two or more tracks came from a point of common origin, we find the point where the transverse distance of closest approach is minimized. Specifically, we minimize:

$$\chi^2 = \sum_{i=1}^{n}\left(\frac{x-(x_i+x_i'z)}{\sigma_{x,i}}\right)^2 + \left(\frac{y-(y_i+y_i'z)}{\sigma_{y,i}}\right)^2 \tag{3.2.1}$$

where x_i' and x_i are the slope and intercept of the ith track and $x,\ y,$ and z are the fit parameters. The σ's represent the error on the track fit to the hits and do not include multiple scattering since we have no momentum information yet. A vertex finding algorithm that uses the full covariance matrix including multiple scattering is mentioned in the section "PASS1 and Skimming".

All the microstrip tracks in an event are initially tested. If the χ^2/DOF for the vertex hypothesis is greater than 3, tracks that contribute the most to the χ^2 are removed until the χ^2/DOF is less than 3. The removed tracks are then tested and so on until no more vertices can be made. We save the vertex locations for later use.

3.2.1 PWC Tracks

To reconstruct tracks from hits in the PWC chambers, we start by extending x, or non–bend view, projections from the microstrip tracks into the PWC system and looking for hits around the extension. Next, projections in the other views of the PWC system are found and matched to the x projection to form tracks. A track found in this way must have hits in the P0 x view; have at least 2 hits in each chamber with no more than 4 hits missing for the whole track; and have hits in at least the first 3 chambers.

Unused hits in the PWC x planes are then formed into projections and matched with the other projections to form new tracks.

A least squares fit is performed on all the PWC tracks found above. As fit parameters, we use the slope, intercept and, for tracks that pass through the aperture of the second analysis magnet, the change of the Y slope. A minimum χ^2/DOF is required for each track. Since we allow projections to share hits, arbitration must be performed to find the best PWC tracks. We arbitrate using both PWC and microstrip information. The procedure in described in the section "Linking".

If a track passes through the second analysis magnet and survives the χ^2/DOF cut, the rough change of the Y slope used in the fit is iterated to include the fringe field effects of the analysis magnets.

We can recover some track topologies we missed earlier. Lower momentum or wide angle tracks from the microstrip track reconstruction that extend through the first, second and third chamber; through the first and second chamber; or just through the first chamber are recovered. A minimum of three hits per chamber are required for the first two cases, and the tracks found that extend through P0 only are required to have all 4 hits.

The efficiency of the PWC track reconstruction algorithm is better than 98% with only 0.5% of tracks being spurious ones. The efficiency is determined using a Monte Carlo simulation where each plane's efficiency is accounted for, but the added noise present in the real system is not. From the analysis of the data, we found it necessary to limit the number of reconstructed tracks to 30. Since noise in the PWC system increases the number of spurious tracks formed, the limitation on the maximum number of tracks allowed dramatically reduces the reconstruction time. As the reconstruction package is biased towards finding the best tracks first, the noise has a small impact on most categories of tracks and is corrected for in the Monte Carlo.

3.2.2 Linking

We again exploit the x view projections to arbitrate our PWC tracks that share hits and choose the PWC tracks that are most likely extensions of microstrip tracks. This is an important part of reconstruction since a link will give us information on the particle momentum via the bend in M1, and PWC tracks not linked to microstrip tracks are available for use in reconstructing particles that decay downstream of the microvertex detector.

The x projections of PWC tracks are extrapolated to the center of M1 where the slopes and projections of these tracks are tested for consistency against microstrip tracks extrapolated to the center of M1. A first pass with loose cuts is made to remove unreasonable links. The surviving candidate linked tracks are then refit using hits in both the microstrip and PWC systems. We arbitrate links based on the χ^2/DOF returned from the fit. We allow a maximum of two PWC tracks to be linked to a microstrip track. A double link is possible in events where the sum of the masses of the individual particles is close to the mass of the decaying particle and events due to Bethe–Heitler production.

The linking efficiency is $\sim 94\%$ for high momentum 3 chamber tracks and $\sim 98\%$ for high momentum 5 chamber tracks. There is a reduction in linking efficiency at lower momenta due to Multiple Coulomb scattering, particles that interact catastrophically with material in the detector downstream of the microstrip system and particles that decay downstream of the microstrip system.

3.2.3 Momentum Determination

We have all the position information on reconstructed tracks. For linked tracks, we can make a momentum determination from the bend measured as the track passes through M1. If there was no link and the track did not pass through M2, we assume the particle was created at one of the vertices found earlier. We trace the x projection of the track back to the target and choose the vertex closest to the projection, or, if no vertex is present, we assume the particle was created in the center of the target. We determine the momentum resolution for tracks that pass through the magnets to be:

$$\begin{aligned}\frac{\sigma_p}{p} &= 3.4\%\left(\frac{p}{100GeV/c}\right)\sqrt{1+\left(\frac{17\ GeV/c}{p}\right)^2} \quad \text{for M1}\\ \frac{\sigma_p}{p} &= 1.4\%\left(\frac{p}{100GeV/c}\right)\sqrt{1+\left(\frac{23\ GeV/c}{p}\right)^2} \quad \text{for M2}\end{aligned} \tag{3.2.2}$$

The momentum dependent term is due to multiple Coulomb scattering.

3.2.4 Vees

Since the lifetime of the particles K_s^0 and Λ are two to three orders of magnitude longer than typical charm lifetimes, we need the ability to reconstruct these particles over a larger volume of the spectrometer. We have several schemes for reconstructing these decays which we call vees. Particle identification is relaxed for these searches, but we assign the highest momentum particle the proton mass if the Λ mass hypothesis is tested.

The vee category with the best resolution is a decay which occurs upstream of the microvertex with two linked tracks. We simply test the vertex hypothesis, albeit this time multiple scattering effects are included, for pairs of oppositely charged tracks and form an invariant mass. A cleaner signal is found when we use the vee momentum vector to seed the search for a primary vertex and require the vee vertex to be separated from the primary vertex found.

We can search for other vees with microstrip information by extrapolating unlinked PWC tracks back to the microvertex detector. Unused hits in the last two stations of the microvertex are tested to see if there is enough information to warrant a refit of the track. If so, the hits are included and the track is refit. Pairs of oppositely charged tracks with additional information are subject to a vertex test which also serves to arbitrate tracks that share hits. An invariant mass is formed and if the candidate is sufficiently close to the K_s^0 or the Λ mass, the candidate is retained.

The next category of vees reconstructed are those which decay in M1. We use x and y projection information to form a vertex hypothesis, but we need to find the momentum for various categories of M1 vee tracks to form an invariant mass.

If an M1 vee is composed of two 5 chamber tracks, we have momentum solutions for both tracks and an invariant mass test can be performed.

If one of the vee tracks is a 3 chamber track, we know the y location of the vertex via the momentum measurement of the 5 chamber track and can find the momentum of the 3 chamber track iteratively. An invariant mass test can then be used.

If both of the vee tracks are 3 chamber tracks, we assume the vee was created at the highest multiplicity (primary)vertex that we formed earlier using microstrip tracks with no multiple Coulomb scattering considerations. The transverse momentum of the vee is balanced and all unknowns are determined.

We now subject the surviving candidates to a fit using all the information available including multiple scattering effects and requiring pointback to the primary vertex.

Some M1 Λ vees are lost because a poor link succeeds for one of the vee daughters. For these categories we allow one track of the vee to be linked. We improve this signal with cuts on momenta and Čerenkov identification. These categories of vees are used in the analysis of the Ξ^- and the Ω^-.

Vees that decay between P0 and P2 are reconstructed with unused clusters of hits in the chambers. X projections are formed and pairs of projections are checked to see if they intersect between P0 and P2. The other projections are then matched with the x projection to find tracks. At least 3 hits must be present in any chamber if less than 4 chambers are used. If the tracks are found with four chambers, we allow one of the chambers to be missing. The categories thus found are P2–P3 tracks, P1–P2–P3 tracks, P2–P3–P4 tracks and P1–P2–P3–P4 tracks. Again, various methods are employed to determine momenta and the vees are subject to vertexing, invariant mass and pointback requirements and are arbitrated on the basis of these requirements.

3.2.5 Kinks

Sometimes a decay downstream of the microvertex detector will not leave a vee(2 charged particles). The decays $\Sigma^+ \rightarrow p\pi^0$, $\Sigma^+ \rightarrow n\pi^+$ and $\Sigma^- \rightarrow n\pi^-$ are reconstructed using the unlinked track as a hypothesis for the Σ in the microvertex and matching it to an unlinked PWC track.

We take the x projections and search for an intersection of the projections. If the projections meet between the downstream end of the microvertex detector and upstream end of P0, we determine the momenta of the particles if possible.

If the PWC track is a 5 chamber and the intersection is upstream of M1, we can infer the momentum of the Σ by solving the kinematic equations for the decay. This procedure leaves a two–fold ambiguity in the Σ momentum. We can reduce background at this point by requiring the extrapolated y position of the PWC track be within 25 mm of the y position of the vertex as determined from the y information of the Σ track.

If the PWC track is a 5 chamber and the intersection is located within M1, we trace the PWC track back to the intersection point and iterate the Σ

momentum until the y intersection is minimized. We again solve the kinematic equations for the decay, but this time we break the kinematic ambiguity by choosing the solution closest to the momentum we got by the minimization process.

If the PWC track is a 3 chamber, we consider those decays that occur upstream of M1 only. The y position of the vertex is determined from the y information of the Σ track and the x projection's intersection in z, and we can determine the PWC track momentum from the vertex position.

3.3 Čerenkov Algorithm

We can check the identity of a particle by seeing whether or not the particle created Čerenkov light in our Čerenkov counters.

We calculate how much light is expected in each cell for a given track and particle hypothesis. Each cell expected to receive some Čerenkov radiation is checked to see whether or not it has a phototube signal above threshold. If one of the cells has a signal, we say the track is on. If all the cells are off, the track is off. Often, the cone of expected Čerenkov radiation from other tracks shares cells with the track we are checking. If there are no cells that are unshared for a track and the shared cells are on, we say that the Čerenkov identification is confused. We do allow a small amount of confusion to exist which results in a bias towards calling a track on that was otherwise off.

Using the track momentum and the threshold in a given counter for a given particle type, we form a particle hypothesis that the track is either an electron, a pion, a kaon or a proton. Next the status of each track for each Čerenkov counter is used to either confirm or deny each hypothesis. Čerenkov counters with a confused status are not used in the decision making, and C3 is not used for 4 chamber, or less, tracks. If counters contradict each other we say the Čerenkov identification is inconsistent. A code(ISTATP) is assigned based on the outcome of the particle hypothesis test. Table 3.3.1 is the list of possible ISTATP codes.

Table 3.3.1 Čerenkov Identification Code ISTATP

Code(ISTATP)	Hypothesis Consistent with
0	Inconsistent
1	$e^{\pm}$
2	$\pi^{\pm}$
3	$e^{\pm},\ \pi^{\pm}$
4	$K^{\pm}$
6	$\pi^{\pm},\ K^{\pm}$
7	$e^{\pm},\ \pi^{\pm},\ K^{\pm}$
8	$p^{\pm}$
12	$K^{\pm},\ p^{\pm}$
14	$\pi^{\pm},\ K^{\pm},\ p^{\pm}$
15	$e^{\pm},\ \pi^{\pm},\ K^{\pm},\ p^{\pm}$

The bias towards calling a cell "on" results in a loss of efficiency for heavy particles(K's, p's) with a resulting decrease in misidentification for heavy particles. Since most of the charm particles we study contain heavy particles and most of the background is dominated by pions, the bias toward clean heavy identification is useful. This is especially true for charm mesons since decays into states containing kaons (mainly categories 4,7 and 12) are highly favored.

3.4 Muon Identification

The muon identification is accomplished by projecting PWC tracks onto the inner muon system and by searching a 3σ scattering radius for hits in the detectors of the inner muon system.

The outer muon system was not used in this analysis and is still under investigation.

3.4.1 Calibration

We stop the proton beam in a steel block upstream of the experimental hall and look at muons that penetrate the shielding. This gives us a broad spectra of muons with which to test the inner muon system. The muons are traced to the inner muon system using the PWC's and the multiple scattering for a muon at a given momentum and plane location is determined. This method for determining the scattering becomes inefficient at lower momentum due to energy loss. We choose to accept the loss at low momentum but can recover a fraction of the loss with looser identification requirements. Figure 3.4.1 is the single track efficiency for the inner muon system in the 1990 configuration we expect using the simulation.

3.4.2 Matching Hits

Once the scattering radii are determined, we can project candidate tracks onto each plane and search a 3σ zone around the projection for any hits. If hits are found, the track has made a match for that plane. More than one track can match to the same hit, but if more than one match is found in a proportional tube plane for a track, the closest hit is kept for later reference.

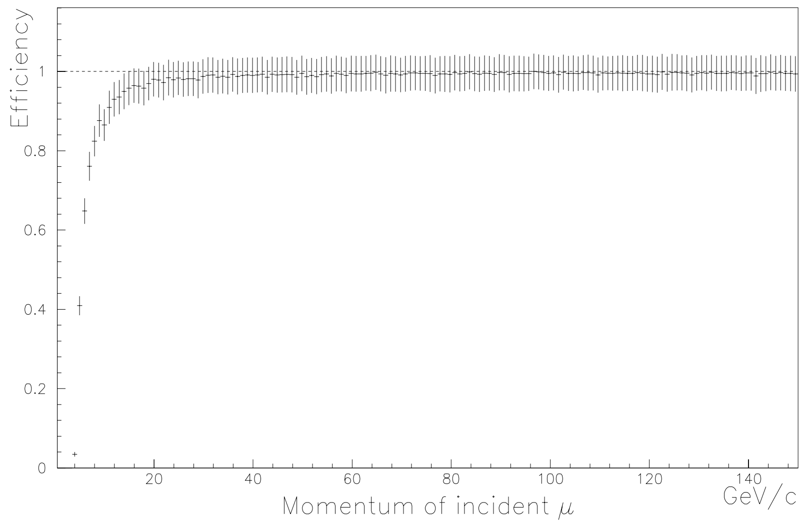

Figure 3.4.1 Expected efficiency vs muon momentum for the 1990 muon system.

3.4.3 Identification Code

If a track has matched 5 or more planes out of a possible 7, we consider it a muon and we assign it a code based on its shared hits history.

Table 3.4.1 Muon Identification Codes

Code(IDMU)	Meaning
4	3 shared hits 4 unshared hits
3	2 shared hits > 2 unshared hits
2	1 shared hit >1 unshared hits
1	0 shared hits Muon definite
0	Not a Muon
-1	1 shared hit ≤1 unshared hits
-2	2 shared hits ≤2 unshared hits
-3	>2 shared hits <4 unshared hits

In practice, if IDMU$\neq 0$ we call the track a muon.

3.4.4 Low Momentum

Below 30 GeV/c, some particles do not reach the second bank. It is possible to have muons that penetrate only to the first bank of the inner muon system or that have scattered outside the 3σ search zone by the time they reach the second bank. This is due in a large part to energy loss in the absorption material. Due to the low level of misidentification in the original muon system, the identification requirements for a particle below 30 GeV/c were relaxed so that a previously lost muon could be recovered if it matched 3 or 4 planes in the first bank. In 1991, these muons were not used since the level of misidentification seen using only the first bank of muon counters was large. In Figure 3.4.2 we demonstrate the expected gain in efficiency at low momentum for the 1990 inner muon system using the simulation.

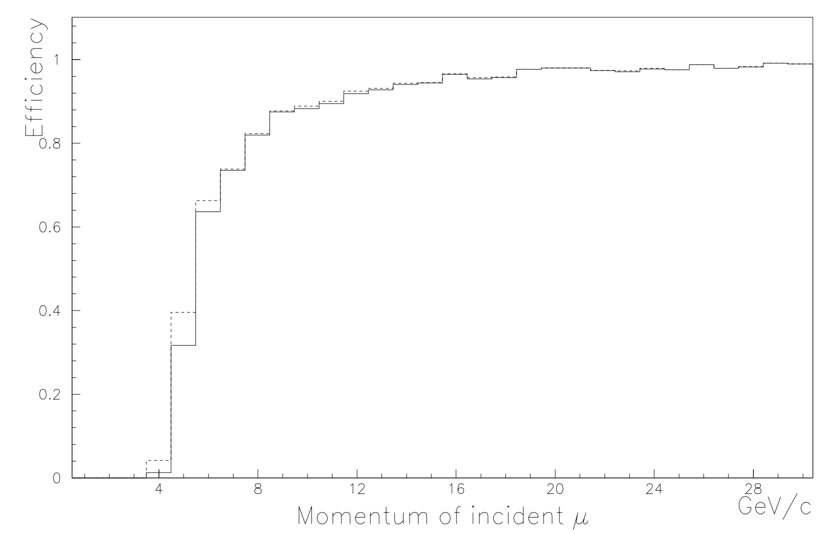

Figure 3.4.2 Expected efficiency vs momentum for the 1990 muon system. The boost in efficiency for accepting low momentum muons is shown as a dotted line.

3.4.5 Dropped Hits

Sometimes, the number of hits in the inner muon system is large. If there are more than 20 hits in any single plane of that system, we drop all the hits from that particular plane. While this is not a problem in the original configuration, we find that a lost plane occurs for about 5% of events in the 1991 data where a muon is present. This effect is simulated and is explained in the Monte Carlo section.

3.5 Muon Misidentification

If we have random noise in the muon system, the probability that a given track will have an accidental match is related to the search radius used. If the noise is related to a particle decaying into a muon, the hits from the resultant muon can lead to the particle being misidentified as a muon.

The goal of determining the behavior and magnitude of muon misidentification is to determine the amount of misidentified signal in a particular analysis. To accomplish this task we use the muon code as a *veto*. Basically, we reanalyze our signal requiring IDMU=0 and reweight the signal that results with our misidentification probability. In this way, we have a true representation of the background due to misidentification in our signal of interest. The method is appealing since we do not have to worry about choosing specific background modes to model, nor do we have to model any complicated production dynamics associated with any particular background.

3.5.1 Sources of Misidentification

The majority of misidentification in the muon system occurs due to hadron(mostly pion) showers penetrating the absorption material. We demonstrate this by examining data where an incident pion beam is used as a calibration tool. It is possible to use the Hadron Calorimeter to look at the amount of energy deposited by a particle traversing that detector. We look at the E/P for particles identified as muons and compare it to the expected E/P for a pion. The amount of data consistent with a pion E/P only and identified as a muon is the amount of misidentified signal. The total amount of pion consistent only data is the normalization signal. In Figure 3.5.1 we show some typical plots of Hadron Calorimeter response.

The amount of misidentified signal due to punch through that we find agrees well, see Figure 3.5.2, with a study done by another group using a similar system.[20]

The other source of misidentification is due to particles that decay into a muon. This accounts for $\sim 15\%$ of the total pion misidentification. We can limit this background to some extent by requiring good PWC–microstrip track links, momentum agreement between the two magnets and good vertex confidence levels.

In the 1991 muon system configuration, a new source of noise was created for tracks below 30 GeV/c (those that use the first bank of the inner muon system only for identification). Presumably, these tracks are misidentified due to beam halo associated with transporting a photon beam through the muon system. In 1991, we discarded muons below 30 GeV/c if there were less than 5 planes matched. In Figure 3.5.3 we see that removing this category of muons significantly reduces misidentification.

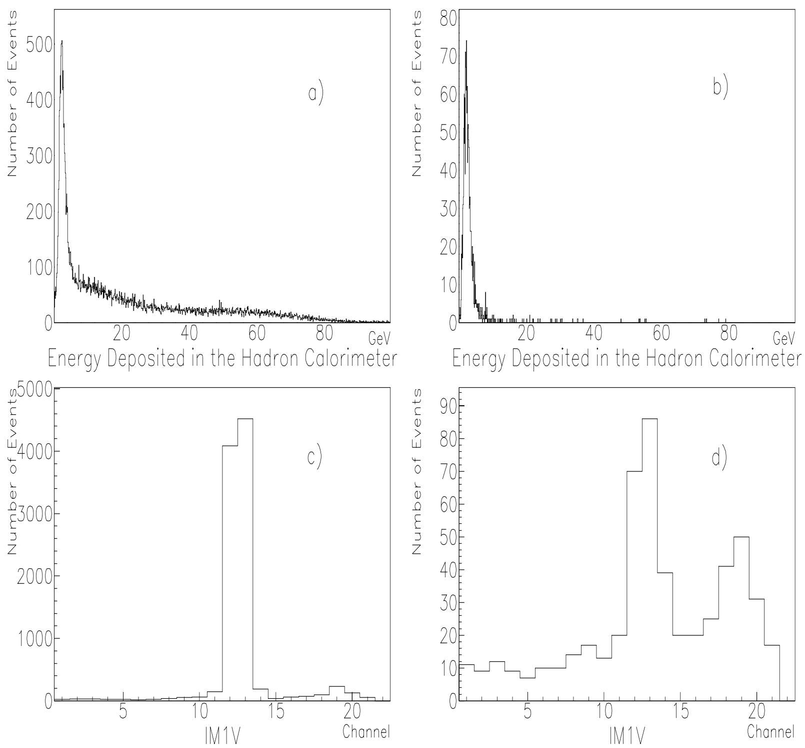

Figure 3.5.1 Plots used in the punch through analysis. a)Energy deposited in the HC for $\sim 50\ GeV/c$ pions in the HC, b)Energy deposited in the HC for $\sim 50\ GeV/c$ muons in the HC, c) distribution of hits in IM1V for "pions" with IDMU$\neq 0$ and d) distribution of hits in IM1V for "pions" with $\frac{E_{HC}}{P} > .3$. Plot d) demonstrates that showers in the HC are distributing hits throughout the muon system.

3.5.2 Parameterization of the Misidentification Probability

We use high statistics decays of $K_0^s \rightarrow \pi^+\pi^-$ and $\phi \rightarrow K^-K^+$ to determine the amount and position dependent behavior of the muon misidentification. We use Monte Carlo to determine the actual shape used in fitting the amount of misidentification vs. momentum.

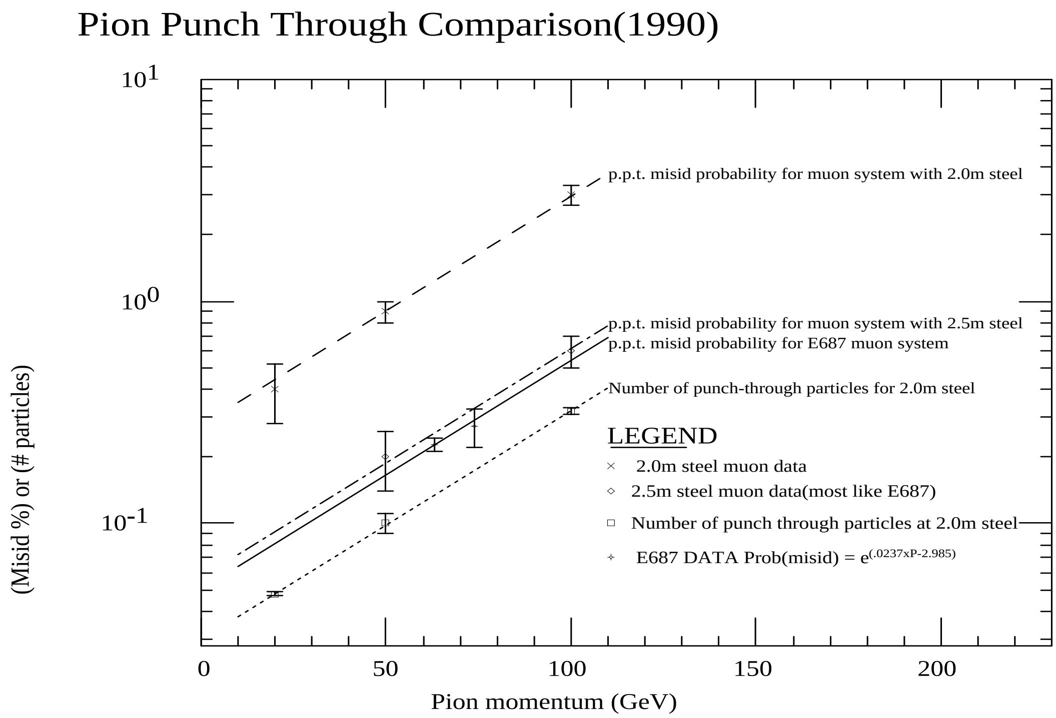

Figure 3.5.2 Plot comparing our level of hadron penetration to a similar system.[20]

In a uniform muon system dominated by random noise, we need only reweight data by its incident momentum to get the misidentification probability. In the 1991 configuration the hole in the muon system presented a special challenge. We have to examine the position dependence inherent in the 91 system. If we assume that the misidentification probability is a separable function of position and momentum,

$$P(misid) = G(x, y)H(p), \tag{3.5.1}$$

we can use the position dependent information from 1990 and 1991 misidentification via $\phi \rightarrow K^-K^+$ decays to provide a transform between 1990 and

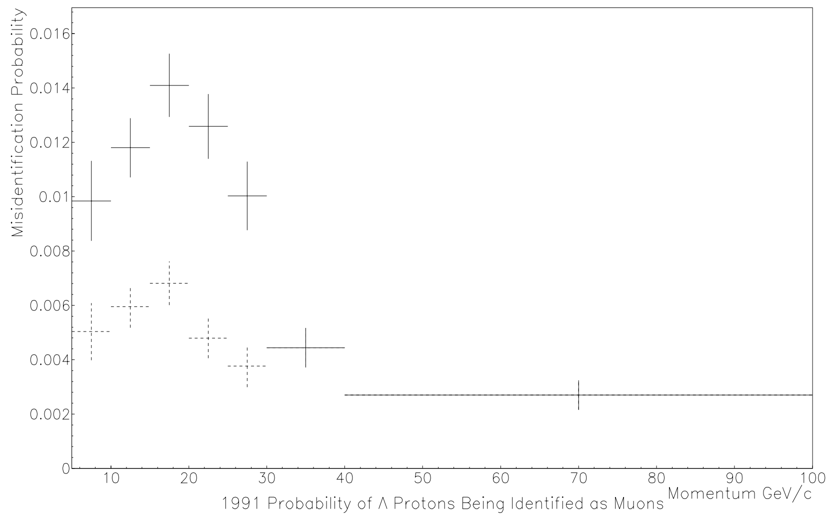

Figure 3.5.3 Proton misidentification vs. momentum for 1991 data. The dashed histogram is the effect of requiring 5 or more planes for a good muon at all momenta.

1991:

$$G_{transform}(x, y) = G_{91}(x, y)/G_{90}(x, y). \tag{3.5.2}$$

Figure 3.5.4 is the display of this transform.

Therefore, we can predict the 1991 momentum behavior using the 1990 momentum behavior and the x,y behavior in 1990 and 1991:

$$H_{91}(p) = (G_{91}(x, y)/G_{90}(x, y))_{\phi} H_{90}(p) \tag{3.5.3}$$

In Figure 3.5.5 we examine the validity of the transform method.

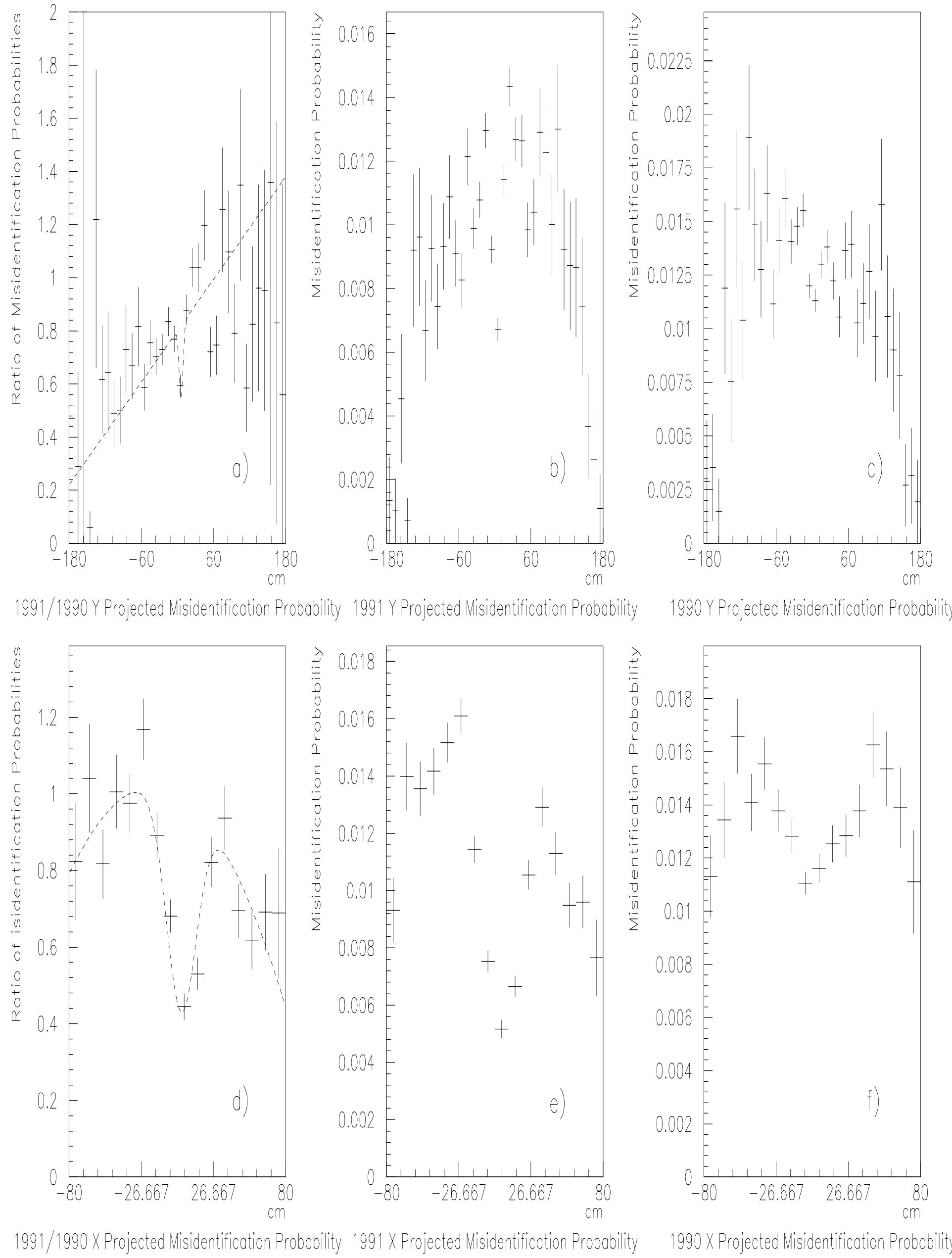

Figure 3.5.4 Misidentification of kaons from ϕ's. Series of plots showing the projections in X and Y at IM1V of a) the 1991/1990 Y transform with fit, b) the 1991 Y projected misidentification, c) the 1990 Y projected misidentification, d) the 1991/1990 X transform with fit, e) the 1991 X projected misidentification and f) the 1990 Y projected misidentification.

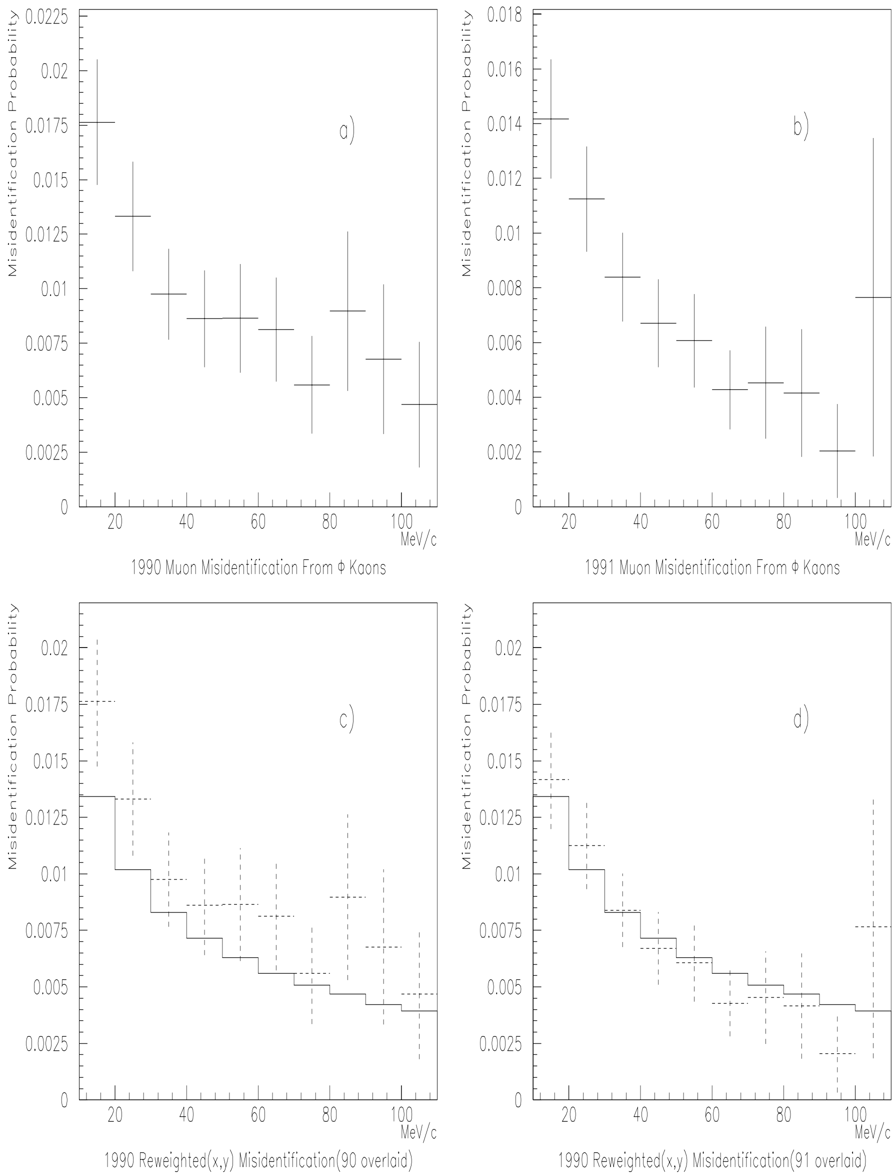

Figure 3.5.5 Effect of transform in X and Y. These plots show the predictive power of the transform in Figure 3.5.4. The 1990 kaon misidentification probability spectra in a) is used to predict the 1991 misidentification probability spectra in b). Figure c) is the transformed 1990 kaon misidentification probability spectra plotted against the 1990 kaon misidentification probability spectra. Figure d) is the transformed 1990 kaon misidentification probability spectra plotted against the 1991 kaon misidentification probability spectra. Agreement is excellent.

We can bolster our knowledge of the momentum dependent misidentification probability using both 1990 and 1991 data:

$$H_{90}^{\pi}(p) = H_{91}^{\pi}(p)\frac{H_{90}^{K}(p)}{H_{91}^{K}(p)} \tag{3.5.4}$$

In Figure 3.5.6 we use the assumption that the 1991 muon system is a transformed 1990 system to improve our momentum dependent misidentification probability.

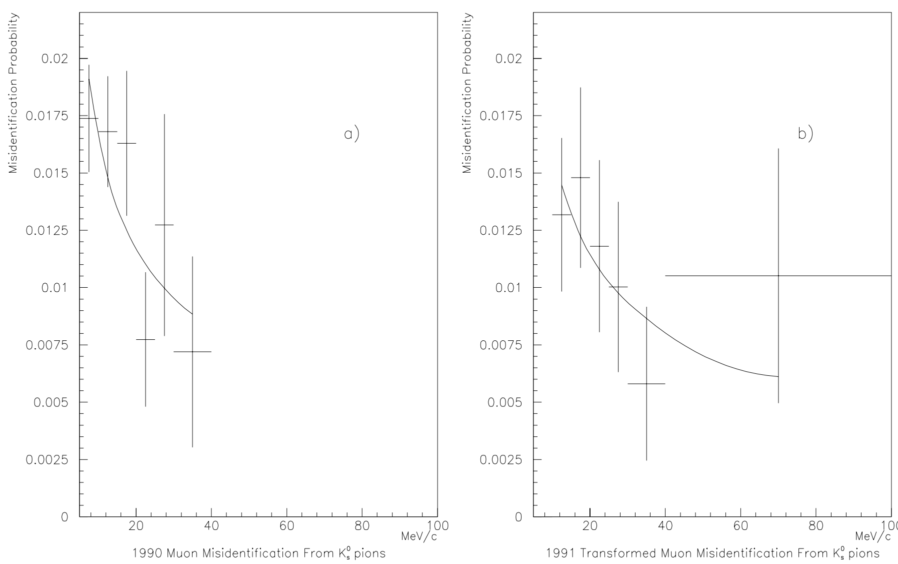

Figure 3.5.6 The fit, a), to 1990 pion misidentification spectra and the fit, b), to the momentum transformed 1991 pion misidentification spectra.

$$H_{90}^{\pi}(p) = \frac{.052 \pm .0044}{\sqrt{p}}, H_{91}^{\pi}(p)\frac{H_{90}^{K}(p)}{H_{91}^{K}(p)} = \frac{.0515 \pm .0073}{\sqrt{p}} \tag{3.5.5}$$

$$H(p) = \frac{.052 \pm .0038}{\sqrt{p}} \tag{3.5.6}$$

3.5.3 Estimating the Contribution to a Real Signal

Now all we need do is run on a skim tape and require that our "muon" pass all our usual cuts but have IDMU=0. We then use the amount of $K\pi$ from the same tape to estimate how much to boost the misid sample so that it is representative of the whole run. The amount of boost is larger in 1991 due to the larger sample of data. The amount of boost is:

$$Boost_{90} = 7.21 \pm .74, Boost_{91} = 13.24 \pm 1.69 \tag{3.5.7}$$

And the final weighting function for misid events from the skim is:

$$F_{90}(misid) = \frac{.375 \pm .057}{\sqrt(p)}, F_{91}(misid) = \frac{.688 \pm .13}{\sqrt(p)} G(x,y) \tag{3.5.8}$$

The reweighting formula is applied to particles with IDMU $= 0$ that pass all cuts the IDMU $\neq 0$ particles did and end up in the final sample.

3.6 Calorimetry

Here we will touch on aspects of the calorimetry. The full and proper electromagnetic calorimetry reconstruction was not available in time for this analysis. There was also no information available on energy reconstructed from charged tracks in the hadron calorimetry available for this thesis.

3.6.1 Electromagnetic Calorimetry

The Outer Electromagnetic calorimeter reconstruction package will not be discussed. Clean signals have been isolated using this detector, but the simulation is still under investigation.

Energy is reconstructed in two ways in the Inner Electromagnetic Calorimeter. Clusters of deposited energy are formed into showers that can be matched to tracks, and tracks can be used as seeds for energy reconstruction.

We reconstruct π^0's from clusters not associated with tracks, and we identify electrons based on the amount and profile of the energy reconstructed. Aspects of the reconstruction are still under investigation.

3.6.2 Hadronic Calorimetry

If a track can be extrapolated to the front of the HC, the towers around the expected position of the resultant shower are summed and an energy is calculated. The energy reconstructed for charged tracks in the HC(or CHC(s)) was not stored in our reduced data sample and was not available for later analyses.

We can also use the HC to discriminate solutions resultant from the Kink analysis for kinks with neutrons. If there is energy deposited in the HC in the expected position for one of the solutions in the kink analysis, the solution is favored.

3.7 PASS1 and Skimming

We combine the reconstruction algorithms together in one package and form reconstructed data from raw data. The process is very CPU intensive. The process was accomplished during the period from November 1991 to August of 1992 using the IBM and SGI parallel computing resources at Fermilab. About 1 terabyte of raw information was turned into 2 terabytes of reconstructed information. We used a second package based on physics motivations to reduce the data set.

In this analysis, we use the part of the data reduction package, called the *skim*, that identifies separated vertices. The vertices are constructed using the full covariance matrix for the tracks involved. The covariance matrix includes effects from multiple scattering and the fit of the track to the hits. The skim we use is called the Global Vertex skim, and the use of the skim reduces the amount of information used in this analysis to about 20 gigabytes. A more complete description of the Global Vertex skim can be found in Chapter 4.

3.8 Monte Carlo Simulation

Now that we have gone to the trouble of collecting and reconstructing the raw data, we have to recreate artificial data to simulate our efficiency losses. Typically, an order of magnitude more simulated data is used than real data for this purpose.

We have to simulate the production of charm particles, the detector responses and the physics processes that affect particle trajectories. We will briefly mention some of the more prominent features of the Monte Carlo with special emphasis on the muon simulation.

The Monte Carlo can be split into two packages. We have a package that creates charm particles(GENERIC) and a package that traces the created particles through the spectrometer(ROGUE).

ROGUE is separated into parts that coincide with different running conditions. We used different targets, different trigger thresholds, chamber efficiencies changed, and the muon system was inoperable for part of the 1990 run due to a data acquisition error.

3.8.1 Production Model(GENERIC)

To create charm particles we use the LUND[19] package. The specific implementation is discussed in the systematics chapter.

3.8.2 Running Periods(ROGUE)

In all we have 10 distinct running periods for the 1990 and 1991 runs. In Table 3.8.1 we list the different periods and the reason for a period change.

The time dependence of the 1991 muon system is handled in the muon simulation.

Table 3.8.1 Running periods

Period	description
1	Start of 1990 run
2	2nd level trigger change
3	New 2nd level triggers, chamber efficiency change
4	Beginning of good 1990 muons
5	Master Gate change
6	11 segment target
7	Master Gate change
8	End of good 1990 muons
9	1991 running
10	change in chamber efficiency

3.8.3 Particle Tracing

To trace particles through the detector, we slice the detector in z, and each slice is called a *stop*. For each stop we can check the particle status and the probability for any physics process to occur. Table 3.8.2 lists the reasons to stop a particle for a check.

Table 3.8.2 Types of *Stops*

Stop description
assign energy deposited in a detector
assign hits to a detector
inside detector acceptance
outside experiments acceptance
stop particles due to interaction with material
multiple Coulomb scattering
photon conversion to e^+e^-
hadronic interaction
hadronic scattering
Čerenkov light deposited
electron bremsstrahlung
muon energy loss and scatter

If a particle is predicted to decay before going outside of the detector acceptance, we perform all the stops until the particle decays. If a particle decays in a Čerenkov counter, we recompute the light deposited based on where the particle decayed and what the decay products are. If the particle decays in a magnet, we perform the magnetic trace until the particle decays, then we perform the trace for any charged decay products.

Particles with momentum less than 100 MeV/c are not traced, and we eliminate neutrinos from the trace.

3.8.4 Data Triggers

If a charged track goes through one of the counters in $H \times V(V')$ or OH we generate a random number and compare it to the predicted efficiency of the counter. If the random number is less than the efficiency, we say the counter is *on*. After all tracing is completed, the signals from the counters that were turned *on* are fed into a software simulation of our Master Gate.

The simulation of the hadron trigger is more complicated. We sum the momenta of all neutral and charged hadrons that impinge on the front of the HC. Electrons are specifically excluded from the energy sum, but muon minimum ionization energy is included. From data, we know the probability for the HC busline to turn on for the summed momenta of hadrons and minimum ionizing energy of muons incident on the HC. We generate a random number and compare it to the efficiency as was done for the Master Gate simulation.

The multiplicity trigger counts the number of tracks that pass through the chambers P0 and P1 outside the region (± 8 cm in x) in which most of the $\gamma \rightarrow e^+e^-$ events are expected to occur and assigns a probability based on the efficiency determined by data for that trigger to be satisfied. A random number is generated to determine the status.

Our simulated trigger is the logical *and* of the Master Gate, the HC trigger and the multiplicity trigger:

$$Master\ Gate \otimes HC \otimes Multiplicity \tag{3.8.1}$$

3.8.5 Microstrip Simulation

If a particle is traced through a microstrip plane, charge is deposited according to a Landau distributed energy function. Charge sharing is allowed as in real data. Broken channels, electronic problems and noise are simulated as well.

3.8.6 Chamber Simulation

As a particle is traced through the detector, the location at which the particle intersected a PWC plane is stored. After the tracing is complete, we use the locations to assign hits in the PWC planes. Hits, spurious hits and adjacencies (hits in more than one wire per track) are assigned to each plane through which a charged particle passed. Each hit and spurious hit are checked for efficiency. If a hit is lost due to inefficiency, the adjacencies are lost as well. Hits and spurious hits are then stored for later use in the reconstruction of the simulated data.

3.8.7 Čerenkov Simulation

If a charged track exceeds the momentum necessary to produce Čerenkov light in a given Čerenkov counter for that particle, photons are generated at an angle determined by the momentum and particle type along the particle path.

The photons from the particle are then traced to the mirrors at the end of the Čerenkov counter. If a photon hits a mirror, it is reflected into a cell and an efficiency is assigned based on the path the photon took to get to the cell and the cell efficiency. If the photon passes a random number test, a signal is registered in the photomultiplier tube for the photon. The signal is based on the response of each photomultiplier tube and is Gaussian distributed about the mean response for a detected photon for that tube.

3.8.8 Muon Monte Carlo

Simulated muon tracks are scattered through the material in the downstream part of the inner E687 spectrometer. If a track reaches the inner muon system after energy losses and multiple Coulomb scattering, hits are assigned in a detector plane based on the scattered position of the simulated muon track at the detector plane and the efficiency of the counter hit in that plane. Figure 3.8.1 is a diagram of the more salient features needed to model multiple scattering.

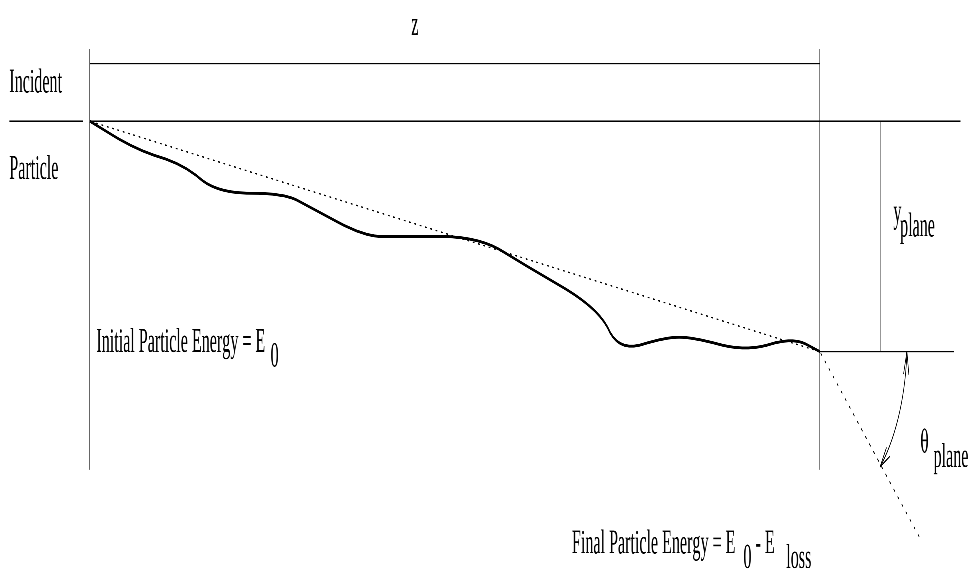

Figure 3.8.1 Diagram of multiple scattering in the plane of the paper. Pertinent variables used in the scattering formulae are labeled in the figure.

The muon simulation exploits the following formulae for scattering and energy loss:

$$\theta_0 = \frac{0.0136\ GeV}{\sqrt{(E_0(E_0 - E_{loss}))}}\sqrt{R}\,(1 + 0.038\log(R)) \tag{3.8.2}$$

$$y_{plane} = r_1 z\theta_0/\sqrt{12} + r_2 z\theta_0/2 \tag{3.8.3}$$

$$\theta_{plane} = r_2\theta_0 \tag{3.8.4}$$

where

θ_0 = Gaussian width of scattering angle for particle traversing R radiation lengths

E_0 = initial particle energy

E_{loss} = energy lost by particle traversing R

R = thickness of material traversed in radiation lengths

r_1 = Gaussian random number $\sigma = 1$

r_2 = Gaussian random number $\sigma = 1$

z = thickness of material traversed in centimeters

y_{plane} = lateral displacement in the y,z plane after scattering

θ_{plane} = angular displacement y,z in the plane after scattering

Since we have many scattering stops for each track that is simulated, it is sufficient to replace the Gaussian random number by a random number that covers the range $\pm\sqrt{12}$.

The performance of the simulation is excellent. In Figure 3.8.2, we show the identification probability for a particular muon run overlaid with the expected response from the muon simulation for that run in the 1991 configuration.

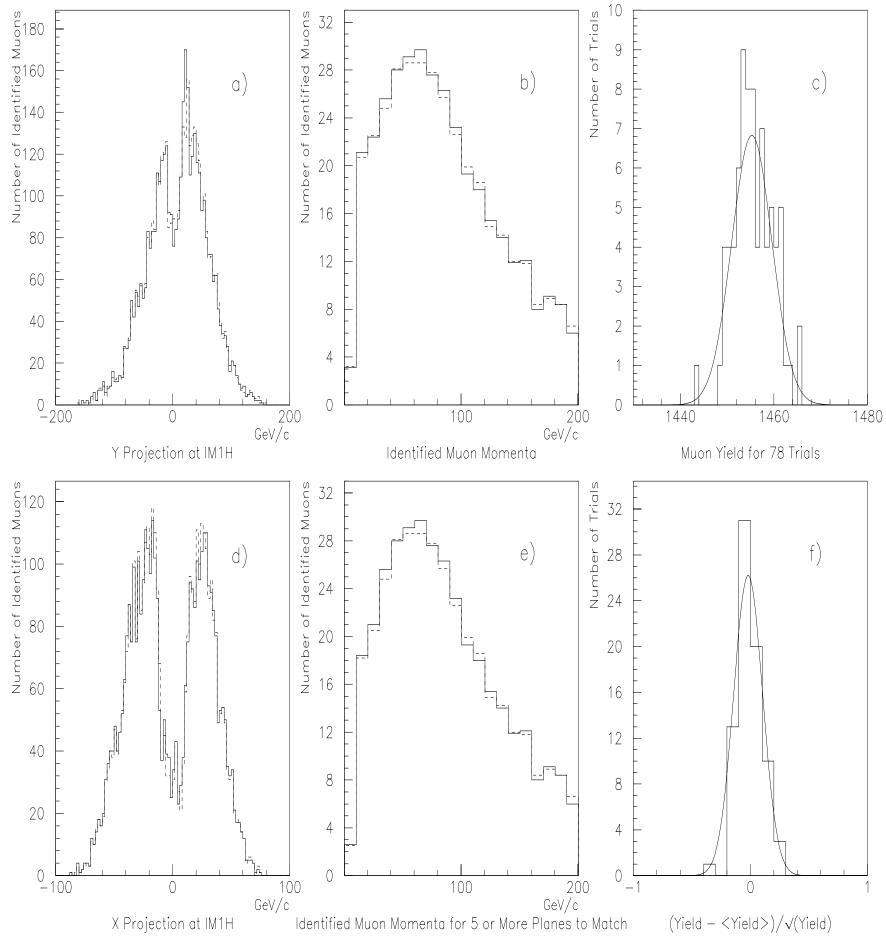

Figure 3.8.2 Plots showing the agreement between the muon identification in data and with the simulation. The X projection of identified muons is shown in a), the momentum spectra of identified muons in b), the number of muons identified using the simulation for 78 independent trials in c), the Y projection in d), the momentum spectra of identified muons for the 5 or more planes requirement in e) and f), the normalized spread of the yields for the 78 independent trials. The simulation is shown as a dotted line. Note that the gain in low momenta categories is small compared to the gain in misidentification(Figure 3.5.3). Note also that the error in the overall yield is less than $\sqrt{yield}$.

In the 1991 simulation there is an additional problem to address. The muon proportional counters had a time dependent efficiency. We looked at three runs separated throughout the 1991 running and produced 3 separate efficiency files. The loss of efficiency for each proportional tube is modeled as a linear change scaling with the amount of data triggers collected. The Monte Carlo generates a simulated amount of data triggers for each running period in the muon simulation, and the proportional tube efficiencies are calculated from the fit. The change in efficiency for a typical signal in 1991 was $\sim 14\%$. To test our model, we ran an analysis of the mode $D^0 \rightarrow K^-\mu^+\nu_\mu$ for each efficiency period and compared it to the time dependent Monte Carlo simulation. The shift in yield between the simulation and the test was roughly $0.6\sigma(1\%)$ and well within other expected shifts in the system. The systematics chapter contains a more thorough explanation of other effects. In Figure 3.8.3 we show the fit to the three separate efficiencies.

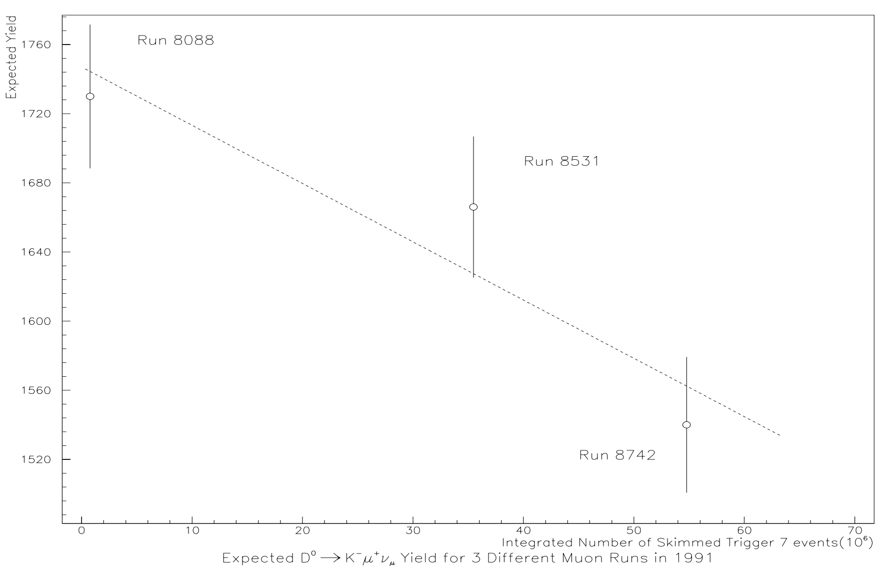

Figure 3.8.3 Plots showing the time dependent nature of the muon system. Note the excellent agreement for a linear representation of the yields. The other changes and uncertainties present in the muon system in 1991 have the effect of increasing the error bars for each point by a factor of 1.5, demonstrating that our time dependent simulation is adequate given the inherent uncertainty in the system.

3.8.9 Noise Augmented Muon Monte Carlo

As we have seen, there are additional contributions to hits in the muon system that primarily come from hadron showers. To model the effect of this noise on the muon identification and misidentification we take a tape that satisfies the skim and triggering requirements of our final signal and strip off muon hits for infusion into the Monte Carlo. These hits are added to the hits generated by the muon simulation.

If this prescription is valid, we should be able to predict the misidentification we see in the data. Figure 3.8.4 has plots showing agreement between data and the "noisy" Monte Carlo. Agreement is good. The "noisy" muons from Monte Carlo are used to get the momentum dependent probability shape used to fit the data.

Noise can affect the identification of muons as well.[21] A muon otherwise not identified as a muon because of a lost hit in a detector, can be identified as a muon if a noise hit falls within the 3σ search radius of the missed plane. Likewise, an otherwise identified muon can be lost if the number of generated hits in a plane plus the added noise in a plane cause all the hits in a plane to be dropped. In Figure 3.8.5 we see the effect of adding hits to the muon identification probability. This is an important effect in 1991 and negligible in 1990.

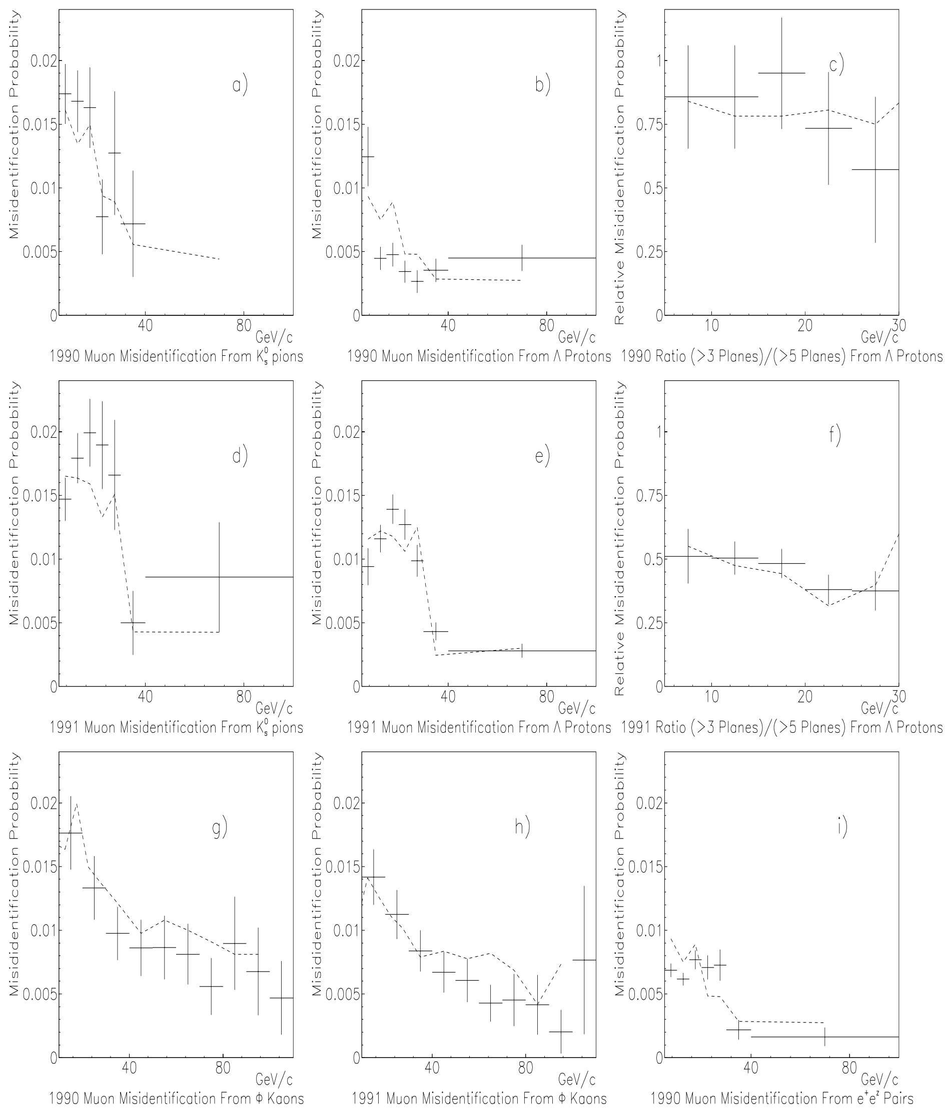

Figure 3.8.4 Plots showing the agreement in misid between data and "noisy" Monte Carlo. The Monte Carlo predictions are dotted lines.

3.8.10 Monte Carlo Reconstruction

We run the Monte Carlo raw data sample through the same reconstruction package and skimming package we used to get our sample from the real

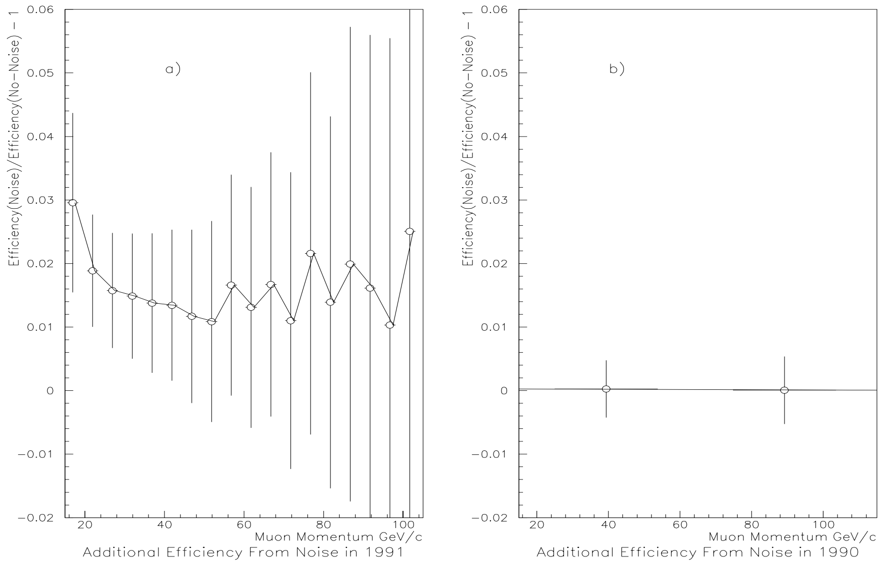

Figure 3.8.5 Plots showing noise impact on the muon id for 90 and 91. The solid line is intended to guide the eye.

data. The resultant skimmed reconstructed simulated data is analyzed in the same way as the data.

CHAPTER 4

TECHNIQUE

4.1 Introduction

In this chapter we describe the method by which information about the decay $D^0 \rightarrow K^-\mu^+\nu_\mu$ is extracted from the experimental data.

Since the D^0 is neutral and travels at most a few millimeters in an uninstrumented part of the experiment, we infer its existence via its point of origin and decay products.

When a photon fluctuates into a charm–anticharm pair in the presence of a nucleus, the accompanying fragmentation of the charm–anticharm pair results in the creation of periphery particles. Since this charm fragmentation process occurs over a very short time span, the particles, typically pions and photons, created as by–products of the fragmentation process can be used to estimate the position where the D^0 was created(see Figure 4.1.1).

Of the decay products of the D^0, the neutrino is essentially unmeasurable, so we must concentrate on the charged daughters, the kaon and the muon, to determine the location where the D^0 decayed and gain some information about the D^0 energy.

Two methods to isolate the signal are demonstrated. The first method involves measuring a D^0 that was created in the decay of another particle, the D^{*+}. This D^{*+} decays strongly, hence very quickly($10^{-23} seconds$), into a D and a pion. About half of the time, the D^{*+} decays into a D^0 and a charged pion. The information gained by utilizing the charged pion can be used to discriminate the D^0 from other signals. The second method relies on our

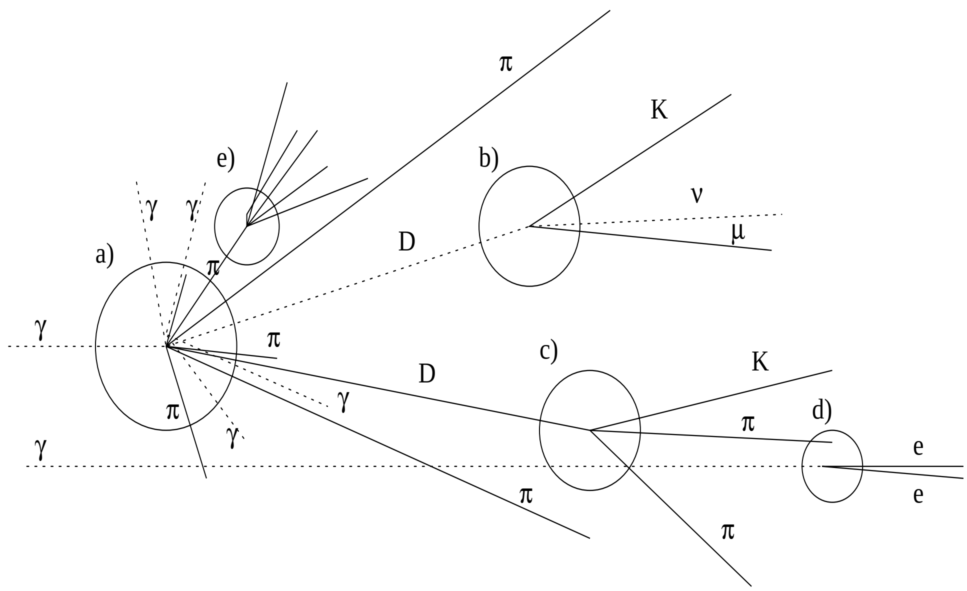

Figure 4.1.1 Topology of Typical Charm anti–Charm Event. The photon beam is incident from the left. Vertices circled are a) primary vertex, b) secondary vertex, c) secondary vertex from anti–charm, d) embedded pair and e) secondary hadronic interaction of a pion.

knowledge of other semileptonic decays and the measurement of misidentification in the E687 inner muon system to estimate the amount of $D^0 \rightarrow K^-\mu^+\nu_\mu$ present in the data.

After the signal is established, estimates of the ratio of production of $D^0 \rightarrow K^-\mu^+\nu_\mu$ to $D^0 \rightarrow K^-\pi^+$, the pole mass associated with $f_\pm(q^2)$, the strengths of $f_\pm(q^2)$, $f_\pm(0)$, and the ratio of production of $D^0 \rightarrow K^-\mu^+\nu_\mu$ to $D^0 \rightarrow K^{*-}\mu^+\nu_\mu$ will be shown.

4.2 The $K^-\mu^+$ Signal from a D^{*+}

4.2.1 $K^-\mu^+$ Candidate Selection

We chose events that were in the Global Vertex skim of the 1990 and 1991 data samples. This skim was favored over the more specific semileptonic skims because it represented the least biased sub–sample of reconstructed events that contained both $K^-\mu^+$ and $K^-\pi^+$. The amount of data we lose by requiring this skim is on the order of 10%.

The Global Vertex skim has a base requirement of at least 3 microstrip tracks that are inconsistent with being e^+e^- production. The skim uses linked microstrip tracks and tests the hypothesis that they come from a common point of origin. If the hypothesis succeeds, i.e. the fitter returns a confidence level of 1% or greater, the tracks are retained. All such pairs of tracks in an event are found. If any two vertices are separated by more than 4.5 standard deviations in z, the event is retained.

In addition to the Global Vertex skim, we require that there be at least 4 microstrip tracks so that we can form both a primary and a secondary vertex. We also require that there be at least 4 tracks in the PWC system and that the main data trigger, trigger 7, is present.

The microstrip tracks are checked to see if they linked to a PWC track. Doubly linked tracks, which have the potential to be from e^+e^- production are rejected in the later analysis, but we retain them in the search for primary vertices.

If the link is successful, there is a requirement that the kaon candidate track have a Čerenkov pattern consistent with being either a kaon or a kaon/proton. The gains to be made by allowing other Čerenkov categories are low. Potentially, the largest gain can be realized if we add the kaons which are consistent with either a kaon or a pion. The gain in signal is expected to be $\sim 10\%$, but the problems with allowing pions into the signal are large. We reject the kaon/pion consistent tracks because of the potential for backgrounds from $D^0 \rightarrow \pi^-\mu^+\nu_\mu(\sim 10\% D^0 \rightarrow K^-\mu^+\nu_\mu), D^0 \rightarrow K^{*-}(K^{*-} \rightarrow K^0\pi^-)\mu^+\nu_\mu(\sim 10\% D^0 \rightarrow K^-\mu^+\nu_\mu)$ and especially $D^0 \rightarrow ((K^- \ or \ \pi^-)X)$. It must be remembered that the mode specific backgrounds above are *in addition* to those already present in the kaon rich sample, and the muon misidentified signal in X is now Cabibbo allowed for either the kaon or the pion.

The muon candidate track has the same linking requirement as the kaon, but it is required to not be a kaon consistent particle. We require this candidate track to be identified as a muon by the inner muon system. In 1991, the usual muon identification requirement was tightened to eliminate categories of muons identified with momentum below 30 GeV/c using only the first bank of the inner muon system. This requirement halves the noise from muon misidentification below 30 GeV/c and retains $\sim 90\%$ of the signal.

A 10 GeV/c momentum cut is applied to the muon candidate in 1990 and a 15 GeV/c momentum cut is applied to the muon candidate in 1991. This cut is used to reduce contamination from misidentification, and, in 1991 it is increased to 15 GeV/c as the added noise in the muon system increases both the misidentification probability and uncertainty in the identification probability.

To infer the presence of a vertex, we take the candidate microstrip tracks and form a confidence level that the distance of closest approach of these two tracks is consistent with a point of common origin. The confidence level is required to be better than 1%.

We form a mass using the candidates tracks four momenta and require this mass to be between 0.95 GeV/c^2 and 1.855 GeV/c^2. This cut removes most of the $K^-\pi^+$ contamination, reduces contamination from any higher multiplicity semileptonic modes and reduces backgrounds from muon misidentification. Figure 4.2.1 is the resultant $K^-\mu^+$ mass after all cuts are applied.

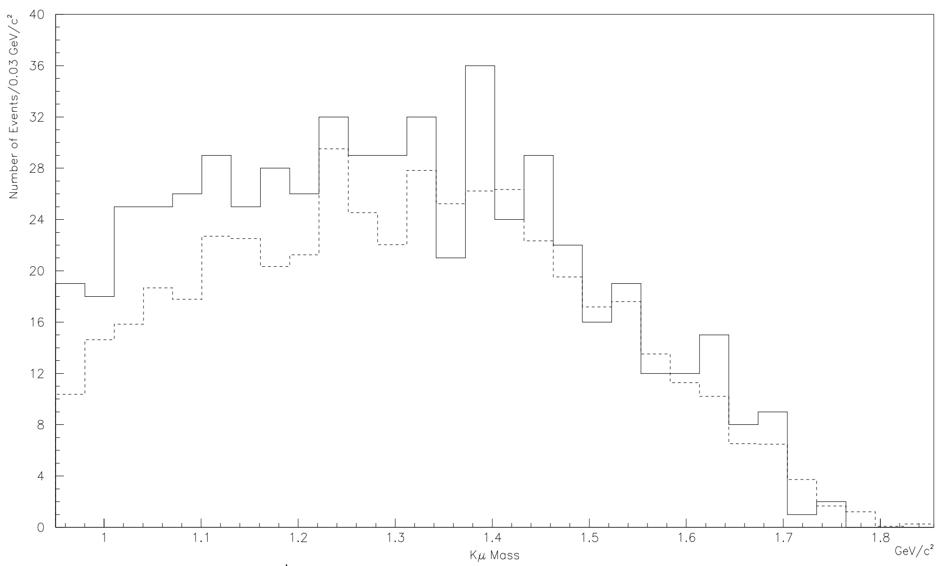

Figure 4.2.1 The $K^-\mu^+$ Mass after all selection criteria. The expected shape from the Monte Carlo for $D^0 \to K^-\mu^+\nu_\mu$ only is overlaid as a dashed line. Note that expected backgrounds from misidentification and $D^0 \to K^{*-}\mu^+\nu_\mu$ are not included in this the Monte Carlo plot. This plot gives us a feel for the amount of background present in the signal.

4.2.2 Primary Vertex Selection

In order to look at the separation between production and decay points, we must select a location for a primary, or production, vertex.

To find a primary vertex, we exclude our previously found $K^-\mu^+$ candidate and use the rest of the microstrip tracks to form candidate primary vertices. Specifically, a track is chosen as a cluster seed, other tracks are added to the seed as long as the confidence level for the vertex hypothesis remains above the cutoff(typically 1%). Tracks not in this vertex cluster are used as new seeds to find additional clusters. For each new cluster, previously used tracks can be again used in the new cluster. We choose one of these clusters by taking the highest multiplicity vertex found in the production target. Ties are resolved by choosing the primary vertex with the best l/σ from the $K^-\mu^+$ candidate vertex. If no primary can be found in the production target or if there is no primary candidate with l/σ above 3.0, we try to find another $K^-\mu^+$ candidate vertex and repeat the primary search. Other methods of finding a primary vertex are discussed in the section on systematic errors.

If there are unused tracks left after finding the $K^-\mu^+$ and primary vertices, we check to see if any of these left over tracks are consistent with forming a vertex with the $K^-\mu^+$ pair. In this way, we can reduce potential backgrounds from higher multiplicity states. We require the confidence level that any left over tracks are consistent with the $K^-\mu^+$ vertex to be $< 1\%$.

4.2.3 D^0 Momentum Reconstruction

There is enough information now to attempt to reconstruct two momentum solutions for a D^0 candidate from the $K^-\mu^+$ candidate and primary vertex candidate information. Since we can only hypothesize the neutrino, there are two solutions for the D^0 momentum.

To solve the basic equation:

$$M_\nu^2 = (E_{D^0} + E_K + E_\mu)^2 - (\overline{P}_{D^0} + \overline{P}_K + \overline{P}_\mu)^2 \tag{4.2.1}$$

We follow the procedure[22] of E691 and boost to a frame where

$$\overline{P}(k\mu) \cdot \hat{l} = 0(\hat{l}\ is\ the\ D^0\ decay\ direction). \tag{4.2.2}$$

We can solve for the neutrino energy in this frame which gives us the neutrino, hence the D^0, $\pm$ momentum along the D^0 decay direction. Next, we boost these solutions to the lab frame.

Rather than just solve equation (4.2.1) directly, this formulation gives us a calculation of some physical quantities associated with the decay. We require the neutrino energy in the boosted frame be greater than zero. Also, due to resolution effects, the squared neutrino momentum along the D^0 is not always a positive quantity. We still accept these events with negative squared neutrino momentum along the D^0 decay direction, but we force the neutrino momentum to be zero if $P^2_{\nu\ along\ D^0} > -1.4$ and discard the solution if $P^2_{\nu\ along\ D^0} < -1.4$. This procedure, which prevents the loss of $\sim 1/3$ of the signal, does not adversely affect our measurements.

In Figure 4.2.2 we show some of the physical quantities associated with the D^0 momenta reconstruction.

4.2.4 D^{*+} Reconstruction

Now that there are one or two candidate D^0's, we can choose another linked track to form the D^{*+} mass by assuming the D^0 mass.

We choose tracks that have a Čerenkov identification consistent with a pion and that come from the primary vertex(the D^{*+} decays quickly). The solutions returned from the D^0 momenta determination are combined with this pion to determine the mass of the D^{*+}.

The mass difference between the D^{*+} and the D^0 is about 145.5 MeV/c^2 and the pion mass is 139.57 MeV/c^2. To choose the correct D^0 candidate, we sort through all possible solutions using all the tracks in the event and retain the solution which gives us the lowest $D^{*+} - D^0$ mass difference.

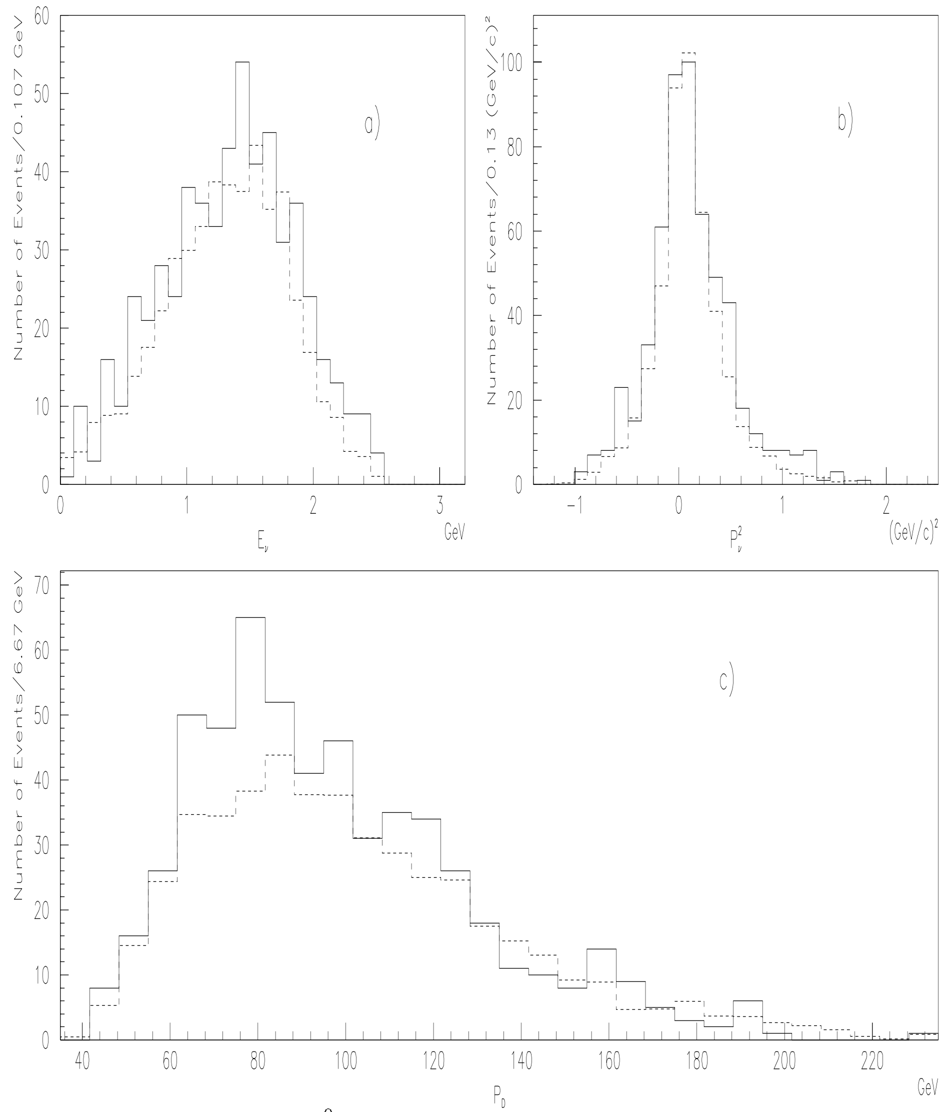

Figure 4.2.2 Plots of D^0 momenta reconstruction parameters: a)E_ν, b) $P_{\nu\ along\ l}^2$ and c) Low D^0 lab momentum solution. The expected shapes from the Monte Carlo for $D^0 \to K^-\mu^+\nu_\mu$ decays are overlaid as dotted lines.

This technique can have a bias if there is a large amount of background under the signal which cannot be modelled or predicted with other data or Monte Carlo. To that effect, we accept both the charge correct pion $Q(\pi) =$

$Q(\mu)$ and the charge opposite pion $Q(\pi) \neq Q(\mu)$ as a check on backgrounds. No large buildup at low D^{*+} mass is seen(Figure 4.2.3).

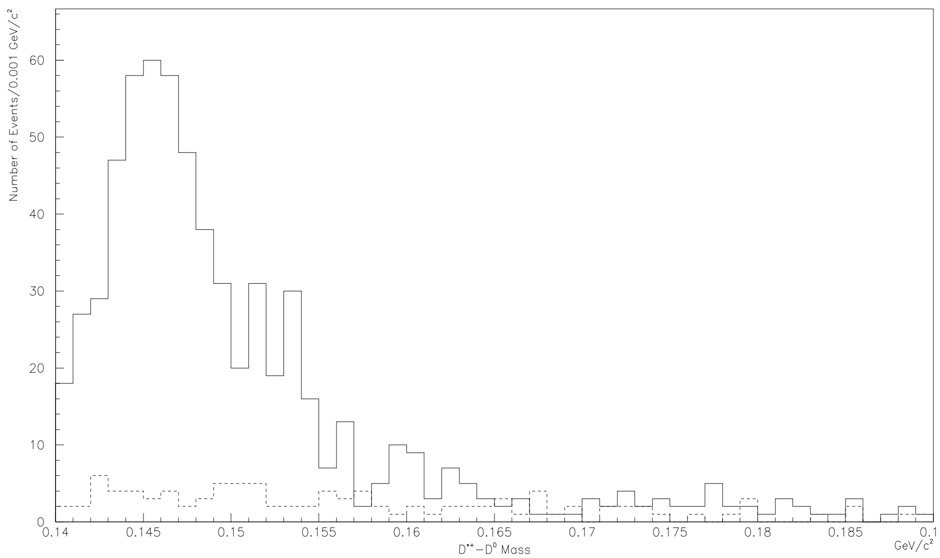

Figure 4.2.3 The $D^{*+} - D^0$ Mass difference for the tagged analysis. The events with $Q(\pi) \neq Q(\mu)$ are overlaid as a dashed line to show the level of non–D^{*+} background in the signal.

Allowing both charge solutions can create problems too. The momentum of an anti–charm daughter, presumably one from a D^{*-}, has a correlation to the decay of interest because the fragmentation of the charm is correlated to the fragmentation of the anti–charm. The correlation is not perfect and smears out the anti–charm's pion. Sometimes, the anti–charm's pion will produce a D^{*+} mass solution lower than that for the correct charm's pion. The effect is small when we consider the likelihood that both charm and anti–charm solutions are present in the same event($\sim 1\%$).

4.2.5 Kinematic Variables of Interest

In the first chapter, we observed that the information useful in determining the pole mass behavior is largely contained in the q^2 or E_{kaon} dependence. We reconstruct the q^2 distribution using the D^0 momentum solution chosen above and the information we have for the kaon track.

The traditional way to measure the pole mass dependence is to find the yield of events that decay via $D^{*+} \to (D^0 \to K^-\mu^+\nu_\mu)\pi^+$ utilizing the D^{*+} mass peak and the wrong sign events as a background shape. Once the yield is known, the q^2 distribution is fit to determine the pole mass. The main difficulty in this type of analysis is assessing the amount of non D^{*+} decayed $D^0 \to K^-\mu^+\nu_\mu$ that gets into the q^2 distribution. We avoid this problem by extracting both the yield of $D^0 \to K^-\mu^+\nu_\mu$ events and the pole mass from the q^2 distribution. This technique allows us to use the D^{*+} mass as information to constrain the event as well.

We test the hypothesis that the event is really $D^{*+} \to (D^0 \to K^-\mu^+\nu_\mu)\pi^+$. We use the D^{*+} pion along with the $K^-\mu^+$ and decay direction to find a single solution for the D^0 momentum.

The event is boosted to the $K^-\mu^+$ center of mass frame. In this frame the D^0 and the neutrino sweep out a cone of possible solutions around the D^{*+} pion. This happens because we know:

$$E_\nu = \frac{M_{D^0}^2 - M_{K\mu}^2}{2(E_K + E_\mu)} \tag{4.2.3}$$

$$\bar{P}_\pi \cdot \bar{P}_D = (M_D^2 + M_\pi^2 + 2E_\pi(E_K + E_\mu) + 2E_\pi E_\nu - M_{D^*}^2)/2. \tag{4.2.4}$$

So we require:

$$|P_\pi||P_D| \geq \bar{P}_\pi \cdot \bar{P}_D \tag{4.2.5}$$

to be consistent with the hypothesis that $D^{*+} \to (D^0 \to K^-\mu^+\nu_\mu)\pi^+$ is what we reconstructed. Figure 4.2.4 is a visualization of the kinematical situation.

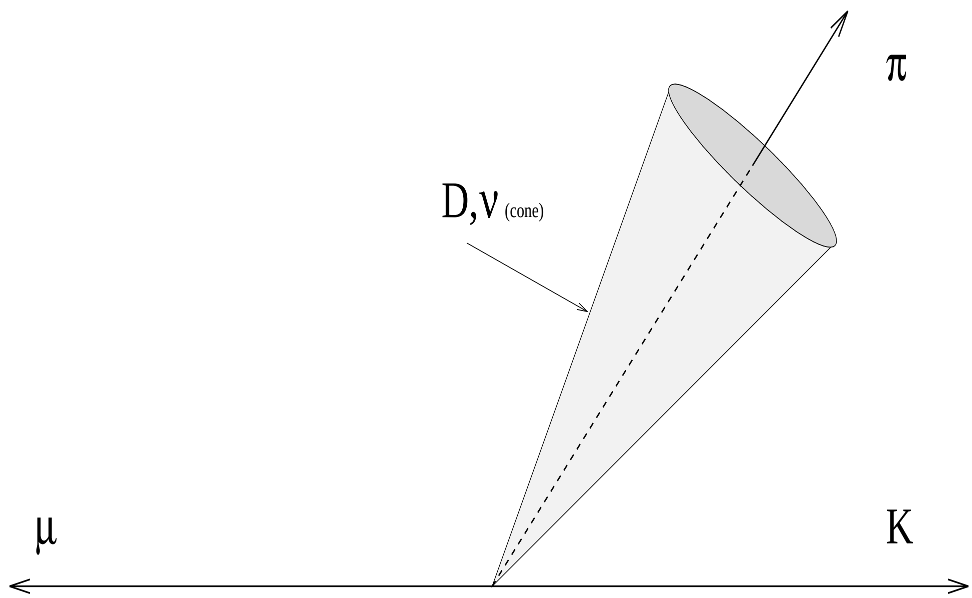

Figure 4.2.4 Plot showing the kinematic situation in the $K^-\mu^+$ center of mass system.

In practice we check 1000 solutions on the cone(one every 0.00628 radians) and choose the solution that is closest to the D^0 decay direction in the lab frame. We reform q^2 and refit the event. The added benefit from this procedure is that all measured quantities are within their physical boundaries and no correction for unphysical events is required.

4.3 Fitting the $K^{-}\mu^{+}$ signal

We fit the data by building up a simulated data histogram in q^2 using Monte Carlo and data that represent backgrounds. The pole mass and the yield are fit at the same time by utilizing the known generated and reconstructed distributions of the Monte Carlo signal for $D^0 \rightarrow K^{-}\mu^{+}\nu_{\mu}$.

4.3.1 Generating Shapes for the Fit

There are several ways to generate a Monte Carlo distribution. The fit technique we use utilizes two methods simultaneously.

We generate a matrix element magnitude(probability), in our case $f_{+}^{2}(q^2, m_{pole_0})M_0^2(q^2, E_{\mu})$, via the decay products produced by our phase space generator utilizing a rejection method. That is, we generate a decay and calculate the magnitude of the matrix element. If this matrix element value is greater than the maximum allowable matrix element magnitude multiplied by a random number distributed evenly between 0 and 1, we keep the generated event.

$$Generated\ Magnitude > Random\ Number(Maximum\ Magnitude) \quad (4.3.1)$$

Another way the event could have been generated is to keep track of the possibility of the event occurring, and reweight the event later based on this probability.

$$Probability\ of\ Event\ Occurring = \frac{Generated}{Maximum} \quad (4.3.2)$$

Where we must make sure that

$$Maximum = \int_{phase\ space} f_{+}^{2} M_0^2, \quad (4.3.3)$$

so the number of events reconstructed is correct.

In any case, the probability that we retain an event is related to the momentum and direction of the kaon and the muon in the D^0 center of mass and the chosen pole mass.

4.3.2 Modifying Shapes for the Fit

In essence, the tracing portion of the Monte Carlo gives us a discrete transform(T) from generated space to reconstructed space. We can modify aspects of the generated decay distribution such as the chosen pole mass or the matrix element, and see the effects readily in reconstructed space. In this way we avoid generating a separate Monte Carlo sample for each choice of the pole mass. The drawback to this method is that one needs either a large Monte Carlo event sample to map out the transform properly or one must be willing to give up resolution by utilizing larger bins in the fit histogram.

If an event in reconstructed space is represented by $D(q^2, E_\mu)_i$, in generated space by $G(q_0^2, E_{\mu 0})_i$, the transform between generated and reconstructed space by $T(< q_0^2, E_{\mu 0} >, < q^2, E_\mu >)_i$ and the weight for each event by $W(q_0^2, E_{\mu 0}, m_{pole})_i$, we can describe the distribution of a reconstructed event for any m_{pole} with:

$$D(q^2, E_\mu)_i = G(q_0^2, E_{\mu 0})_i T(< q_0^2, E_{\mu 0} >, < q^2, E_\mu >)_i W(q_0^2, E_{\mu 0}, m_{pole})_i. \tag{4.3.4}$$

We can avoid calculating the transform by noting that the discrete nature of the transform will give identical results if the weight is forced to be 1. Thus, the only variant on an event by event basis is the weight of the event.

$$D(q^2, E_\mu)_i \mid_{m'_{pole}} = D(q^2, E_\mu)_i \mid_{m_{pole}} \times \left(\frac{G(q_0^2, E_{\mu 0})_i T(< q_0^2, E_{\mu 0} >, < q^2, E_\mu >)_i W(q_0^2, E_{\mu 0}, m'_{pole})_i}{G(q_0^2, E_{\mu 0})_i T(< q_0^2, E_{\mu 0} >, < q^2, E_\mu >)_i W(q_0^2, E_{\mu 0}, m_{pole})_i} \right). \tag{4.3.5}$$

and since q^2,E_μ,q_0^2 and $E_{\mu 0}$ are the same,

$$D(q^2, E_\mu)_i \mid_{m'_{pole}} = D(q^2, E_\mu)_i \mid_{m_{pole}} \frac{W(q_0^2, E_{\mu 0}, m'_{pole})_i}{W(q_0^2, E_{\mu 0}, m_{pole})_i} \tag{4.3.6}$$

where

$$W(q_0^2, E_{\mu 0}, m_{pole}) = \frac{f_+^2(q_0^2, m_{pole}) M_0^2(q_0^2, E_{\mu 0})}{\sum_{i=1}^{\#\ Generated} f_+^2(q_i^2, m_{pole}) M_0^2(q_i^2, E_{\mu i}) / \#\ Generated}. \tag{4.3.7}$$

4.3.3 Forming the Likelihood

The method we use for the present measurement utilizes a binned maximum likelihood technique. This technique has been shown to be a robust estimator for other E687 analyses. We can perform many fits in a reasonable amount of time, and we need not choose a function to represent any particular shape used in the fit.

Essentially, the likelihood is a probability. How we choose the form of the probability is important. For a small sample chosen at random from a large one, we should use Poisson statistics to motivate our choice. Since a χ^2 fit will underestimate the yield in a signal obeying Poisson statistics(typically by the value of χ^2), we could choose the popular χ^2 or $\sigma = \sqrt{n}$ approach only if we had well populated bins and a lot of signal.

The idea is to maximize the probability. In practice, it is easier to minimize $-\log L$. As this is a sum instead of a product, we avoid dealing with very large numbers on the computer. The form of the likelihood for Poisson statistics will be:

$$\mathcal{L} = \prod_{bins_i} \frac{n_i^{s_i} e^{-n_i}}{s_i!}, \tag{4.3.8}$$

where

$$s_i = \text{number of events in } bin_i$$

$$n_i = \text{number of event in fit histogram } bin_i.$$

The likelihood estimator allows us to compare the data histogram and the fit histogram. The fit histogram is composed of everything we think is in the data histogram with a guess as to what is left over. The actual fit process adjusts the magnitude of each contribution to the fit histogram to make the best possible one. The fitting routine also returns an estimate of how well it thinks the fit histogram represents the data.

4.3.4 Making the Fit Histogram

We have to decide what signals to place in the fit histogram. Hopefully our cuts have done a reasonable job of making the signal we are interested in the majority contribution of our data. We are left with trying to predict the rest of the data signal(background). Our Monte Carlo has the capacity to simulate $D\overline{D}$ production where each meson is then decayed according to the Particle Data Group branching ratios. If the tracing routine(ROGUE) has done a reasonable job, we should be able to identify the larger contributions to the background. In principle, one could run enough Monte Carlo in this way to analyze the signal, but the amount of Monte Carlo needed makes this a very

Table 4.3.1 $D^0 \to K^-\mu^+\nu_\mu$ Signal Contributors

Mode	$\sim$ % Amount of total signal
$D^0 \to K^-\mu^+\nu_\mu$	86
$D^0 \to K^{*-}\mu^+\nu_\mu$	11
$D^+ \to K^{*0}\mu^+\nu_\mu$	1
$D_s^+ \to \phi\mu^+\nu_\mu$	< 1
$D \to K^-X$ MISID	2
$D \to \pi^-X$ MISID	< 1

time consuming process. Looking at modes that populate the $D^0 \to K^-\mu^+\nu_\mu$ analysis in Table 4.3.1, we can identify several important modes.

I choose to leave off all the modes that contribute to $D \to K^-X$ since they are myriad and each has its own production dynamics, matrix elements, etc.

Of the contributors to the signal, the relative branching ratio to $D^0 \to K^-l^+\nu_l$ has been measured for $D^0 \to K^{*-}l^+\nu_l$[23], $D^+ \to K^{*0}l^+\nu_l$[24] and can be estimated for $D_s^+ \to \phi l^+\nu_l$.[24,25] The $D^+ \to K^{*0}l^+\nu_l$ measurements are accomplished by assuming the isospin argument

$$, (D^0 \to K^{*-}\mu^+\nu_\mu) = , (D^+ \to K^{*0}\mu^+\nu_\mu), \tag{4.3.9}$$

and by using the branching ratios $D^0 \to K^-\pi^+$ and $D^+ \to K^-\pi^+\pi^+$, the relative production of D^0 vs. D^+ and the lifetimes of the D^0 and D^+. The

$D_s^+ \to \phi\mu^+\nu_\mu$ production is estimated using the relation

$$, (D^+ \to K^{*0}\mu^+\nu_\mu) = (1.11 \pm 0.13)^{[25]}, (D_s^+ \to \phi\mu^+\nu_\mu), \tag{4.3.10}$$

our yields and efficiency of $(D^+ \to K^{*0}\mu^+\nu_\mu)$[26,27] and $(D_s^+ \to \phi\mu^+\nu_\mu)$,[27] the D^+[28] lifetime and the D_s^+[29] lifetime. Therefore, these modes actually add information about $D^0 \to K^-\mu^+\nu_\mu$ to the fit histogram since we can estimate contributions via

$$\begin{aligned} &Semileptonic\ Contribution = \#(D^0 \to K^-\mu^+\nu_\mu)\times \\ &\left[1+\left(\tfrac{\# D^0 \to K^{*-}\mu^+\nu_\mu}{\# D^0 \to K^-\mu^+\nu_\mu}\right)+\left(\tfrac{\# D^+ \to K^{*0}\mu^+\nu_\mu}{\# D^0 \to K^-\mu^+\nu_\mu}\right)+\left(\tfrac{\# D_s^+ \to \phi\mu^+\nu_\mu}{\# D^0 \to K^-\mu^+\nu_\mu}\right)\right] \end{aligned} \tag{4.3.11}$$

The estimate of the background $D \to K^-X$ via muon misidentification is discussed in the reconstruction and systematics chapters. The estimate of the remaining background is made using wrong sign data from the misidentified(IDMU=0) sample.

The fit histogram can now be constructed using the separate components. We form the number of events, n_i, in the fit histogram as

$$\begin{aligned} n_i =&Y \left(S_{1i} + \frac{\epsilon_2}{\epsilon_1}(BRVP)S_{2i} + \frac{\epsilon_3}{\epsilon_1}(BRVP)\frac{P_2}{P_1}\frac{T_2}{T_1}S_{3i} + \right. \\ &\left. \frac{\epsilon_4}{\epsilon_1}(BRVP)\frac{P_3}{P_2}\frac{P_2}{P_1}\frac{T_2}{T_1}S_{4i}\right) + M\ S_{Mi} + X\ S_{Xi} \end{aligned} \tag{4.3.12}$$

where

Y= $D^0 \to K^-\mu^+\nu_\mu$ yield

$\epsilon_1 = \frac{D^0 \to K^-\mu^+\nu_\mu\ accepted}{D^0 \to K^-\mu^+\nu_\mu\ generated}$

$\epsilon_2 = \frac{D^0 \to K^{*-}\mu^+\nu_\mu\ accepted}{D^0 \to K^{*-}\mu^+\nu_\mu\ generated}$

$\epsilon_3 = \frac{D^+ \to K^{*0}\mu^+\nu_\mu \ accepted}{D^+ \to K^{*0}\mu^+\nu_\mu \ generated}$

$\epsilon_4 = \frac{D_s^+ \to \phi\mu^+\nu_\mu \ accepted}{D_s^+ \to \phi\mu^+\nu_\mu \ generated}$

$BRVP = \frac{BR(D^0 \to K^{*-}\mu^+\nu_\mu)}{BR(D^0 \to K^-\mu^+\nu_\mu)}$

$\frac{P_2}{P_1}$ = ratio of production $\frac{D^+}{D^0}$ [30]

$\frac{P_3}{P_2}$ = ratio of production $\frac{(D_s^+ \to \phi\mu^+\nu_\mu)}{(D^+ \to K^{*0}\mu^+\nu_\mu)}$

$\frac{T_2}{T_1}$ = ratio of lifetimes $\frac{\tau_{D^+}}{\tau_{D^0}}$

M = number of events estimated to come from muon misidentification

X = number of background events

S_{1i} = fraction of $D^0 \to K^-\mu^+\nu_\mu$ in bin_i

S_{2i} = fraction of $D^0 \to K^{*-}\mu^+\nu_\mu$ in bin_i

S_{3i} = fraction of $D^0 \to K^{*0}\mu^+\nu_\mu$ in bin_i

S_{4i} = fraction of $D^0 \to \phi\mu^+\nu_\mu$ in bin_i

S_{Mi} = fraction of muon misidentification signal in bin_i

S_{Xi} = fraction of background in bin_i

The values ϵ_1 and the S_i's warrant some further explanation. ϵ_1 is modified for each m_{pole} or change in matrix element as described in the section "Modifying Shapes for the Fit." Briefly, the whole $D^0 \to K^-\mu^+\nu_\mu$ sample is reweighted event–by–event and loaded into a new histogram. The new efficiency ϵ_1 is calculated and the new histogram is normalized for a new S_1. Each S_i is taken from a normalized histogram of the signal in question. I.e. for any S_i

$$\sum_{i=1}^{\#\ of\ bins} S_i = 1. \tag{4.3.13}$$

Due to the drastic change in the muon system in 1991, we analyzed the 1990 and 1991 data separately. Each S, M, Y, X and M_{pole} has a representation for both 1990 and 1991. The parameters varied in the fit are Y_{90}, Y_{91}, X_{90}, X_{91} , m_{pole90} and m_{pole91}. The likelihood becomes

$$\mathcal{L} = \prod_{bins_{90i}} \frac{n_{90i}^{s_{90i}} e^{-n_{90i}}}{s_{90i}!} \prod_{bins_{91i}} \frac{n_{91i}^{s_{91i}} e^{-n_{91i}}}{s_{91i}!} \tag{4.3.14}$$

where

$$\begin{aligned} s_{90i} &= \text{number of events in } bin_i \text{ in 1990} \\ n_{90i} &= \text{number of events in fit histogram } bin_i \text{ in 1990} \\ s_{91i} &= \text{number of events in } bin_i \text{ in 1991} \\ n_{91i} &= \text{number of events in fit histogram } bin_i \text{ in 1991.} \end{aligned}$$

4.3.5 Results of the Fit

To minimize the negative log likelihood, we use the MINUIT[31] package from CERN. The fit returns 194 ± 16 events in 1990, 232 ± 22 events in 1991, a pole mass of $2.09^{+0.66}_{-0.29}$ in 1990 and a pole mass of $1.97^{+0.43}_{-0.22}$ in 1991.(In subsequent measurements of the pole mass using the D^* sample the 1990 and 1991 pole mass variabless are combined in the fit routine.) Figure 4.3.1 is the q^2 distribution with fit overlaid. The agreement appears quite good. A study of the reliability of the fitter and the systematic error associated with this measurement can be found in the chapter on systematics.

4.3.6 Fitting for f_-

We can release our assumption that $|f_-(0)/f_+(0)| = 0$ in the fit and try to estimate this quantity. We use the same procedure outlined above to find a value for the ratio $|f_-(0)/f_+(0)|$. We fix $m_{pole} = 2.0 \pm 0.22$ and vary $|f_-(0)/f_+(0)|$ only so that we need not perform thousands of normalization integrals. Our cuts used in the analysis above lower our sensitivity

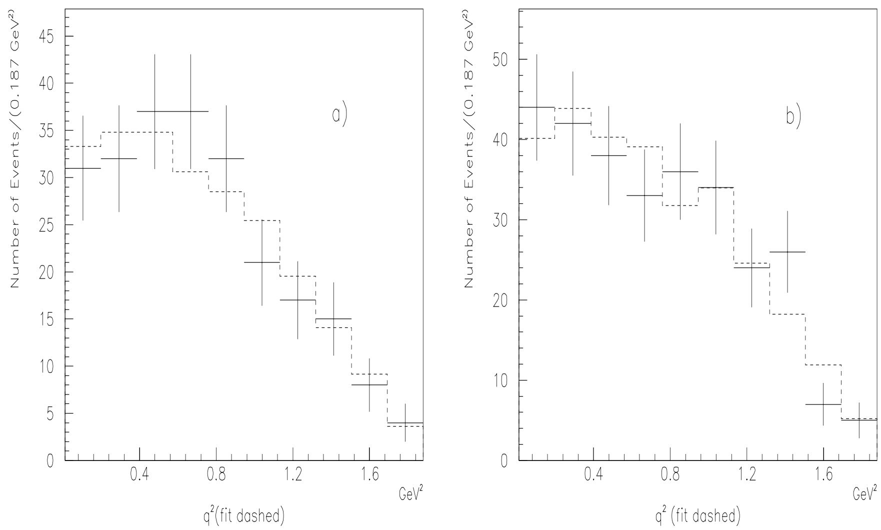

Figure 4.3.1 The q^2 distribution with fit overlaid as a dashed line for: a) 1990 data and b) 1991 data.

to $|f_-(0)/f_+(0)|$ by a factor of 2. Since the quality of the tag analysis signal is high, we relax our cut on the $K^-\mu^+$ mass to increase our sensitivity to $|f_-(0)/f_+(0)|$. We also expand the fit to include the information from the muon energy in the D^0 center of mass. We find that $|f_-(0)/f_+(0)| = 2.2 \pm 2.0$. A study of the reliability of the result can be found in the chapter on systematics.

4.4 The $K^-\pi^+$ Signal From a D^{*+}

4.4.1 $K^-\mu^+$ Candidate Selection

We keep the analysis for the $K^-\pi^+$ signal as close as possible to the $K^-\mu^+$ signal. The vertexing, Čerenkov and acceptance cuts are the same as the tag sample. The mass cut on $K^-\pi^+$ is from 1.78 GeV/c^2 to 1.95 GeV/c^2, and since we already know the D^0 energy, no kinematic ambiguity exists. We form the D^{*+} simply by finding the $K^-\pi^+\pi^+$ mass and subtracting off the

$K^-\pi^+$ mass. The fit is performed on the $K^-\pi^+$ mass spectra to avoid the problems described in estimating the background in the $D^{*+} - D^0$ mass peak for $K^-\mu^+$. We just try to find the amount of $D^0 \rightarrow K^-\pi^+$ for a $D^{*+} - D^0$ mass difference less than 0.150 GeV/c^2. The quality of the signal is high as shown in Figure 4.4.1.

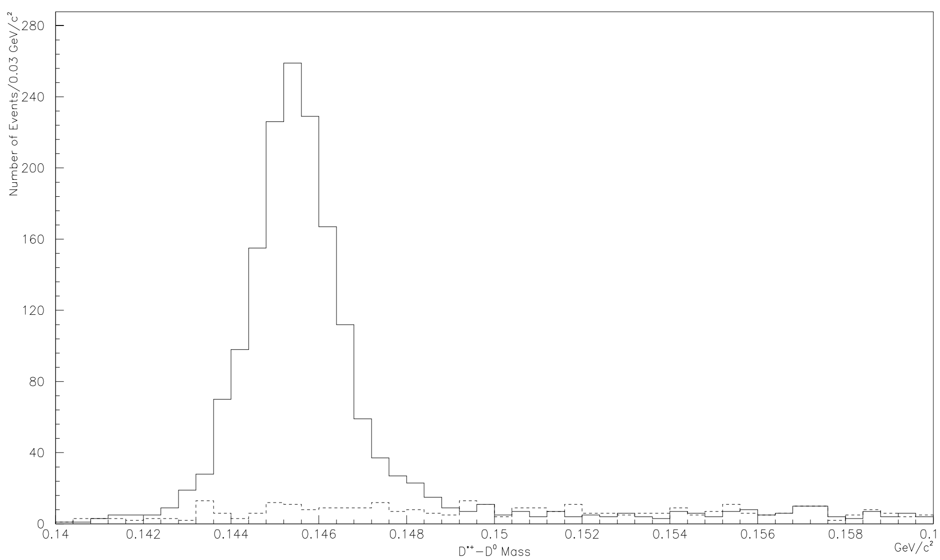

Figure 4.4.1 The $D^{*+} - D^0$ mass difference for the $D^0 \rightarrow K^-\pi^+$ analysis. The events with $Q(\pi) \neq Q(\mu)$ are overlaid as a dashed line to show the level of non–D^{*+} background in the signal. If the $Q(\pi) = Q(\mu)$ distribution is fit to a Gaussian and a 3rd degree polynomial we find 1432 ± 40 events with a mass difference of 0.145437 ± 0.000031 GeV/c^2.

4.5 Fitting the $K^-\pi^+$ signal

We fit the data by building up a simulated data histogram in $K^-\pi^+$ mass using Monte Carlo and a function that represents backgrounds.

4.5.1 Making the Fit Histogram

The fit histogram is different from the $K^-\mu^+$ analysis because we use a functional form for the backgrounds we do not model. The only known background accounted for is $D^0 \rightarrow K^+K^-$, and its representation is functionalized as well. Our representation or the number of events in a $K^-\pi^+$ mass bin_i is:

$$n_i = YS_{1i} + AS_{2i} + BS_{3i} + CS_{4i} \tag{4.5.1}$$

where

$Y = D^0 \rightarrow K^-\pi^+$ yield

A=Amount of constant background present

B=Amount of background that varies linearly in $K^-\pi^+$ mass

C=Amount of K^-K^+ background that varies as

$exp(-.5 * ((M(K^-\pi^+) - 1.775)/.0234)^2$ in $K^-\pi^+$ mass

S_{1i} = fraction of $D^0 \rightarrow K^-\pi^+$ in bin_i

S_{2i} = fraction of A in bin_i

S_{3i} = fraction of B in bin_i

S_{4i} = fraction of C in bin_i

In practice, the fit converges more rapidly when we eliminate the $D^0 \rightarrow K^+K^-$ region($M(K^-\pi^+) < 1.82\ GeV/c^2$) from fit consideration. The resultant increase in the error of the yield is small and the fit no longer depends on the estimate of $D^0 \rightarrow K^+K^-$, so we do not include it in the fit.

4.5.2 Results of the Fit

To minimize the negative log likelihood, we again use the MINUIT[31] package from CERN. The fit returns 446 ± 21 events in 1990 and 971 ± 34 events in 1991. The agreement between the fit and the data is excellent and is shown in Figure 4.5.1.

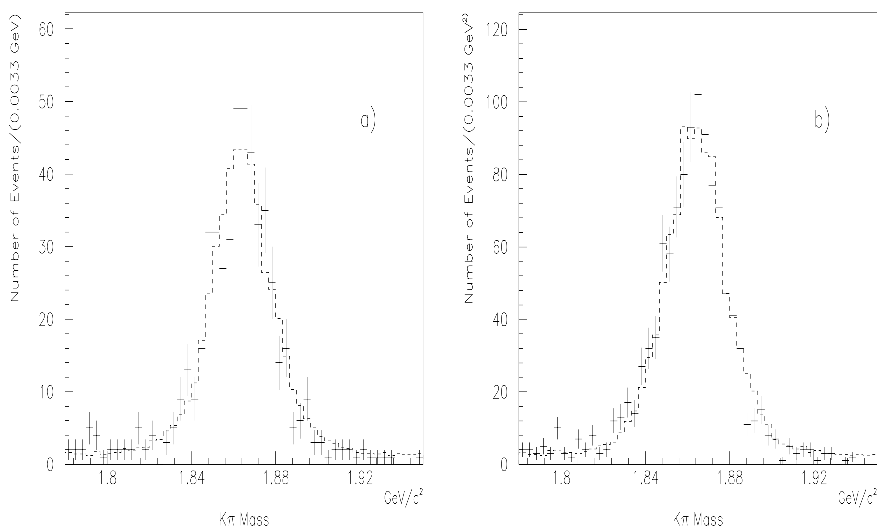

Figure 4.5.1 The $K^-\pi^+$ mass signal from a) 1990 data and b) 1991 data. The fit histogram is overlaid as a dotted line.

4.6 The $K^-\mu^+$ Signal

In this section we describe a method to isolate the $D^0 \to K^-\mu^+\nu_\mu$ signal without the benefit of a D^{*+}. The procedures used to find and analyze the signal are similar to the D^{*+} technique, but we make harder requirements on the $K^-\mu^+$ vertex and the muon momentum to distinguish signal from background. The D^0 momenta reconstruction differs slightly, and we use a different source of background to represent what is left over after we predict what is in the signal.

We choose to fit a two dimensional histogram for this $K^-\mu^+$ signal. Backgrounds are higher in this method, and utilizing two kinematical variables helps us discriminate between the different contributions to the overall signal.

The primary motivation for analyzing the signal without a D^{*+} is to increase the number of events we analyze. The goal is to get a better measurement using this method than is possible using the D^{*+} technique.

4.6.1 $K^-\mu^+$ Candidate Selection Differences

The kaon selection is identical to the D^{*+} case. A large amount of background from muon misidentification appears in the $K^-\mu^+$ signal at low muon momentum. We make cuts that enhance the high end of the muon momentum spectrum. The minimum allowed muon momentum is 15 GeV. We require that the muon be identified by the Čerenkov system as either an electron/pion or an electron/pion/kaon if the muon momentum is above 60 GeV. The muon identification requirement is the same.

The confidence level of the secondary vertex is required to be above 5%. The same $K^-\mu^+$ mass cut $0.95\ GeV/c^2 < M(MK\mu) < 1.855\ GeV/c^2$) is in effect. Figure 4.6.1 is the display of the $K^-\mu^+$ mass after all selection criteria.

4.6.2 D^0 Momentum Reconstruction

We force the neutrino momentum to be zero if $P^2_{\nu\ along\ D^0} > -0.7$ and drop the event if $P^2_{\nu\ along\ D^0} < -0.7$. Otherwise, the reconstruction of the 2 D^0 solutions is identical. We can compare the tagged analysis to the plots in Figure 4.6.2.

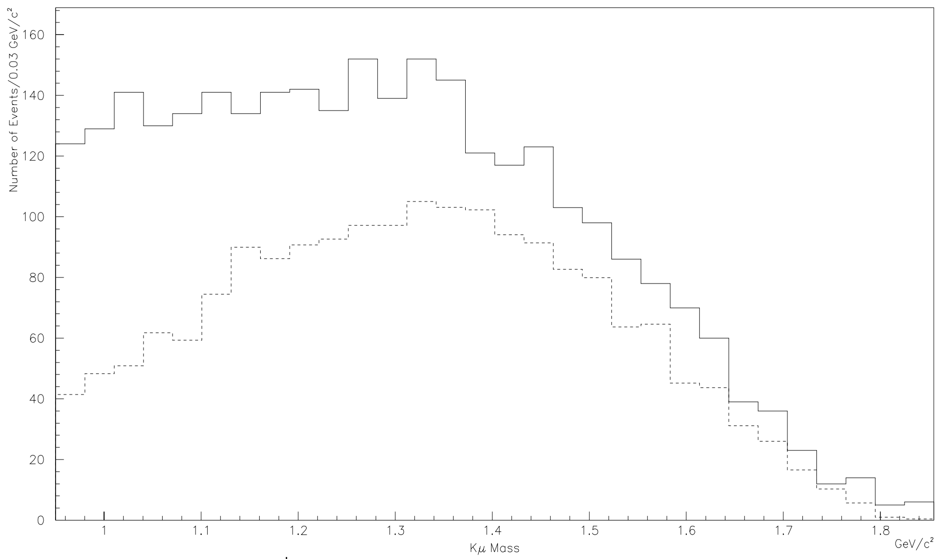

Figure 4.6.1 The $K^-\mu^+$ Mass after all selection criteria. The expected shape from the Monte Carlo for $D^0 \to K^-\mu^+\nu_\mu$ only is overlaid as a dashed line. Note that expected backgrounds from misidentification and $D \to K^*\mu^+\nu_\mu$ are not included in this the Monte Carlo plot. This plot gives us a feel for the amount of background present in the non–tag signal.

4.6.3 Kinematic Variables of Interest

We form bins in q^2 and in the muon momentum in the D^0 center of mass(E_μ). Using these two variables gives discrimination against backgrounds. Moreover, decreasing the bin size in these two variables will decrease the error in our yield measurement. Resolution effects and bin sizes are discussed in the systematics chapter.

4.7 Fitting the $K^-\mu^+$ Signal

We fit the data by building up a simulated data histogram in q^2 and E_μ using Monte Carlo and data that represents backgrounds. The pole mass and the yield are fit at the same time in a manner similar to the way we fit the D^{*+} signal.

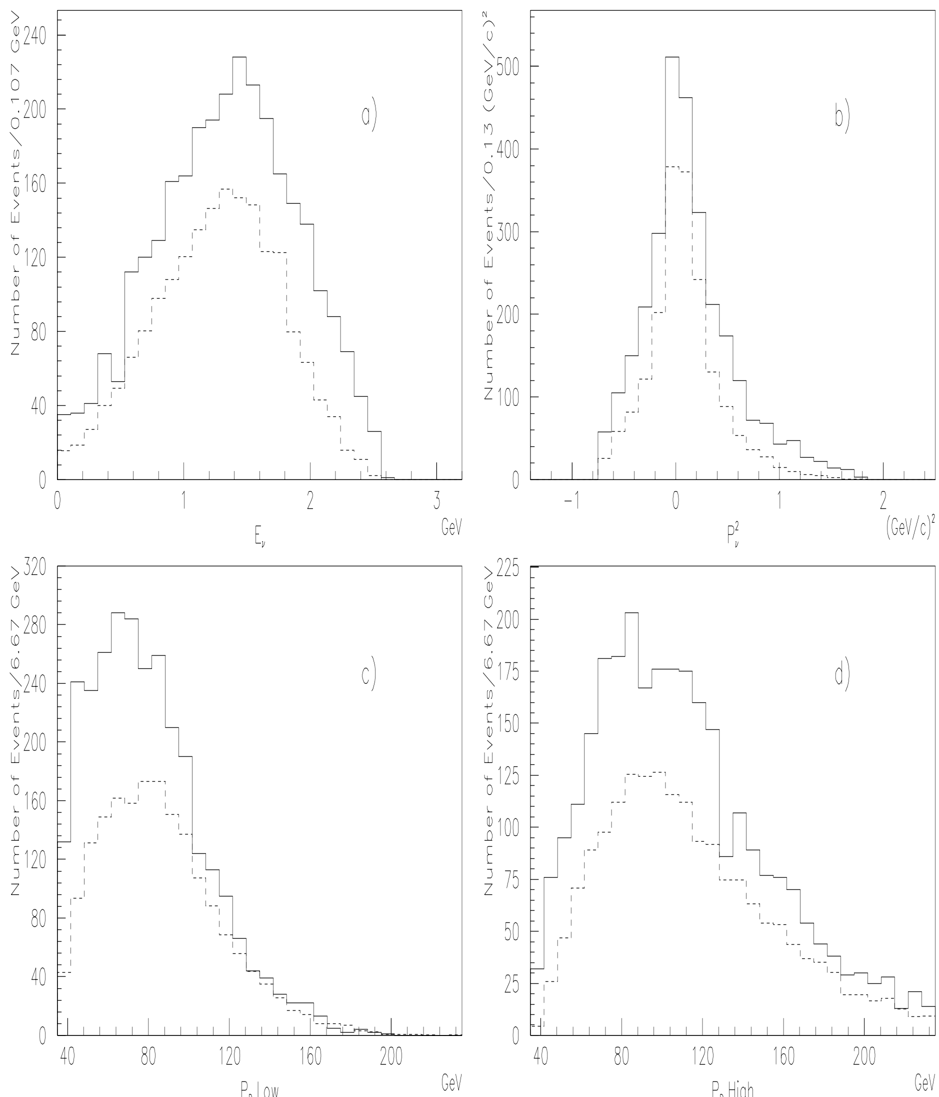

Figure 4.6.2 Plots of D^0 momenta reconstruction parameters: a)E_ν, b) $P^2_{\nu\ along\ l}$, c) Low D^0 lab momentum solution and d) High D^0 lab momentum solution. The expected shapes from the Monte Carlo for $D^0 \to K^-\mu^+\nu_m u$ decays are overlaid as dotted lines.

4.7.1 Making the Fit Histogram

The fit histogram is almost identical to the D^{*+} fit histogram. We have substituted a background that consists of data where $Q(K) = Q(\mu)$ for the background that we used for the D^{*+} case. The contributors to the fit histogram are featured in Figure 4.7.1.

4.7.2 Results of the Fit

To minimize the negative log likelihood, we use the MINUIT[31] package from CERN. The fit returns 819 ± 32 events in 1990, 1112 ± 40 events in 1991 and a pole mass of $1.86^{+0.10}_{-0.08}$. Figure 4.7.2 is the q^2 distribution with fit overlaid. The agreement appears quite good. A study of the reliability of the fitter and the systematic error associated with this measurement can be found in Chapter 5.

4.7.3 Fitting for f_-

We use the same procedure outlined above to find a value for the ratio $|f_-(0)/f_+(0)|$. Again, it is easier to fix m_{pole} and vary $|f_-(0)/f_+(0)|$ only so that we need not perform thousands of normalization integrals. Our cuts used in the analysis above lower our sensitivity to $|f_-(0)/f_+(0)|$ by a factor of 2. We find $|f_-(0)/f_+(0)| = 3.4 \pm 1.7$. A study of the systematic error associated with this result can be found in the systematics chapter.

4.8 The $K^-\pi^+$ Signal

The $K^-\pi^+$ has cuts that mimic the $K^-\mu^+$ signal. We have a further requirement on this signal that the kaon momentum be above 10 GeV. This cut is made because $D^0 \rightarrow K^-\pi^+$ is a two body decay, and our cuts on the pion momentum limit the phase space of the kaon. This cut retains about 90% of the $K^-\pi^+$ signal and decreases the error in the fit by 10%. In Figure 4.8.1 we display the effectiveness of the 10 GeV cut. The fit technique is the same as for the D^{*+} case.

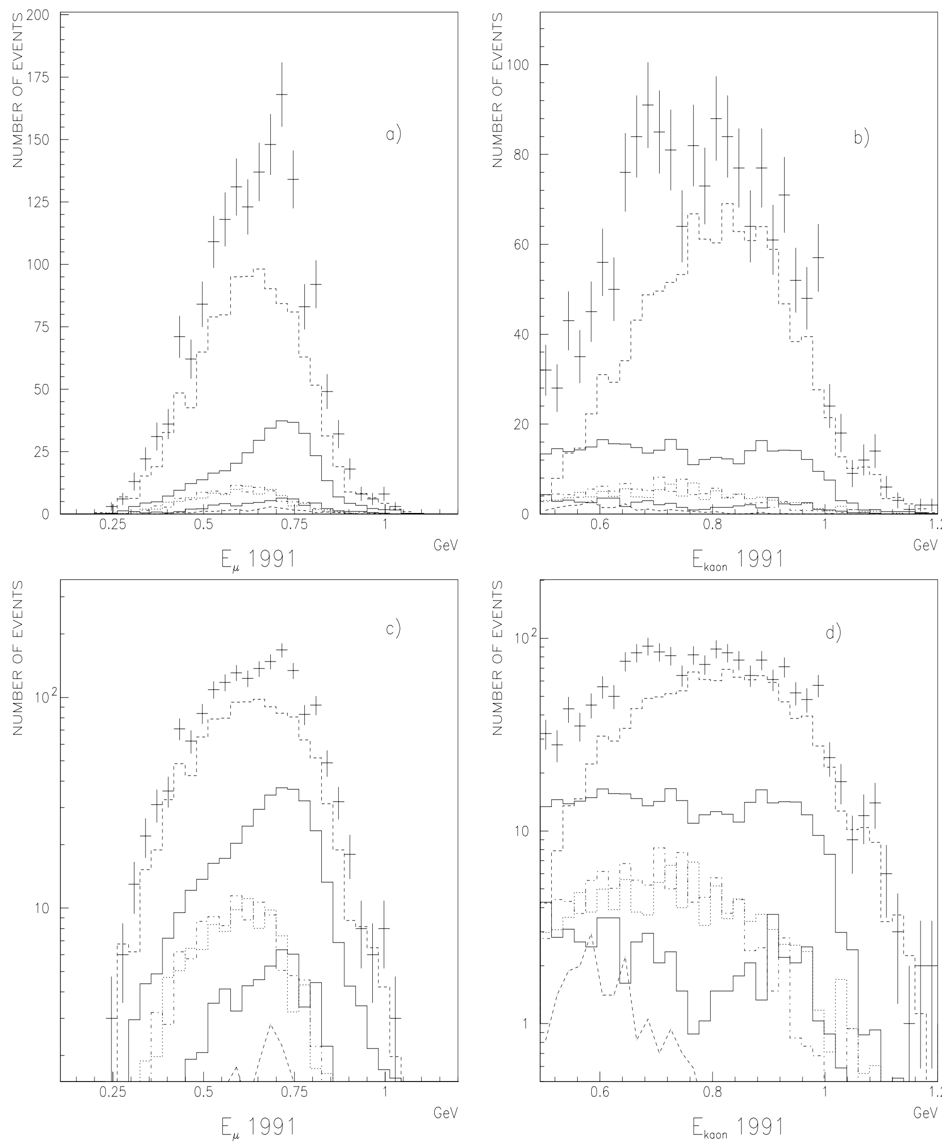

Figure 4.7.1 Plots of the fit histograms for E_μ and q^2 for 1990 and 1991: a) 1991 E_μ, b) 1991 q^2, c) 1991 E_μ on a log scale and d) 1991 q^2 on a log scale. Each plot contains the data histogram itself(error bars), the $D^0 \rightarrow K^-\mu^+\nu_\mu$ contribution(long dashes), the contribution from muon misidentified events(larger solid histogram), the $D^0 \rightarrow K^{*-}\mu^+\nu_\mu$ contribution(short dashes), the $D^+ \rightarrow K^{*0}\mu^+\nu_\mu$ contribution(dot dashes), $Q(K) = Q(\mu)$ background(smaller solid histogram) and the $D_s^+ \rightarrow \phi\mu^+\nu_\mu$ contribution(bins joined with long dashes).

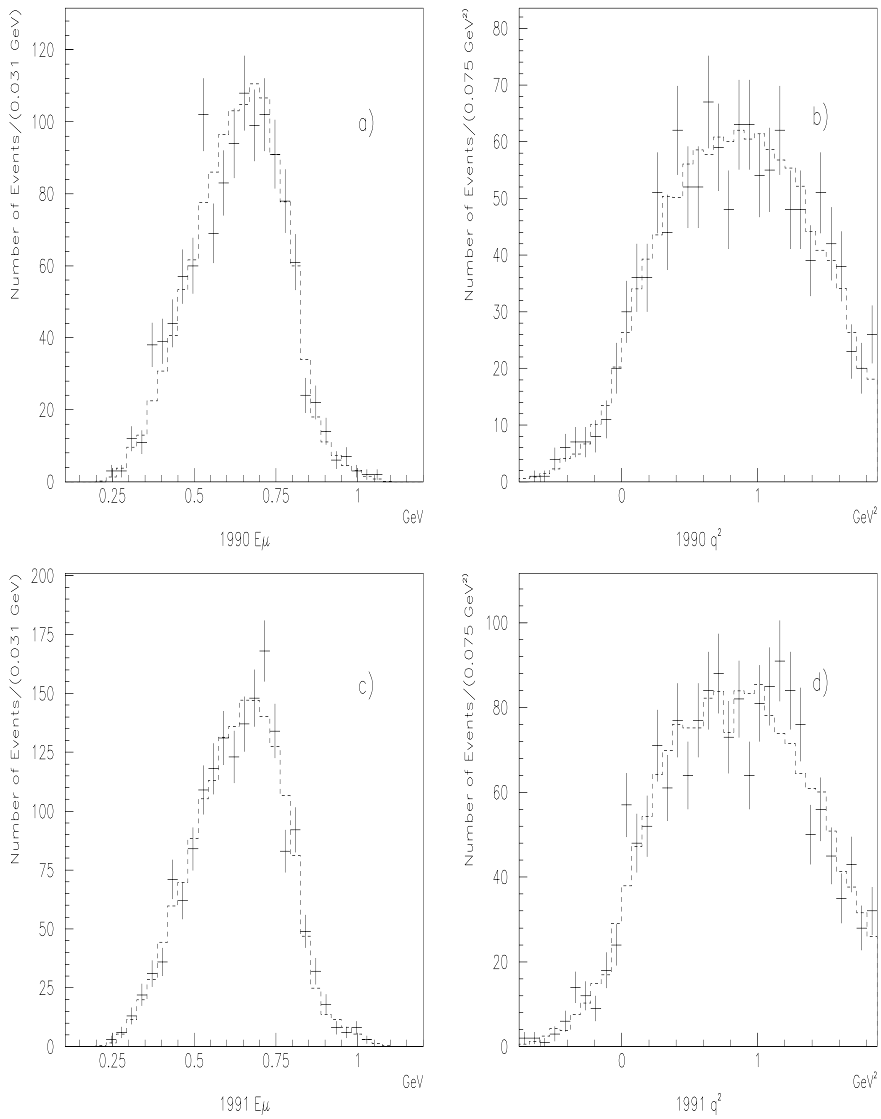

Figure 4.7.2 Plots of E_μ and q^2 for 1990 and 1991 data: a) 1990 E_μ with fit overlaid as a dashed line, b) 1990 q^2 with fit overlaid as a dashed line, c) 1991 E_μ with fit overlaid as a dashed line, d) 1991 q^2 with fit overlaid as a dashed line,

4.8.1 Results of the Fit

To minimize the negative log likelihood, we use the MINUIT[31] package from CERN. The fit returns 1720 ± 58 events in 1990 and 3821 ± 86 events

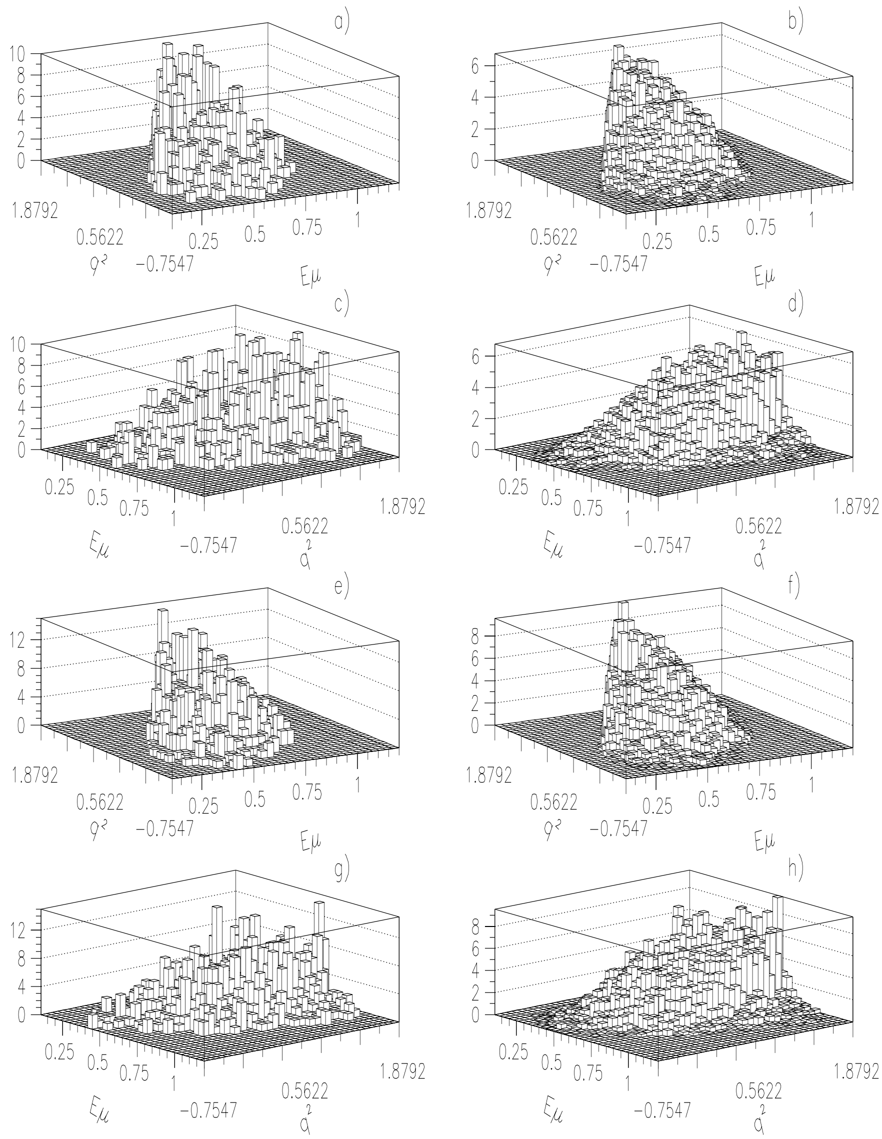

Figure 4.7.3 Plots of the 2 dimensional data and fit histograms: a) 1990 data, b) 1990 fit histogram, c) 1990 data(rotated), d) 1990 fit histogram(rotated), e) 1991 data, f) 1991 fit histogram, g) 1991 data(rotated) and h) 1991 fit histogram(rotated)

in 1991. Figure 4.8.2 is the $M(K^-\pi^+)$ distribution with fit overlaid. The agreement appears quite good. A study of the reliability of the fitter and the

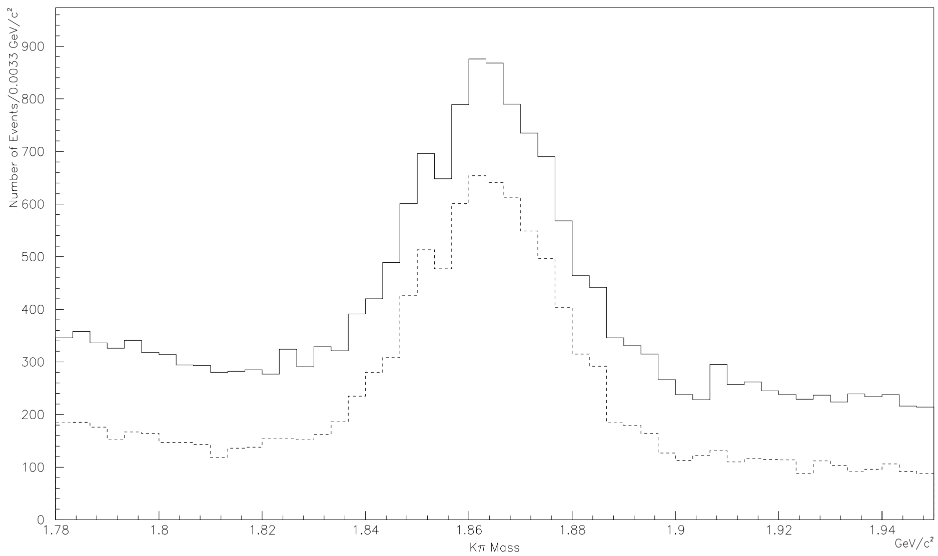

Figure 4.8.1 The $K^-\pi^+$ signal before(solid) and after(dashes) application of the 10 GeV/c momentum cut on the kaon.

systematic error associated with this measurement can be found in the chapter on systematics.

4.9 The Ratio of Branching Ratios, $\frac{BR(D^0 K^-\mu^+\nu_\mu)}{BR(D^0 K^-\pi^+)}$

To find the Ratio of Branching ratios between $BR(D^0 \rightarrow K^-\mu^+\nu_\mu)$ and $BR(D^0 \rightarrow K^-\pi^+)$, we use the following prescription.

$$\frac{BR(D^0 \rightarrow K^-\mu^+\nu_\mu)}{BR(D^0 \rightarrow K^-\pi^+)} = \frac{Yield\ D^0 \rightarrow K^-\mu^+\nu_\mu}{Yield\ D^0 \rightarrow K^-\pi^+} \frac{Efficiency(D^0 \rightarrow K^-\pi^+)}{Efficiency(D^0 \rightarrow K^-\mu^+\nu_\mu)} \tag{4.9.1}$$

where

$$Efficiency = \frac{\#\ of\ events\ accepted\ from\ Monte\ Carlo}{\#\ of\ events\ generated\ by\ Monte\ Carlo}. \tag{4.9.2}$$

The yields come from the fits above and the Monte Carlo events are simply counted from the histograms used in the fit procedure.

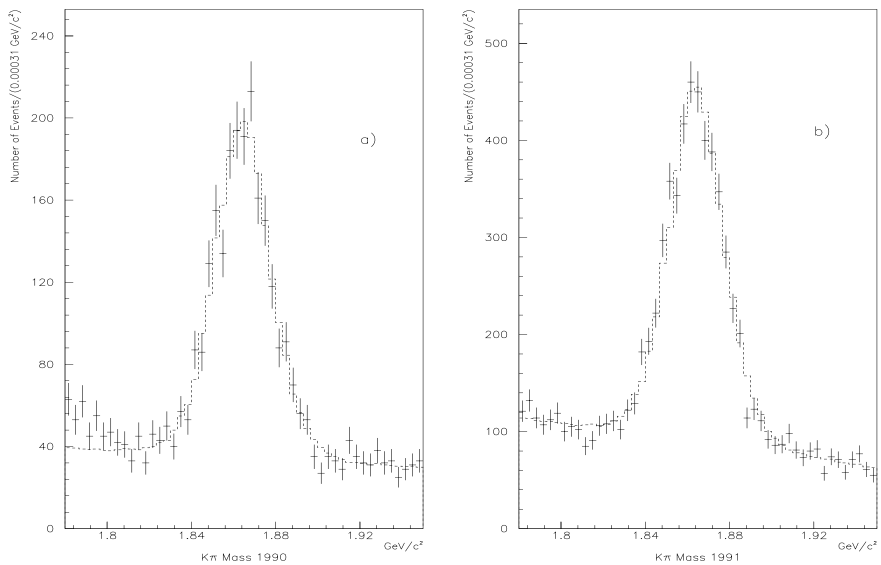

Figure 4.8.2 Plots of the $K^-\pi^+$ mass for 1990 and 1991 data: a) 1990 $K^-\pi^+$ mass with fit overlaid as a dashed line and b) 1991 $K^-\pi^+$ mass with fit overlaid as a dashed line. We have not included information below 1.82 GeV/c^2 in the fit to eliminate adding a representation for $D^0 \rightarrow K^+K^-$ in the fit histogram.

4.9.1 Results

The Ratio of Branching ratios for the non–D^{*+} analysis in 1990 is 0.870 ± 0.048 and 0.865 ± 0.038 in 1991. The result for the method which utilizes the D^{*+} is 0.845 ± 0.081 in 1990 and 0.849 ± 0.086 in 1991. Systematic effects, which increase the error and modify this result slightly, are considered in the next chapter.

4.10 The Ratio of Branching Ratios, $\frac{BR(D^0 \rightarrow K^{*-}\mu^+\nu_\mu)}{BR(D^0 \rightarrow K^-\mu^+\nu_\mu)}$

This ratio provides a test on various models used to predict physics in the charm sector. The trend is for the theories to predict this ratio to be ~ 1 (see Chapter 6), but most experiments are reporting a lower value.[24,23] We can improve the previous E687 measurement of this quantity[24] with a new measurement from this thesis.

The fit must be modified to remove the previously measured value of $\frac{BR(D^0\to K^{*-}\mu^+\nu_\mu)}{BR(D^0\to K^-\mu^+\nu_\mu)}$. Instead, we use our measurement of the $D^0 \to K^-\pi^+$ yield, the ratio $\frac{BR(D^+\to K^{*0}\mu^+\nu_\mu)}{BR(D^+\to K^-\pi^+\pi^+\pi^-)}$,[32] the measurements of $BR(D^0 \to K^-\pi^+)$,[33] $BR(D^+ \to K^-\pi^+\pi^+\pi^-)$,[34] τ_{D^0}[28] and τ_{D^+}.[28] We can then measure the ratio $\frac{BR(D^0\to K^{*-}\mu^+\nu_\mu)}{BR(D^0\to K^-\mu^+\nu_\mu)}$ in a constraint to the general fit.

4.10.1 Making the Fit Histogram

The likelihood is modified to include the constraint on the ratio $\frac{BR(D^0\to K^{*-}\mu^+\nu_\mu)}{BR(D^0\to K^-\mu^+\nu_\mu)}$, and we allow this ratio to vary freely in the fit. Otherwise, the formulation of the fit histogram is identical.

4.10.2 Forming the Likelihood

The original likelihood $\mathcal{L}_0$ is modified to include the constraint:

$$\begin{aligned} &\frac{BR(D^0 \to K^{*-}\mu^+\nu_\mu)}{BR(D^0 \to K^-\mu^+\nu_\mu)}\frac{Yield(D^0 \to K^-\mu^+\nu_\mu)}{Eff(D^0 \to K^-\mu^+\nu_\mu)} = \\ &\quad\frac{BR(D^0 \to K^{*-}\mu^+\nu_\mu)}{BR(D^0 \to K^-\pi^+)}\frac{Yield(D^0 \to K^-\pi^+)}{Eff(D^0 \to K^-\pi^+)} \end{aligned} \tag{4.10.1}$$

such that

$$\mathcal{L} \to \mathcal{L}_0 \times exp(-.5\left(\frac{(B_K - VB_K)}{\sigma_{B_K}}\right)^2) \times exp(-.5\left(\frac{(R_K - VR_K)}{\sigma_{R_K}}\right)^2) \tag{4.10.2}$$

where

$B_K = \frac{BR(D^0\to K^{*-}\mu^+\nu_\mu)}{BR(D^0\to K^-\pi^+)}$

$\sigma_{B_K} =$ error on B_K

$VB_K =$ an additional variable in the fit

$R_K = \frac{Yield(D^0\to K^-\pi^+)}{Eff(D^0\to K^-\pi^+)}$

$\sigma_{R_K} =$ error on R_K

$$VR_K = \frac{Yield(D^0 \to K^- \mu^+ \nu_\mu)}{Eff(D^0 \to K^- \mu^+ \nu_\mu)} \frac{\frac{BR(D^0 \to K^{*-} \mu^+ \nu_\mu)}{BR(D^0 \to K^- \mu^+ \nu_\mu)}}{\frac{BR(D^0 \to K^{*-} \mu^+ \nu_\mu)}{BR(D^0 \to K^- \pi^+)}}$$

and $\frac{BR(D^0 \to K^{*-} \mu^+ \nu_\mu)}{BR(D^0 \to K^- \mu^+ \nu_\mu)}$ is now a variable in the fit. Note that we split the data into 1990 and 1991 samples for this measurement as well.

4.10.3 Results of the Fit

We find:

$$\frac{BR(D^0 \to K^{*-} \mu^+ \nu_\mu)}{BR(D^0 \to K^- \mu^+ \nu_\mu)} = 0.62 \pm 0.05 \tag{4.10.3}$$

Figure 4.10.1 is the projection of q^2 and E_μ overlaid with the new fit results. No gross deviations are seen. A study of the systematic error associated with this measurement can be found in the chapter on systematics.

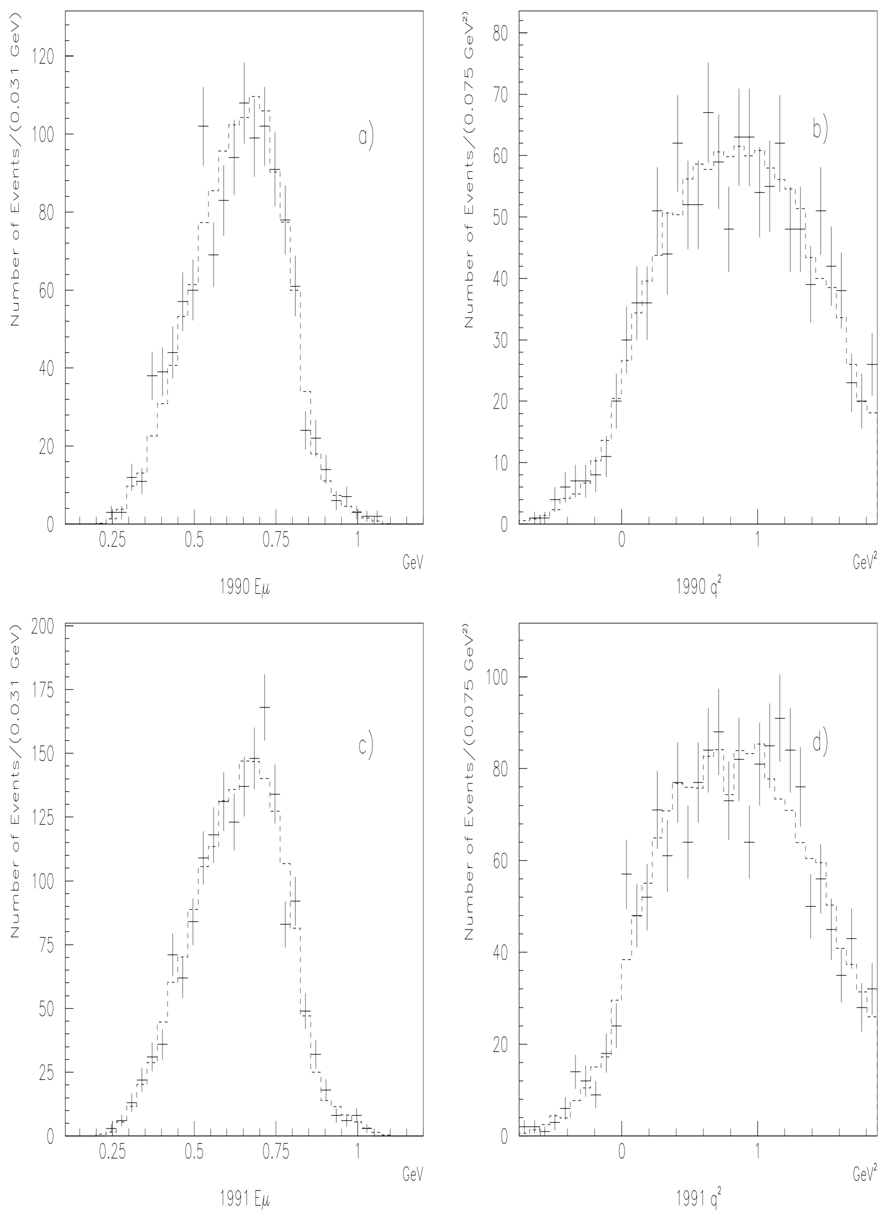

Figure 4.10.1 Plots of E_μ and q^2 for 1990 and 1991 data with the fit fit used for the determination of $\frac{BR(D^0 \rightarrow K^{*-}\mu^+\nu_\mu)}{BR(D^0 \rightarrow K^-\mu^+\nu_\mu)}$: a) 1990 E_μ with fit overlaid as a dashed line, b) 1990 q^2 with fit overlaid as a dashed line, c) 1991 E_μ with fit overlaid as a dashed line, d) 1991 q^2 with fit overlaid as a dashed line.

CHAPTER 5

SYSTEMATIC STUDIES

Besides the statistical error associated with the number of events measured, there is error from the imprecision of the representation of the signal used to simulate the data.

It is important to identify sources of systematic error and minimize the impact on the final measurement. Some sources of error prove intangible to the experimenter, and the error from these sources must be estimated and combined with the statistical error to get a true representation of the uncertainty in the final result. In this chapter we will present four types of systematic checks.

1) There will be qualitative checks of the simulation. Some checks of this type have been shown already. One example is the reproducibility of the muon simulation.

2) The quantities used in the fit will be investigated. A good example of this kind of error is the uncertainty in the level of misidentification and how it impacts our final result.

3) We will investigate the behavior of the results returned by the fit. In so doing, we can assess the systematic error stemming from other sources. The classic check for an analysis using separated vertices is the behavior of a given result compared to the significance of separation of the vertices(l/σ).

4) We look at the validity of the fit itself. It is necessary to check the errors returned by the fitter and determine the "goodness" of the fit. In a least squares fit, "goodness" of the fit is commonly expressed as a confidence level.

Finally, we will discuss briefly the technique used in other analyses of this type in E687 to combine sources of systematic error. We then combine all sources of systematic error we have measured to determine the effect on our results.

All sources of systematic error can never be found, but we can use the above checks and borrow some other checks from different analyses to assure ourselves that our quoted results are correct.

5.1 Qualitative Checks

5.1.1 Event Generation

The Monte Carlo can contribute error to the final results in any number of ways. If the production model or the matrix element governing the decay of interest is incorrect, error is injected into the event in the initial stages of the simulation.

To fragment a photon into two charm particles in the presence of a nucleus, a model must be used. The Monte Carlo presently uses the Pythia 5.6[19] package to calculate the photon–gluon fusion cross section and the Jetset 7.3[19] package to fragment the charm. Both of these packages are subsets of the main LUND[19] package. A comparison to the E687 data and the LUND[19] package can be found in reference [35]. Briefly, we find an analysis of fully and partially reconstructed $D\overline{D}$ pairs shows "reasonable agreement with most correlations predicted by the tree-level photon-gluon fusion process and the Lund string fragmentation model."[35] The main concerns for this analysis are the production model underestimates the transverse momentum between $D\overline{D}$ pairs or that the model will not properly model the energy of the produced $D\overline{D}$ pair. If the transverse momentum is improperly modelled, the wrong sign representation of the background, events where the muon and the pion in the tagged analysis have the opposite charge, will be of marginal utility. Since there is some degree of correlation between the D and the opposite side $\overline{D}$, events can get into the wrong sign background if a $\overline{D}^*$ decays into a charged pion with the dynamical nature of a pion from the decay $D^* \rightarrow D$. The proper modelling of the energy of the produced $D's$ will ease the demand on the simulation of the hadronic energy trigger.

We know that there is some production of $D^{**} \rightarrow D$ that is not reproduced by the simulation. Evidence that additional production is present in the data is seen by looking at the yield of $D^0 \rightarrow K^-\pi^+$ in the sidebands($M(D^*) - M(D^0) > 0.15\ GeV/c^2$) of the reconstructed mass difference $M(D^*) - M(D^0)$ distribution and comparing it to the yield of $D^0 \rightarrow K^-\pi^+$ in the signal($M(D^*) - M(D^0) < 0.15\ GeV/c^2$) region. Table 5.1.1 is a summary of the shortfall in the Monte Carlo.

Table 5.1.1 D^{*+} analysis yield comparisons

Sample	D^{*+} signal	D^{*+} sideband	$\frac{sideband}{signal}$
1991 data	770 ± 29	476 ± 29	$.62 \pm .04$
1990 data	348 ± 19	202 ± 19	$.58 \pm .07$
1991 Monte Carlo	6041 ± 78	2329 ± 51	$.39 \pm .01$
1990 Monte Carlo	3442 ± 59	1383 ± 39	$.40 \pm .01$

The chief concerns for this added signal are that the choice of solution in the tag analysis will be affected by excess $D^0 \rightarrow K^-\pi^+$ in the wrong sign background and that the momentum distribution of the produced charm will affect the non–tag analysis. In Figure 5.1.1 we compare the D^0 momentum from the $D^0 \to K^-\pi^+$ non–tag analysis for data and Monte Carlo. Since we cannot directly measure the D^0 momentum in the $D^0 \to K^-\mu^+\nu_\mu$ analysis, we estimate the effect, if any, of the variation in the D^0 momenta using other reconstructed quantities.

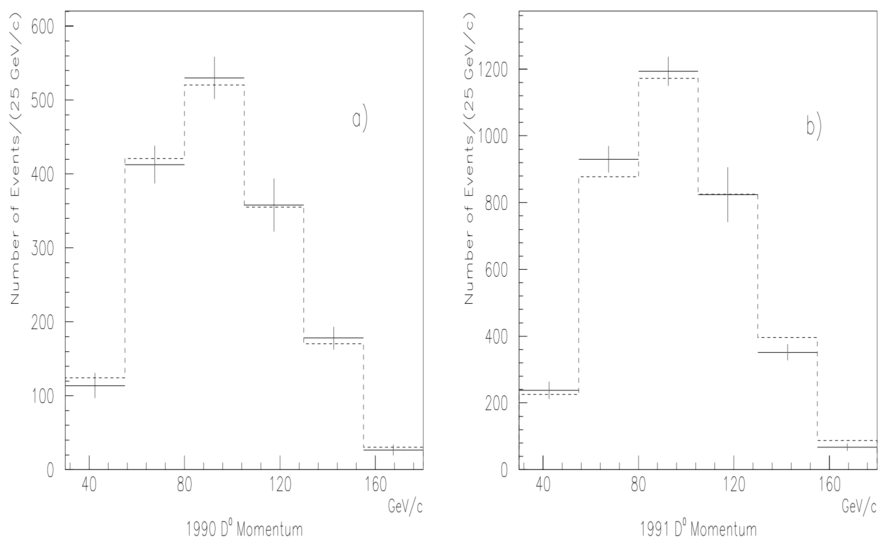

Figure 5.1.1 The D^0 momentum in a) 1990 and b) 1991. Note the poorer agreement in the 1991 signal.

Once the charm meson has been created by the production model it decays. The particles resulting from the decay process do not always come out in random directions or energies. There is physics locked in the particle decay process, and it is the physics that we wish to measure or model. To test the decay generation process for the decay $D^0 \to K^-\mu^+\nu_\mu$ we use the expression for the electron decay

$$\frac{d^2,}{dE_e dE_K} \propto 2(P_{D^0} \cdot P_e)(P_{D^0} \cdot P_{\nu_e}) - M_{D^0}^2 (P_e \cdot P_{\nu_e}) \tag{5.1.1}$$

in conjunction with our multi–particle phase space generator and fit the projections of the electron and kaon spectra in the D^0 center of mass:

$$\frac{d,}{dE_K} \propto M_{D^0} P_K^3 \tag{5.1.2}$$

$$\frac{d,}{dE_e} \propto M_{D^0} \frac{E_e^2 (\frac{M_{D^0}^2 - M_k^2}{2M_{D^0}} - E_e)^2}{M_{D^0} - 2E_e}. \tag{5.1.3}$$

The results of the fit are shown in Figure 5.1.2. The generator delivers an excellent representation of the distributions. No systematic error is expected from the matrix element or the decay generator.

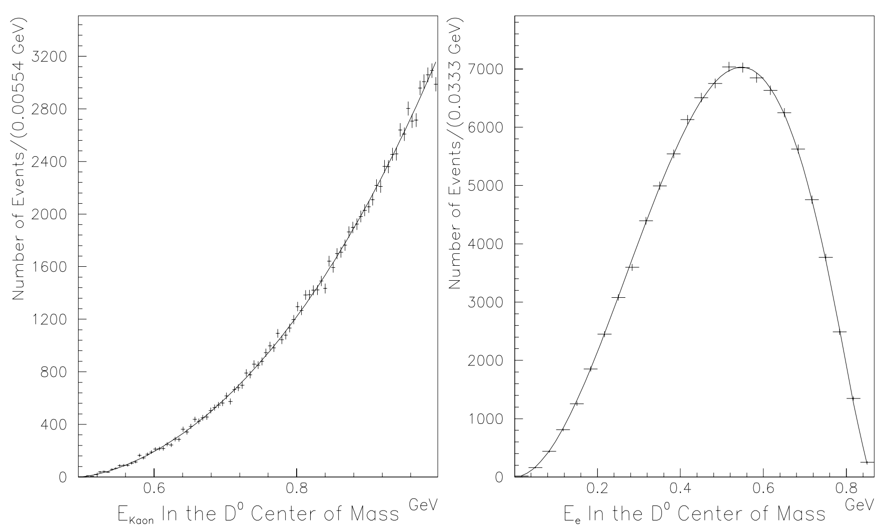

Figure 5.1.2 Generated and expected shapes of the q^2 and E_e spectra.

There is another significant decay process to be modelled. We check the matrix element for the decays $D^+ \to \overline{K}^{*0}\mu^+\nu_\mu$ and $D^0 \to K^{*-}\mu^+\nu_\mu$ by comparing our simulated signal to data. Specifically, we analyze the signal $D^+ \to \overline{K}^{*0}\mu^+\nu_\mu$ by looking for the decay $\overline{K}^{*0} \to K^-\pi^+$ in the same vertex as the muon. We then proceed to reconstruct the event as if the pion were not present. We look at the quantities q^2 and E_μ and check the cleanliness of the signal using the $\overline{K}^{*0}$ peak. Both the high and low D^0 momentum solutions are investigated. Agreement between the simulation and the analysis of data is good(Figure 5.1.3).

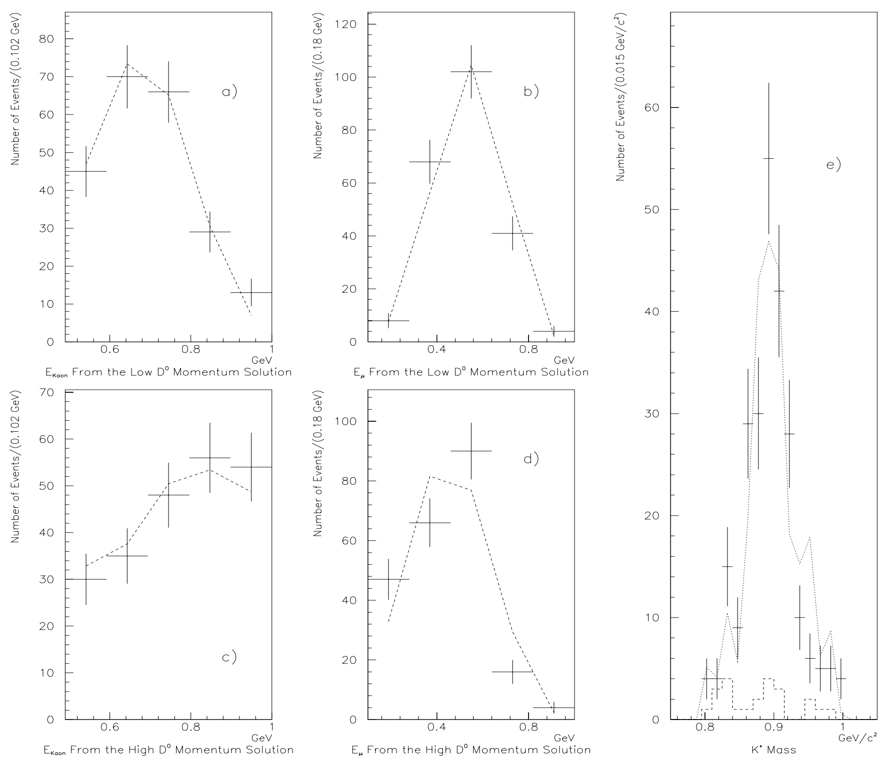

Figure 5.1.3 The agreement between the simulated and 1990 $D^+ \to K^{*0}\mu^+\nu_\mu$ signals reconstructed as $D^0 \to K^-\mu^+\nu_\mu$.

5.1.2 Reconstruction Methods

Of primary importance in the reconstruction of the $D^0 \rightarrow K^-\mu^+\nu_\mu$ signal is the selection of the primary vertex where the incoming photon converts into a charm particle and an anti–charm particle. We know that the selection is not perfect. Sometimes the charm opposite to the particle we are interested in can pull the solution away from the true location. Embedded e^+e^- events and secondary hadronic interactions can have this effect as well.

The best test of our selection method is to try a completely different type of vertex algorithm. Instead of the free–form method we use in the analyses presented earlier, we try a "candidate driven" vertexing algorithm. This technique is commonly used for our lifetime analyses.[28,29] Briefly, the resultant momentum vector from our secondary($K^-\mu^+$) vertex is used as a seed to find events consistent with the hypothesis that a vertex exists somewhere along the seed vector. Use of this other method leaves our results invariant.(see Table 5.1.2)

Table 5.1.2 Vertexing Method Results

Method	Yield for tagged analysis	Yield after 10^{-4} $ISO2$ cut
Free–form	242	184
Candidate Driven	241	181

Another test of the vertexing methodology involves looking at $D^0 \rightarrow K^-\pi^+$ events where $P^2_{\nu\ along\ D} > 0$ which will occur part of the time due to resolution smearing. The usual boost analysis is done and E_K is computed. To simulate noise we subtract events in the region $\pm 4 \rightarrow 6\sigma$ away from the $K^-\pi^+$ central mass peak from the events within $\pm 2\sigma$ of the $K^-\pi^+$ central

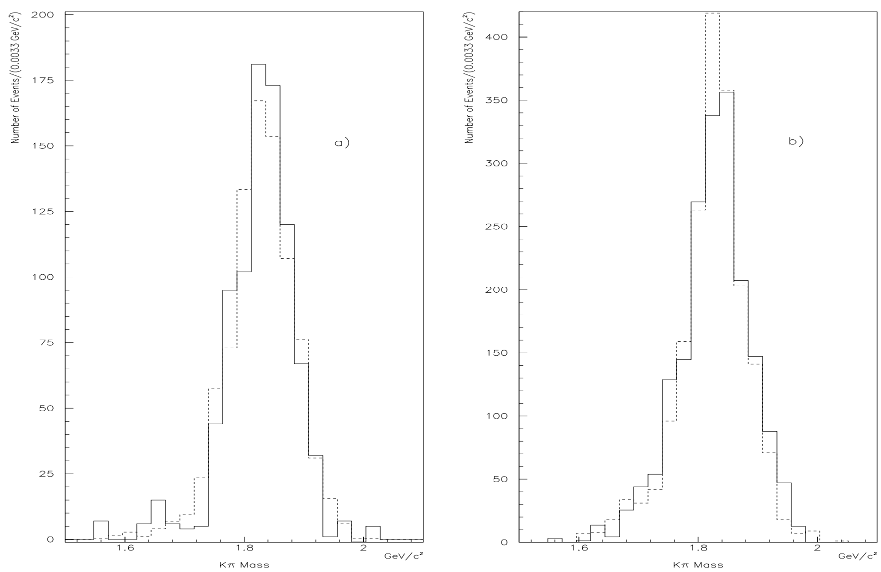

Figure 5.1.4 The simulated and reconstructed q^2 resolution using the $D^0 \to K^-\pi^+$ data samples.

mass peak. Figure 5.1.4 is the distribution of E_K for both 1990 and 1991 $D^0 \to K^-\pi^+$ samples. Agreement looks good.

5.1.3 Detector Simulations

We have already seen checks of the muon simulation in a very controlled calibration environment. Now we can take our fit results and look at some detector responses. These checks are different from quantitative checks done in a later section. We are looking for gross problems now.

We first want to check the projected x and y positions of tracks identified as muons. We get the distribution from the data and from the information used to create the fit histogram. We see from Figure 5.1.5 and Figure 5.1.6 that agreement is excellent in 1990 and acceptable in 1991.

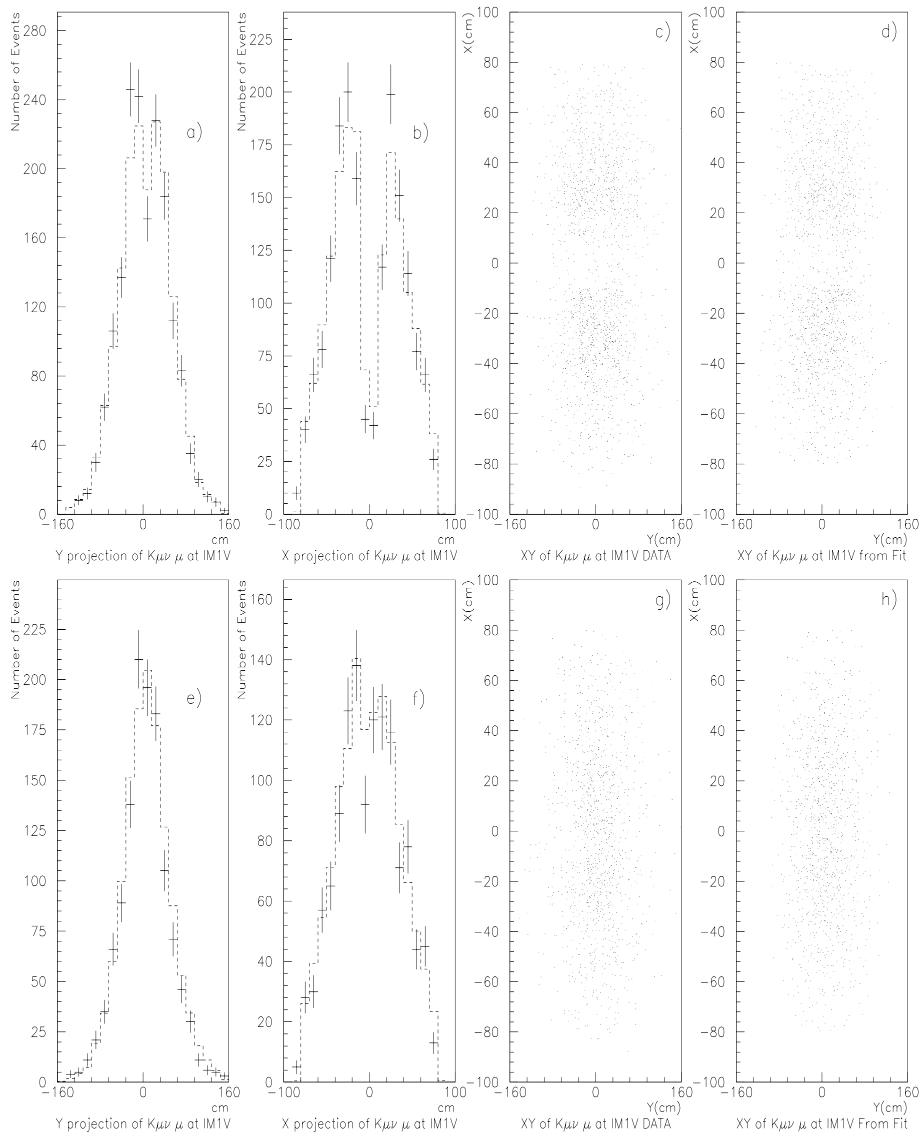

Figure 5.1.5 The position dependence of the reconstructed $D^0 \to K^-\mu^+\nu_\mu$ muon(error bars) and the simulated signal(dashed line) for the a)–d), 1991 sample and the e)–h) 1990 sample.

The other system that requires a closer look is the Čerenkov system. These detectors have been studied intensively for other analyses. We take data from the tagged analysis of $D^0 \to K^-\mu^+\nu_\mu$, subtract the wrong sign background, and look at the distribution of Čerenkov identification codes.

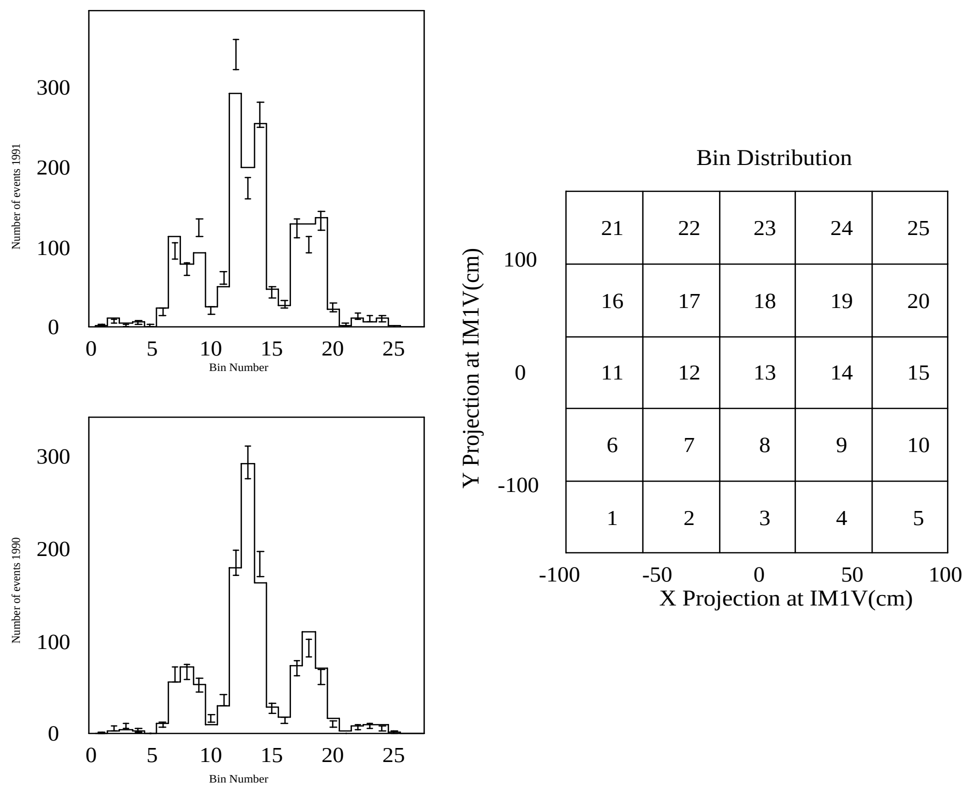

Figure 5.1.6 Alternate check of the position dependence of the muon system. Instead of projecting the X,Y behavior, we separate the data into two dimensional bins. Again, agreement in 1990 is better than 1991. When viewing these plots, it must be remembered that other detectors contribute to the acceptance as well. For instance, position dependent efficiencies in the PWC's are not modelled. The data is represented by the error bars.

In Figure 5.1.7 we see the only significant departure from data occurs for category $ISTATP = 0$ soft pions in the 1990 analysis.

5.2 Quantities Used in the Fit

We can assign some of the normalized shapes we use in the fit magnitudes based on their expected yields, or their expected yield relative to $D^0 \rightarrow K^{*-}\mu^+\nu_\mu$. This section describes the additional error in our fit result given the uncertainty of the information we put into the fit.

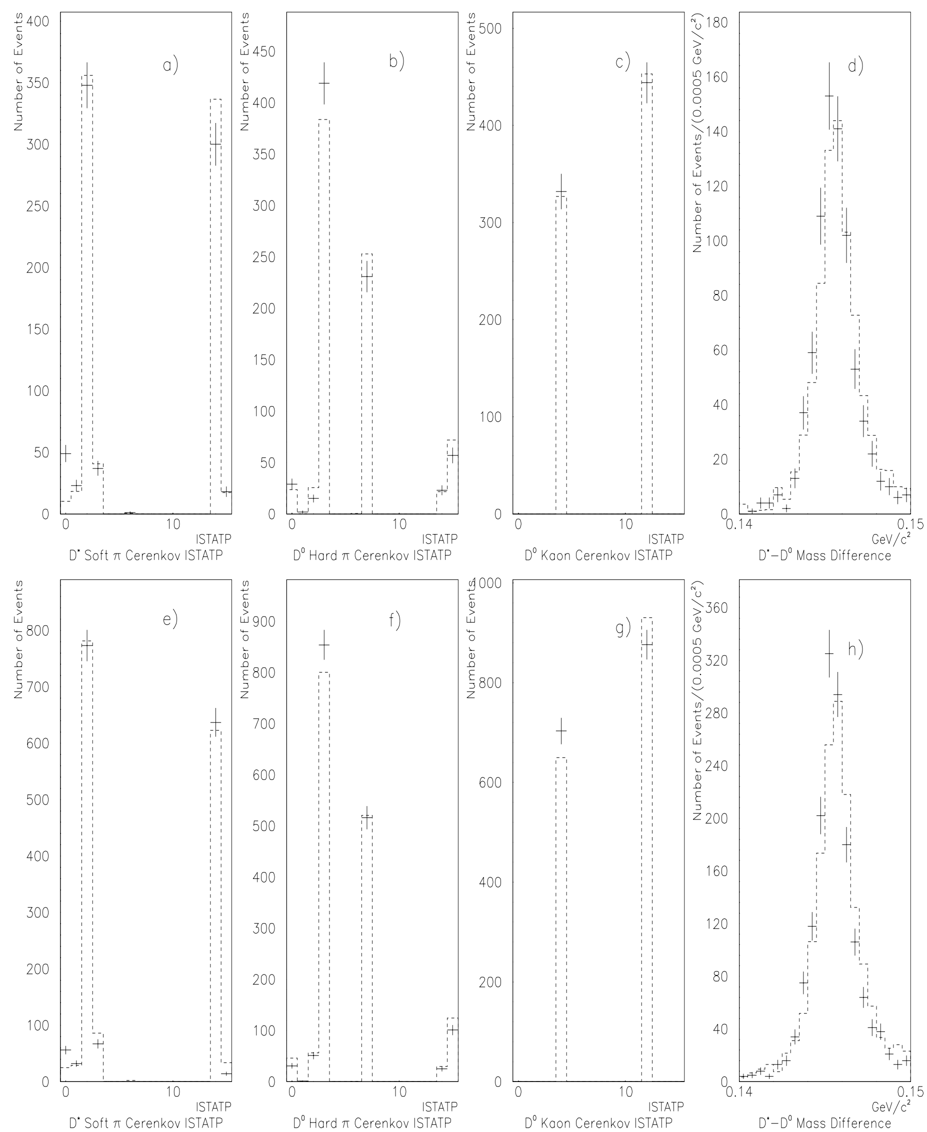

Figure 5.1.7 The Čerenkov codes for the Kaon, hard pion and soft pion using the tagged $D^0 \to K^-\pi^+$ sample for a)–d), 1990 and e)–h) 1991.

5.2.1 The Relative Rates of the Decays $D^0 \to K^{*-}\mu^+\nu_\mu$ and $D^0 \to K^-\mu^+\nu_\mu$

The main idea of the fit procedure used in the $D^0 \to K^-\mu^+\nu_\mu$ analysis is we can parameterize some backgrounds. Other experiments have even measured some of the backgrounds relative to $BR(D^0 \to K^-\mu^+\nu_\mu)$, and from their measurements we gain information on both the shape of the background and the decay of interest via the correlation between decays.

The primary background in the tagged sample comes from the decay $D^0 \to K^{*-}\mu^+\nu_\mu$ where $K^{*-} \to K^-\pi^0$. We have several measurements of the ratio of branching ratios to link the $D^0 \to K^-\mu^+\nu_\mu$ and $D^0 \to K^{*-}\mu^+\nu_\mu$ decays. (see Table 5.2.1)

Table 5.2.1 $BR(D^0 \to K^{*-}l^+\nu_l)/BR(D^0 \to K^-l^+\nu_l)$ Measurements

Experiment	Measurement	Value	Reference
CLEO	$\frac{BR(D^0 \to K^{*-}e^+\nu_e)}{BR(D^0 \to K^-e^+\nu_e)}$	$.62 \pm .08$	[23]
E687	$\frac{BR(D^0 \to K^{*-}\mu^+\nu_\mu)}{BR(D^0 \to K^-\mu^+\nu_\mu)}$	$.59 \pm .10 \pm .13$	[32]
E691	$\frac{BR(D^0 \to K^{*-}e^+\nu_e)}{BR(D^0 \to K^-e^+\nu_e)}$	$.55 \pm .14$	[36]

The value we use for the fit is:

$$\frac{BR(D^0 \to K^{*-}\mu^+\nu_\mu)}{BR(D^0 \to K^-\mu^+\nu_\mu)} = 0.60 \pm 0.06 \ . \tag{5.2.1}$$

We have combined results ignoring any phase space and model motivated corrections. Including these effects is expected to change the value by 0.01.[37]

To estimate the contribution to the final error from the uncertainty in this ratio, we redo the fit using the $\pm 1\sigma$ errors of the combined value and find:

$$\delta(\%)\frac{BR(D^0 \to K^-\mu^+\nu_\mu)}{BR(D^0 \to K^-\pi^+)} = 1.4\% \tag{5.2.2}$$

$$\delta m_{pole} = \pm 0.03 \ . \tag{5.2.3}$$

This error is not included in our new measurement of

$$\frac{BR(D^0 \rightarrow K^{*-}\mu^+\nu_\mu)}{BR(D^0 \rightarrow K^-\mu^+\nu_\mu)}. \tag{5.2.4}$$

5.2.2 $D^0 \rightarrow K^{*-}\mu^+\nu_\mu$ Polarization and Form Factors

In addition to the value of the above ratio, there is uncertainty involved in our understanding of the physics locked into the decay distribution of the decays $D^0 \rightarrow K^{*-}\mu^+\nu_\mu$ and $D^+ \rightarrow \overline{K}^{*0}\mu^+\nu_\mu$. The physics parameters we measure come from the expression for the rate in the W helicity representation:[27]

$$\begin{aligned}
&\frac{d^4,}{dM^2_{K\pi}\ dt\ dcos\theta_\nu\ dcos\theta_\mu} = \\
&G_F^2|V_{cs}|^2\frac{3}{2(4\pi)^5}\frac{M_{K^*}}{M_D^2 M_{K\pi}}\frac{M_{K^*},}{(M^2_{K\pi}-M^2_{K^*})^2+M^2_{K^*},\,^2}Kt\left(1-\frac{m_\mu^2}{t}\right)^2 \\
&\big(sin^2\theta_\nu((1+cos\theta_\mu)^2|H_+(t)|^2+(1-cos\theta_\mu)^2|H_-(t)|^2) \\
&+4cos^2\theta_\nu sin^2\theta_\mu|H_0(t)|^2-2sin^2\theta_\nu sin^2\theta_\mu cos2\chi Re(H_+^*H_-) \\
&-2sin\theta_\nu cos\theta_\nu sin\theta_\mu(1+cos\theta_\mu)cos\chi Re(H_+^*H_0) \\
&+4sin\theta_\nu cos\theta_\nu sin\theta_\mu(1-cos\theta_\mu)cos\chi Re(H_-^*H_0) \\
&+\left(\frac{m_\mu^2}{t}\right)terms\Bigg)
\end{aligned} \tag{5.2.5}$$

where

$$H_\pm(t) = (M_D+M_{K\pi})A_1(t) \mp 2\frac{M_D K}{M_D+M_{K\pi}}V(t) \tag{5.2.6}$$

$$\begin{aligned}
&H_0(t) = \\
&\frac{1}{M_{K\pi}\sqrt{t}}\left((M_D^2-M^2_{K\pi}-t)(M_D+M_{K\pi})A_1(t)-4\frac{M_D^2K^2}{M_D+M_{K\pi}}A_2(t)\right)
\end{aligned} \tag{5.2.7}$$

$$A_{1,2}(t) = \frac{A_{1,2}(0)}{1 - t/M_A^2}, \; M_A = 2.5GeV/c^2 \tag{5.2.8}$$

$$V(t) = \frac{V(0)}{1 - t/M_V^2}, \; M_V = 2.1GeV/c^2 \tag{5.2.9}$$

and we measure,

$$R_v = \frac{V(0)}{A_1(0)} \text{and } R_2 = \frac{A_2(0)}{A_1(0)}. \tag{5.2.10}$$

The magnitude of $A_1(0)$ is calculated using the integrated partial rate, the measurement of $BR(D^+ \to K^-\pi^+\pi^+)$, the D^+ lifetime measurement and the value of V_{cs}. Each H_x above corresponds to a different spin state of the W.

To determine the amount of systematic error we add to the final result, we reanalyzed the signal with R_v and R_2 at their 1 σ bounds. We find that the values we use for R_v and R_2:[32,38]

$$R_v = 1.88 \pm 0.27 \tag{5.2.11}$$

$$R_2 = 0.8 \pm 0.16 \tag{5.2.12}$$

contribute:

$$\delta(\%)\frac{BR(D^0 \to K^-\mu^+\nu_\mu)}{BR(D^0 \to K^-\pi^+)} = \pm 0.5\% \tag{5.2.13}$$

$$\delta m_{pole} = \pm 0.01 \tag{5.2.14}$$

$$\delta(\%)\frac{BR(D^0 \to K^{*-}\mu^+\nu_\mu)}{BR(D^0 \to K^-\mu^+\nu_\mu)} = 0.5\% \tag{5.2.15}$$

to the final result.

5.2.3 The Relative Production of D^+ and D^0

We use the production ratio to determine the amount of D^+ contamination from $D^+ \to \overline{K}^{*0}\mu^+\nu_\mu$ and to determine the amount of D_s^+ contamination from $D_s^+ \to \phi\mu^+\nu_\mu$ in the $D^0 \to K^-\mu^+\nu_\mu$ fit.

The value we use for the ratio

$$\frac{Production(D^+)}{Production(D^0)} = 0.42 \pm 0.05, \tag{5.2.16}$$

was determined by measuring the yields of $D^0 \to K^-\pi^+$, $D^0 \to K^-\pi^+\pi^+\pi^-$ and $D^+ \to K^-\pi^+\pi^+$ and comparing to known branching ratios.[30] This choice adds the following uncertainties:

$$\delta(\%)\frac{BR(D^0 \to K^-\mu^+\nu_\mu)}{BR(D^0 \to K^-\pi^+)} = 1.1\% \tag{5.2.17}$$

$$\delta m_{pole} = \pm 0.02 \tag{5.2.18}$$

$$\delta(\%)\frac{BR(D^0 \to K^{*-}\mu^+\nu_\mu)}{BR(D^0 \to K^-\mu^+\nu_\mu)} = 1.1\%. \tag{5.2.19}$$

to our measurement.

5.2.4 The Production of $(D_s^+ \to \phi\mu^+\nu_\mu)$ relative to $(D^+ \to K^{*0}\mu^+\nu_\mu)$

The method of calculating this ratio was mentioned in Chapter 4. We estimate the uncertainty in the level of this contamination adds the following error to the final results:

$$\delta(\%)\frac{BR(D^0 \to K^-\mu^+\nu_\mu)}{BR(D^0 \to K^-\pi^+)} = 0.5\% \tag{5.2.20}$$

$$\delta m_{pole} = \pm 0.0 \tag{5.2.21}$$

$$\delta(\%)\frac{BR(D^0 \to K^{*-}\mu^+\nu_\mu)}{BR(D^0 \to K^-\mu^+\nu_\mu)} = 0.5\%. \tag{5.2.22}$$

5.2.5 The Lifetimes τ_{D^0}, τ_{D^+} and $\tau_{D_s^+}$

A ratio of lifetimes appears in the calculation for the estimated $D^+ \to \overline{K}^{*0}\mu^+\nu_\mu$ and $D_s^+ \to \phi\mu^+\nu_\mu$ yields for the $\frac{BR(D^0\to K^-\mu^+\nu_\mu)}{BR(D^0\to K^-\pi^+)}$ measurement and the estimated $D^0 \to K^{*-}\mu^+\nu_\mu$, $D^+ \to \overline{K}^{*0}\mu^+\nu_\mu$ and $D_s^+ \to \phi\mu^+\nu_\mu$ yields for the $\frac{BR(D^0\to K^{*-}\mu^+\nu_\mu)}{BR(D^0\to K^-\mu^+\nu_\mu)}$ measurement. The values we use:

$$\tau_{D^0} = 0.413\pm0.005ps^{[28]},\ \tau_{D^+} = 1.048\pm0.019ps^{[28]} \text{ and } \tau_{D_s^+} = 0.475\pm0.021ps^{[29]} \tag{5.2.23}$$

do not add significant error to the final result.

5.2.6 The Ratio f_-/f_+

We use $f_-/f_+ = 0$ in the fit, but this quantity is expected to range from about -0.4 to -1.0.[40−45] We estimate the variation in our final result by refitting the data with $f_-/f_+ = -1.0$. We include the following errors in the final results:

$$\delta(\%)\frac{BR(D^0 \to K^-\mu^+\nu_\mu)}{BR(D^0 \to K^-\pi^+)} = 2.0\% \tag{5.2.24}$$

$$\delta m_{pole} = \pm 0.01 \tag{5.2.25}$$

$$\delta(\%)\frac{BR(D^0 \to K^{*-}\mu^+\nu_\mu)}{BR(D^0 \to K^-\mu^+\nu_\mu)} = 2.0\%. \tag{5.2.26}$$

for the difference between the results for $f_-/f_+ = -1$ and $f_-/f_+ = 0$.

5.2.7 Muon Misidentification

We have shown previously the method by which we estimate the shape and yield of the signal expected from particles misidentified as muons. In the final analysis we apply an additional 10% to the error in the misidentification reweighting term in case we have misrepresented the shape of the misidentification.

We find that the error in the misidentification leads to an error in the final result:

$$\delta(\%)\frac{BR(D^0 \to K^-\mu^+\nu_\mu)}{BR(D^0 \to K^-\pi^+)} = 1.9\% \tag{5.2.27}$$

$$\delta m_{pole} = \pm 0.015 \tag{5.2.28}$$

$$\delta(\%)\frac{BR(D^0 \to K^{*-}\mu^+\nu_\mu)}{BR(D^0 \to K^-\mu^+\nu_\mu)} = 1.9\%. \tag{5.2.29}$$

5.2.8 Muon Identification

One of the chief concerns about the muon system is the difference between data and calibration. In order to get more data for muon calibration, larger counters are used in the Master Gate trigger in place of the TR counters. Timing can change. We know from calibration runs in 1991 that the proportional tubes are sensitive to timing effects. If we look at the distribution of TDC signals from P4 for a run with poor muon performance and compare it to a good run, we can see a shift of 10–15 ns in the distributions and an $\sim 80\%$ loss of efficiency in the proportional tubes. We would like to be confident that this shift in efficiency is not present in the charm data.

To check the timing we look at pion calibration data. This data has tighter trigger requirements and was carefully timed to match the TR counters. We look at the E/P in the HC and IE and compare the distributions with $IDMU = 0$ and $IDMU \neq 0$. We find that $4.3 \pm .8\%(53.5 \pm 10.5$ events) of the total muon signal is exclusively in the $IDMU = 0$ sample. Some of this signal is due to pion decay. To estimate the number of pions that decay into muons we use the sample of $IDMU = 0$ particles in the 50–60 GeV range as representative of the number of incoming pions. We expect roughly 70 of these 10500 pions in the $IDMU = 0$ sample to decay between M1 and the HC, and in the 50–60 GeV range, the muon system detects about $1/3 \pm 1/10$ of the decays. So we expect 46 ± 7 events from decays to be in the HC and not identified as muons. The muon simulation claims the muon identification is 99% efficient for a perfect system at 50–60GeV. We would claim using the pion data that the muon system is $(1 - ((53.5 \pm 10.5) - (46 \pm 7))/(1259 \pm 36) = .99 \pm .01$ efficient. This agrees with the simulation, and since a change in timing is known to effect the identification efficiency by 40% or more, we see no evidence for a timing problem.

The shielding in the muon system in 1991 was modified during the course of the run. We expect a 1.4% change in muon efficiency in 1991 due to uncertainty in the shielding calculation.

There is additional muon efficiency in the system due to noise in the muon system(see Figure 3.8.5). The addition of noise into the Monte Carlo is modelled well, so we add a conservative uncertainty of 1% in the overall efficiency for the 1991 system due to noise and lost planes.

The time dependence of the muon system may not be perfect in 1991. The difference between assessing individual runs and a time dependent Monte

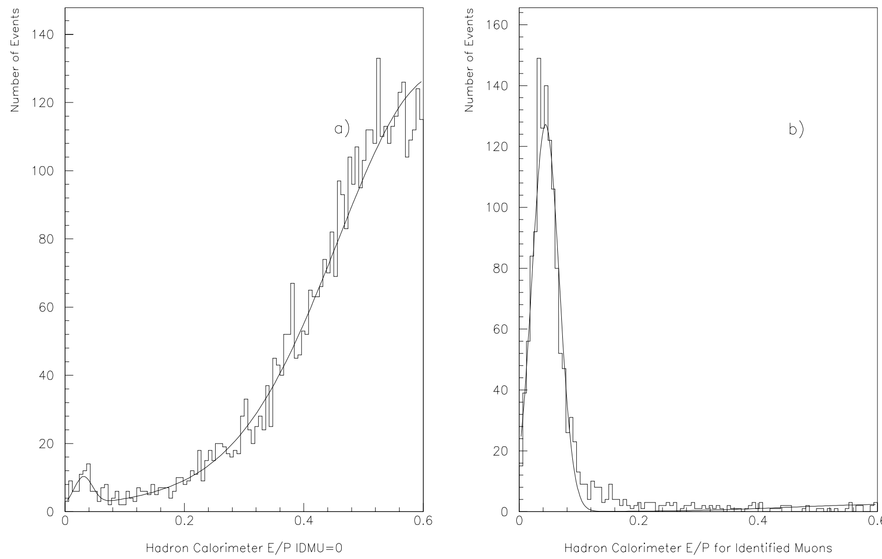

Figure 5.2.1 The E/P response for tracks where a) $IDMU = 0$ and b) $IDMU \neq 0$. The fit used to determine the possible efficiency loss due to timing effects is overlaid as a line.

Carlo was seen to be negligible($\sim 1\%$) and is accounted for by the uncertainty in the shielding calculation and the allowance we made for fluctuations from additional noise or lost planes.

These considerations lead to an overall systematic in the muon identification and simulation of $\sqrt{1.4^2 + 1.0^2} = 1.7\%$ in 1991. We see no evidence for a shift in the 1990 identification or simulation. The final results are expected to fluctuate by

$$\delta(\%)\frac{BR(D^0 \to K^-\mu^+\nu_\mu)}{BR(D^0 \to K^-\pi^+)} = 1.0\% \tag{5.2.30}$$

$$\delta m_{pole} = \pm 0.0 \tag{5.2.31}$$

$$\delta(\%)\frac{BR(D^0 \to K^{*-}\mu^+\nu_\mu)}{BR(D^0 \to K^-\mu^+\nu_\mu)} = 1.0\% \tag{5.2.32}$$

due to uncertainties in the muon system simulation.

5.2.9 Other Backgrounds

We have done a careful job to consider some of the more prominent backgrounds in our signal. Some background can get into the signal via Čerenkov misidentification. Other background may come into the signal from higher multiplicity semileptonic modes.

The Čerenkov misidentified signals from $D^0 \rightarrow K^{*-}\mu^+\nu_\mu$ and from the muon misidentification are already accounted for. Other potential backgrounds can come from $D_s^+ \rightarrow \eta(\eta')\mu^+\nu_\mu$, $D^0(D^+)(D_s^+) \rightarrow \rho^{-,0}\mu^+\nu_\mu$, $D^0 \rightarrow \pi^-\mu^+\nu_\mu$ and $D_s^+ \rightarrow \omega\mu^+\nu_\mu$ to name a few. The rates for these modes are expected to be small, either through production or branching ratios, and the Čerenkov misidentification of a pion as a kaon or kaon/proton is about 2% so a general purpose background representation can be used.

Higher multiplicity modes have been looked for. The PDG lists the following pertinent searches:

Table 5.2.2 Other Higher Multiplicity Semileptonic Modes

Mode	Value	Reference
$\frac{\Gamma(D^+ \rightarrow K^-\pi^+\mu^+\nu_\mu)\ nonresonant}{\Gamma(D^+ \rightarrow K^-\pi+\mu^+\nu_\mu)}$	$< 0.12(90\% C.L.)$	[32]
$\frac{\Gamma(D^+ \rightarrow K^-\pi^+\pi^0\mu^+\nu_\mu)}{\Gamma(D^+ \rightarrow K^-\pi+\mu^+\nu_\mu)}$	$< 0.042(90\% C.L.)$	[32]
$\frac{\Gamma(D^+ \rightarrow (\overline{K}^*\pi)^0 e^+\nu_e)}{\Gamma_{total}}$	$< 0.012(90\% C.L.)$	[47]
$\frac{BR(D^0 \rightarrow K^-\pi^+\pi^-\mu^+\nu_\mu)}{BR(D^0 \rightarrow K^-\mu^+\nu_\mu)}$	$< 0.037(90\% C.L.)$	[48]
$\frac{BR(D^0 \rightarrow (K^*\pi)^-\mu^+\nu_\mu)}{BR(D^0 \rightarrow K^-\mu^+\nu_\mu)}$	$< 0.043(90\% C.L.)$	[48]

Of these modes, the $D^+ \rightarrow K^-\pi^+\mu^+\nu_\mu$ *nonresonant* has the most potential to be a significant background. Since the muon simulation was not prepared for the 1991 data in time for the analysis of $D^+ \rightarrow K^-\pi^+\mu^+\nu_\mu$

nonresonant, a more careful analysis using the present simulation for this analysis can be done to determine whether the non–resonant signal is really misidentified $D^+ \to K^-\pi^+\pi^+X$.

The CLEO collaboration[23] made a measurement of the total leptonic rate. They found that the sum of Cabibbo–favored pseudoscalar and vector decays , $(D \to [K+K^*]e\nu) = (14.8 \pm 1.3) \times 10^{10}s^{-1}$ saturates the inclusive rate , $(D \to eX) = (16.7 \pm 1.5) \times 10^{10}s^{-1}$. Following a recent review,[49] we add an additional 8% of the sum of Cabibbo–favored pseudoscalar and vector decays for the expected rate of Cabibbo–suppressed decays, and we find a deficit of 0.9 ± 2.0 which is consistent within errors to no additional decays.

We choose to model any unaccounted for background with events that come from wrong–sign misidentified signal for the analysis with the D^* tag and events where $Q(K) = Q(\mu)$ for the analysis where no D^* tag is used.

To account for the systematic contribution to the final result we allow the background to vary in the fit. Typically, the error on the background yield is the order of the background yield and is small. Roughly 2% of the total $K\mu$ signal is accounted for by the background term, and this is consistent with the expectation that any additional semileptonic contribution is small.

5.2.10 Monte Carlo Statistics

We generate an order of magnitude more Monte Carlo events than we see in the data. The final results are expected to change by:

$$\delta RESULT = \sigma(RESULT)\sqrt{1.0 + 0.1^2} \tag{5.2.33}$$

due to Monte Carlo statistics.

5.3 Checks Using the Data

We know that conditions change in an experiment like E687. Chambers lose efficiency, targets or detectors are moved to increase their efficiencies, beams are tuned to give optimal performance and whole detectors may be replaced. We correct for changes in the experiment by assigning run periods to our simulation based on our knowledge of physical changes to the experiment. Likewise, we assess intangible error associated with the simulation by comparing it to our analyzed data.

To make a quantitative check of the simulation, we compare reconstructed quantities with the results of our fit and look for trends that indicate a shift in our result. If a trend is seen, we need to determine the effect on the final result.

In addition to drawing on other E687 analyses, we would like to check a variety of reconstructed quantities. The following sections will describe checks on vertexing, lifetimes, mass dependence, momentum dependence, triggering and different analysis techniques. The main motivation for each test will be mentioned.

We will demonstrate that systematic errors can cancel in ratio to another mode, illustrating the allure of doing a branching ratio measurement.

5.3.1 Experience from Other Analyses

The Monte Carlo simulation has been tested for consistency using measurements from other experiments.[50] In short, we measure the ratio of branching ratios $\frac{BR(D^0 \to K^- \pi^+ \pi^+ \pi^-)}{BR(D^0 \to K^- \pi^+)}$ and assign a per track correction to the efficiency. We find the correction to be $3 \pm 3\%$ per track for modes of *different* multiplicities. When we take modes of the same multiplicity in ratio, this error largely disappears. The study covers effects from the Čerenkov system, the triggers, the PWC system, hadronic absorption, multiple scattering, vertex detector efficiency, linking considerations, acceptance(apertures), vertex fit confidence levels, resolution effects and different running periods.

5.3.2 l/σ

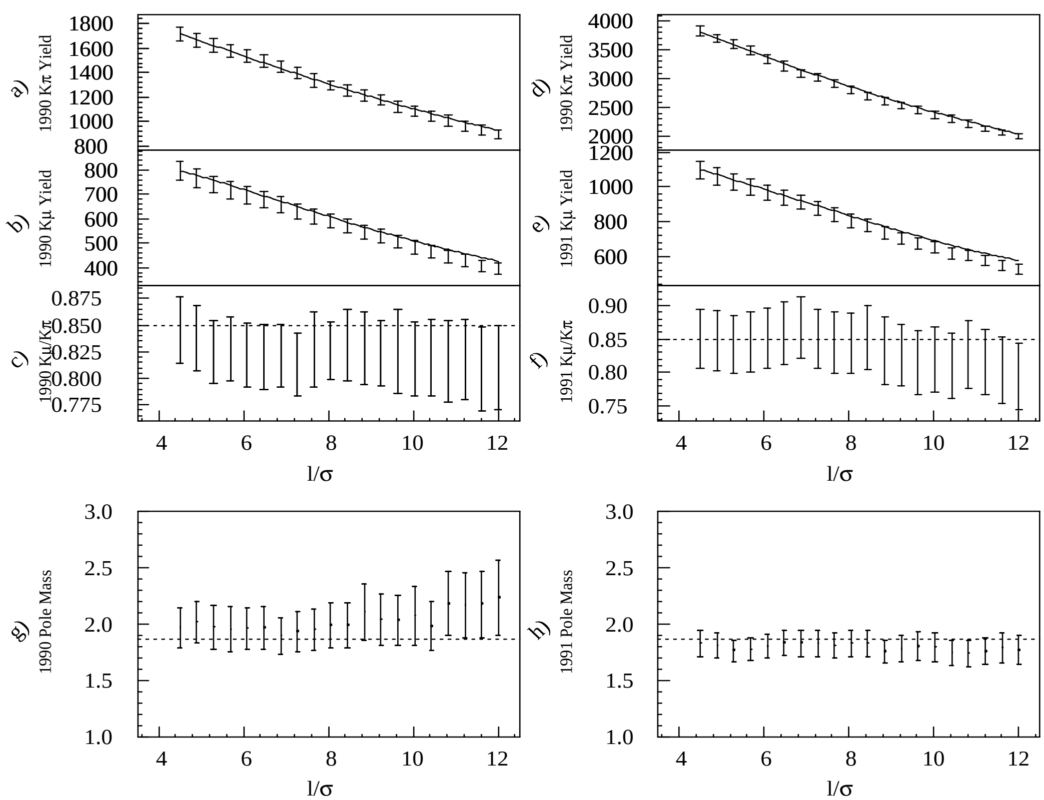

Figure 5.3.1 The l/σ behavior for a), the 1990 $K^-\pi^+$ yield, b), the 1990 $K^-\mu^+$ yield, c), the 1990 ratio of $K^-\mu^+$ and $K^-\pi^+$, d) the 1991 $K^-\pi^+$ yield, e), the 1991 $K^-\mu^+$ yield, f), the 1991 ratio of $K^-\mu^+$ and $K^-\pi^+$, g), the 1990 M_{pole} measurement and h), the 1991 M_{pole} measurement. The solid lines in a), b), d) and e) are the expected behavior of the yields from the simulation. The dashed lines in c), f), g) and h) are the final results using the entire sample.

We study the significance of separation(l/σ) of the secondary vertex from the primary vertex as a check on backgrounds and resolution. If a particle decayed at the secondary vertex location, we gain insight into the particle lifetime by measuring the distance between the primary and secondary vertex and the momenta of the secondaries. We can use the lifetime to discriminate against signals with different lifetimes. When we calculate the error on the separation, we need to predict the momentum dependent resolution of the microvertex detector, and we are predicting the quality of the vertex based on the opening angle of the tracks in that vertex. We can use the predicted error to discriminate against unreasonable vertices. Combining these two measures gives us a broad check of our signal and simulation.

If we see a problem in the l/σ behavior of the branching ratio measurement, we look at the behavior of the individual signals in the branching ratio to determine whether the problem is universal or plagues just one mode. If we see a problem in the m_{pole} measurement, we might doubt both our resolution model and representation of the components in the $K^-\mu^+$ signal.

We show the l/σ behavior of the branching ratio, the individual yields and m_{pole} for the 1990 and 1991 data samples in Figure 5.3.1. Agreement is good for the 1990 branching ratio and the 1991 branching ratio. The pole mass agreement is good as well. We can now look at other reconstructed quantities to see if other trends exist.

5.3.3 $\underline{M(K\mu)}$

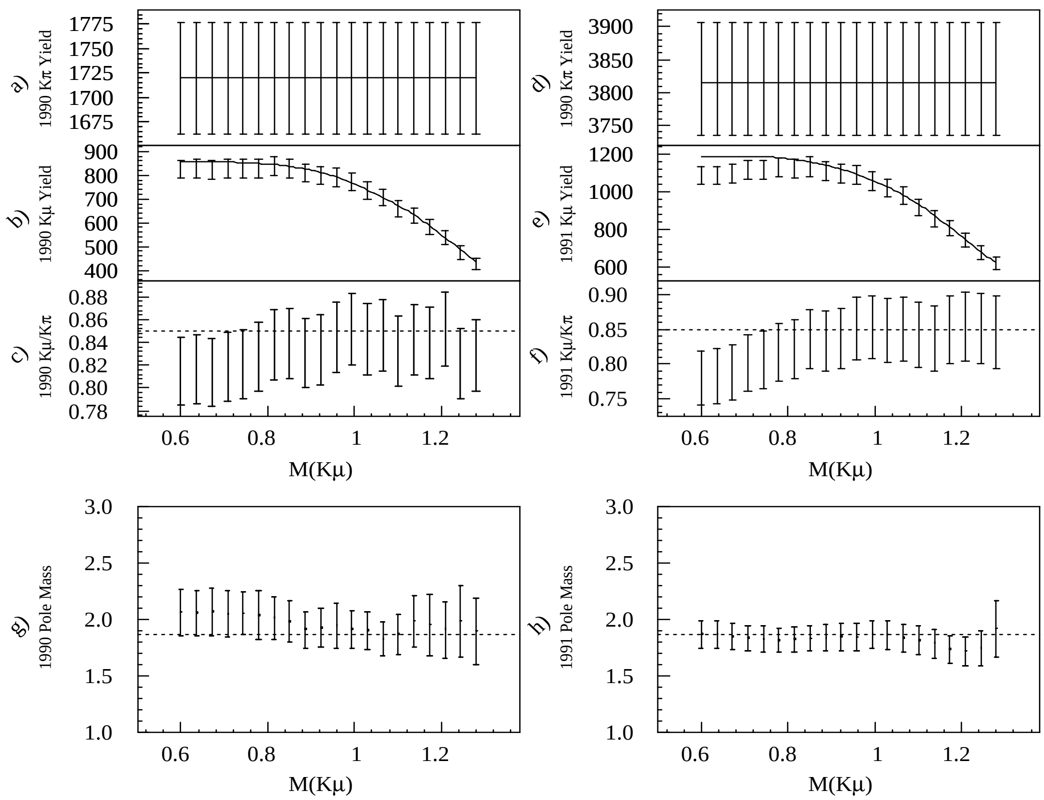

Figure 5.3.2 The $K^-\mu^+$ mass behavior. Labels are as for Figure 5.3.1. Not the stability of the result for $M(K\mu) > 0.8\ GeV/c^2$ indicating that our cut at $M(K\mu) = 0.95\ GeV/c^2$ is conservative.

Studying the $K^-\mu^+$ mass can tell us whether there is a resolution effect that depends on the opening angle, or there are significant backgrounds that we have missed. There is no cancelling systematic check in the $K^-\pi^+$ analysis so this study is a stringent test of our $K^-\mu^+$ simulation.

We see in Figure 5.3.2 that all signals are well behaved above $M(K\mu) = 0.8\ GeV/c^2$ for this study and we expect no systematic error from the $K^-\mu^+$ mass variation since we cut the signal at $M(K\mu) = 0.95\ GeV/c^2$ to reduce the influence of background fluctuations, additional semileptonic modes, and variations from $D \to K^* \mu \nu$ contamination(see Figure 4.6.1). In other words, the systematic error expected by relaxing the cut exceeds the variation we see in Figure 5.3.2 and reduces the precision of our result.

5.3.4 *DCL*

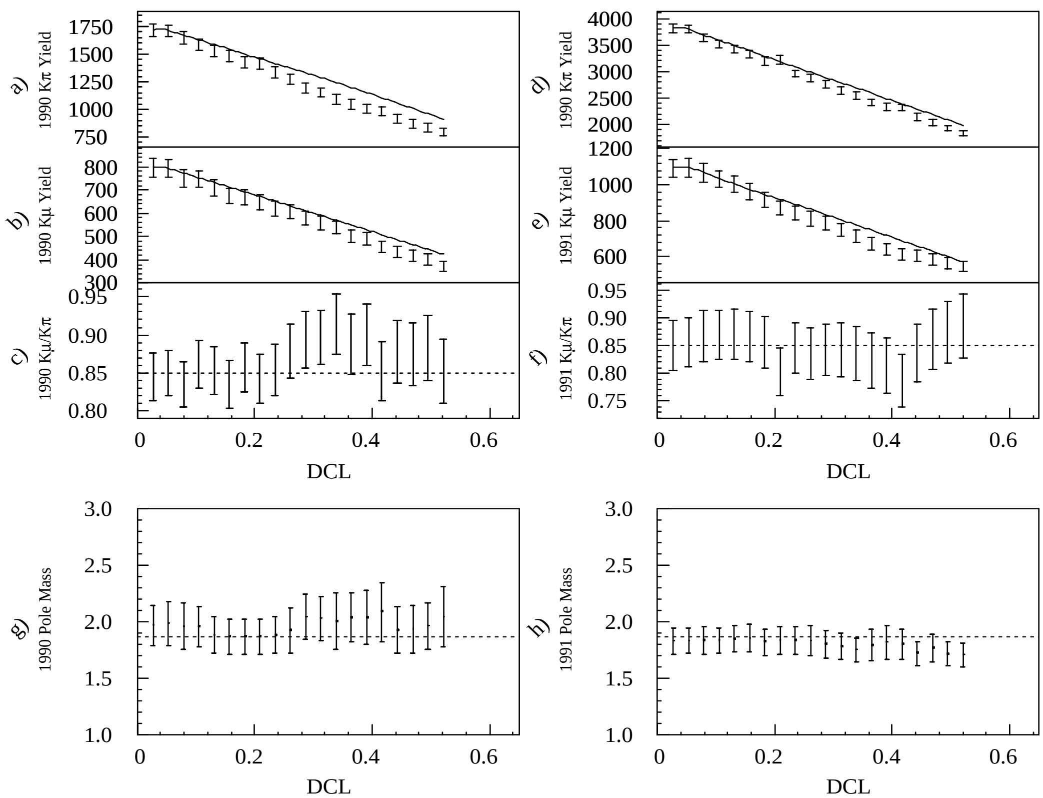

Figure 5.3.3 *DCL* mass behavior. Labels are as for Figure 5.3.1.

The Daughter Confidence Level(DCL) is a check on the quality of the secondary vertex. Vertex quality can change due to background in the signal or an aspect of the reconstruction that we have not modelled correctly.

We show the results of this study in Figure 5.3.3. The agreement between data and Monte Carlo is poor for the yield measurements, but good for the m_{pole} measurement. The shift in the yield measurement is cancelled in the ratio thus demonstrating the utility of a normalizing mode and indicating that the shift is probably due to reconstruction differences rather than background effects. One cause for this effect is the microvertex track fitter.[51] We do not arbitrate against exceedingly poor hits, and we include these hits in subsequent calculations. The overall effect in resolution is small, but a shift in confidence levels would result.

5.3.5 $\underline{P(K)}$

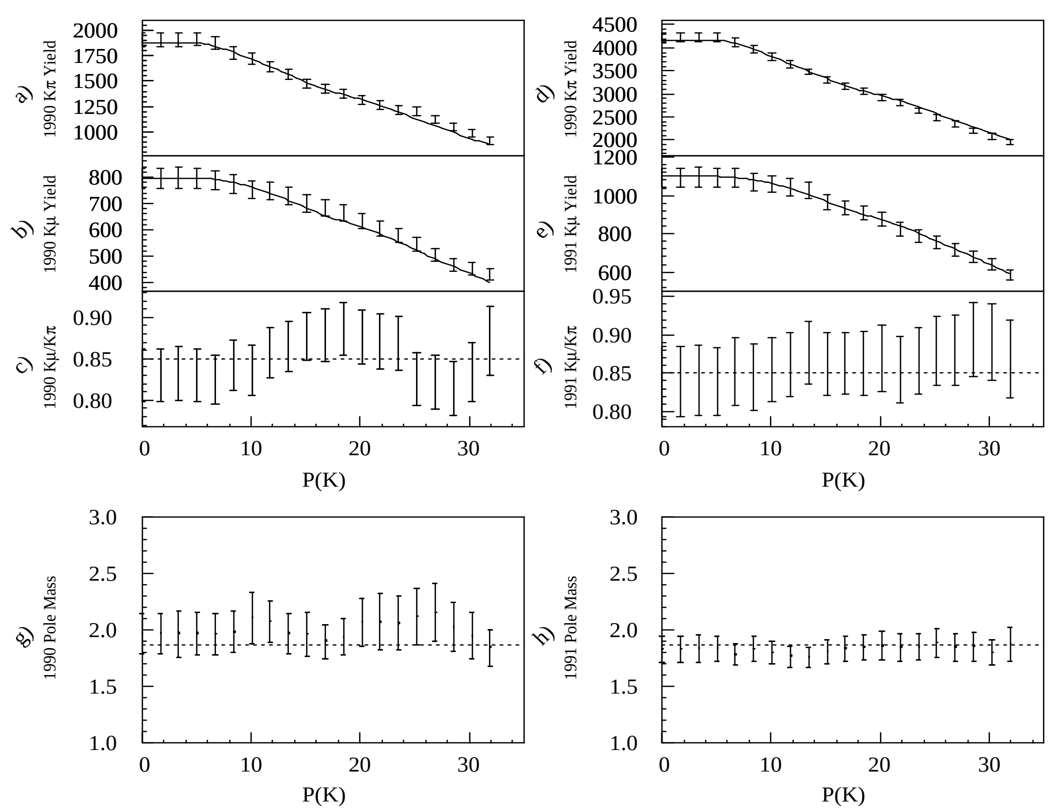

Figure 5.3.4 The K^- momentum behavior. Labels are as for Figure 5.3.1.

We indirectly test the generated charm momentum, the hadronic trigger simulation and the acceptance of the experiment by looking at the reconstructed kaon momentum.

We see good agreement in this cut variable for the ratio and the pole mass, justifying our 10 GeV/c cut in the $D^0 \to K^-\pi^+$ analysis, and demonstrating the ability of the normalization mode to correct systematic effects again.

5.3.6 $\underline{P(\mu(\pi))}$

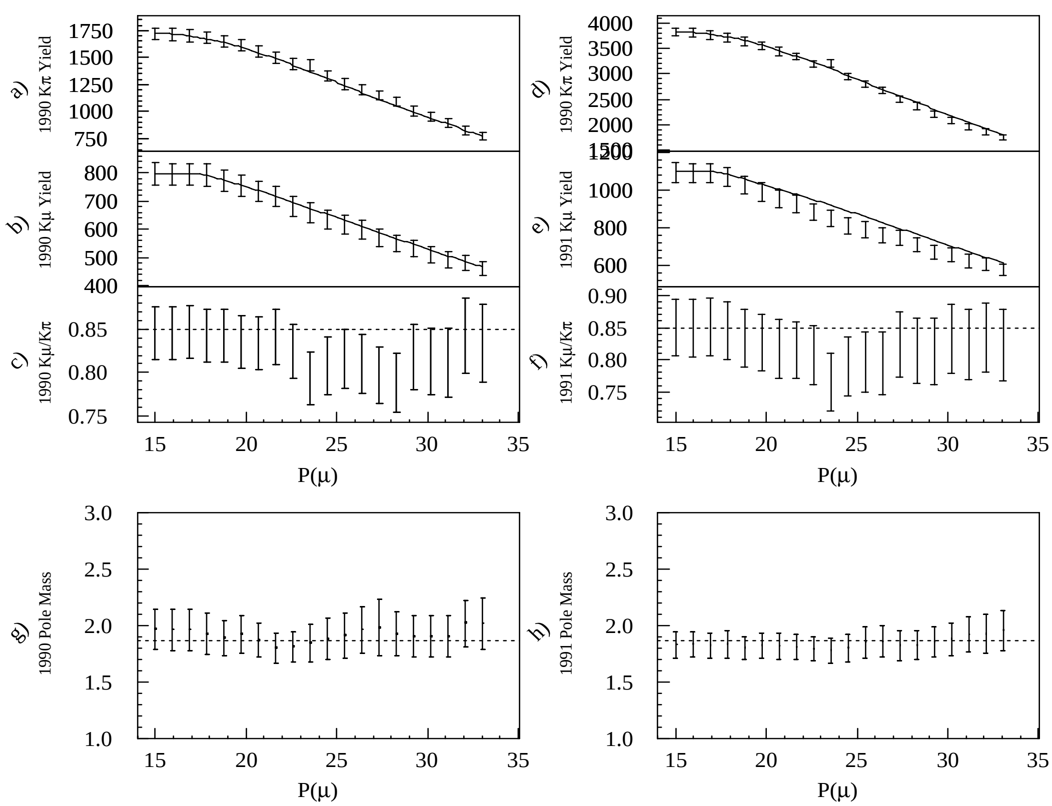

Figure 5.3.5 The μ^+ momentum behavior. Labels are as for Figure 5.3.1.

Here we are essentially checking the muon system and the generated charm momentum again. We demonstrate that the muon momentum is fairly insensitive to the hadronic trigger in Figure 5.3.6. This test compliments the previous test of $P(K)$ since we have a separate test of the generated charm momentum, and we can tell if a problem here is related to the muon simulation, or the hadronic trigger.

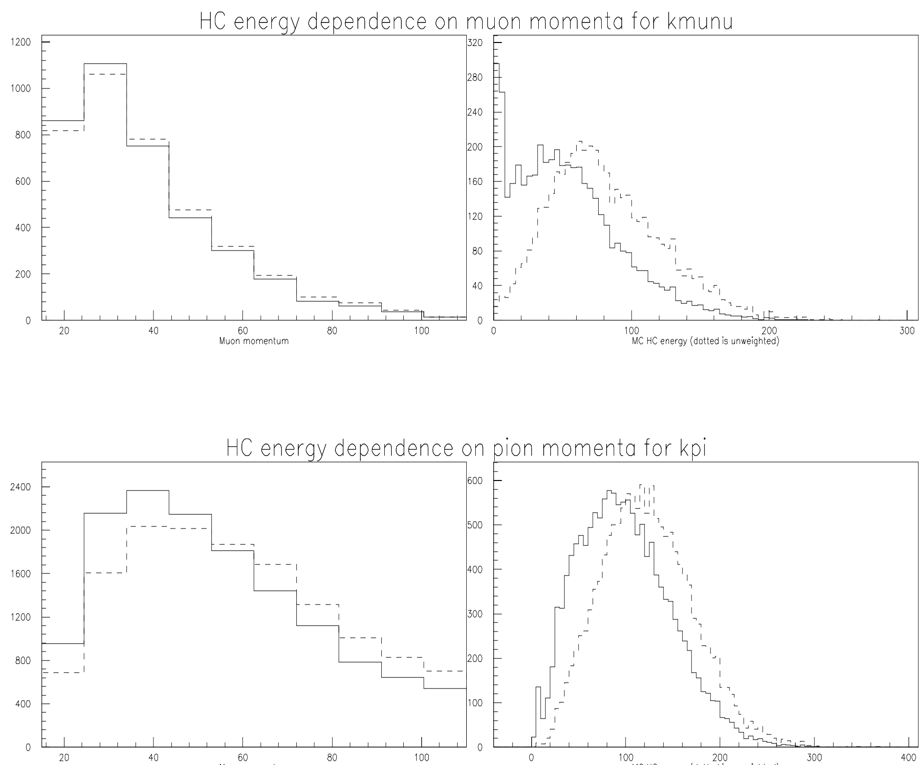

Figure 5.3.6 The variation of the μ^+ and π^+ for a drastic change in the hadronic trigger. The simulated response before the reweighting is performed is overlaid as a dotted line. Note that the μ^+ momentum behavior is invariant compared to the π^+ behavior for this test.

We see no trend in the 1991 branching ratio or the 1990 branching ratio. Agreement for the pole mass is fine as well.

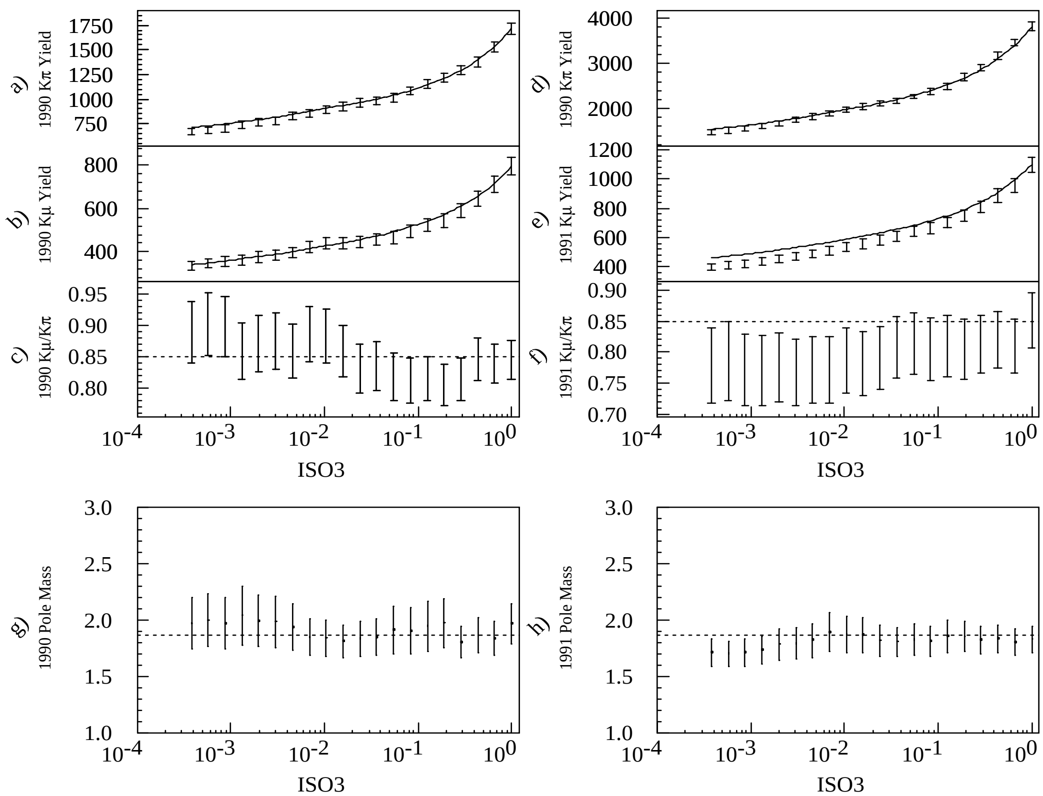

Figure 5.3.7 *ISO*3 behavior. Labels are as for Figure 5.3.1.

5.3.7 *ISO3*

Finally, we want to test our earlier contention that semileptonic modes of higher multiplicities are not a significant source of contamination. We are looking at the behavior of the signal using a more stringent isolation cut(ISO3). The method is to isolate the $K^-\mu^+$ and $K^-\pi^+$ vertex from *all* other microstrip tracks in the event(the soft pion is an exception in the D^* analysis).

Agreement as shown in Figure 5.3.7 is fair, but since the trends are opposite in 1990 and 1991, we can use this test, the yield of the added background, the published limits and the CLEO[23] inclusive result to be confident that we are not missing a large source of higher multiplicity semileptonic contamination in our signal. Subsequent studies using the high D^0 momentum solution confirm that the trend seen here is statistical in nature.

5.4 Checks of the Fit

In this section we show that the representation we use for the data is a good one and that we have properly taken care of effects such as resolution smearing properly. In cases where we have a discrepancy, we assign an additional error to the final result.

We check bin sizes, the high D momenta solution, the D^* analysis compared to the analysis without using the D^*, errors returned by the fitter, goodness of the fit and finally we use a different fitting technique that incorporates some of the systematic error in estimating the final result.

5.4.1 Information, Resolution and Bin Size

As mentioned previously, we need to make sure that we have generated enough Monte Carlo to properly map out the transform between generated space and reconstructed space. We can also check our fit to make sure it is varying smoothly with bin size.

Suppose the feature we are trying to fit is a straight line or level with no slope. We need not bin the histogram to get a reasonable answer. Now suppose we are trying to fit a slope. We need at least 2 bins in our histogram. As we bin the histogram in finer and finer bins, features that may or may not be related to statistical fluctuations appear. If we generate our histogram by binning a random number, we expect that the features are statistical in nature. If we are generating a mass peak, we hope that a peak will continue to appear as we go to finer bins. If we were generating a mass peak, but our histogram just covers the inner peak area, finner binning will not significantly add to the information from coarser bins. Thus, by checking bin size we can test whether we get significantly more information as we go to finer binning.

We expect that the resolution in q^2 will limit the utility of decreasing bin size for the m_{pole} measurement as the change across the q^2 plot is gradual and the resolution in q^2 is large. By contrast, we might expect that finer bins will let us discriminate between signal and background for the yield measurement as each component has features that vary in both q^2 and E_μ.

What we find is that decreasing bin size has a positive effect on the pole mass measurement and can give us more discriminating power in the yield measurement as well. We also find that the fit error is essentially stable after 35 bins in q^2 and E_μ with little benefit in going to smaller bin sizes. The stability of the yield and pole mass with decreasing bin size also indicates that we have generated sufficient events to map out our transform. Figure 5.4.1 is a summary of these results.

5.4.2 High P_D Solution

Another test of resolution or bias in our measurement is to use the high momentum solution for the D^0. Because of resolution effects, this solution is often redundant with the other solution, but we can check again to see whether we have manufactured a result. We combine this test with the results from the tag analysis in the section "Combining the Sources of Systematic Error." We compare the final results of the high momentum solution to the tag analysis and the low momentum solution in the next section.

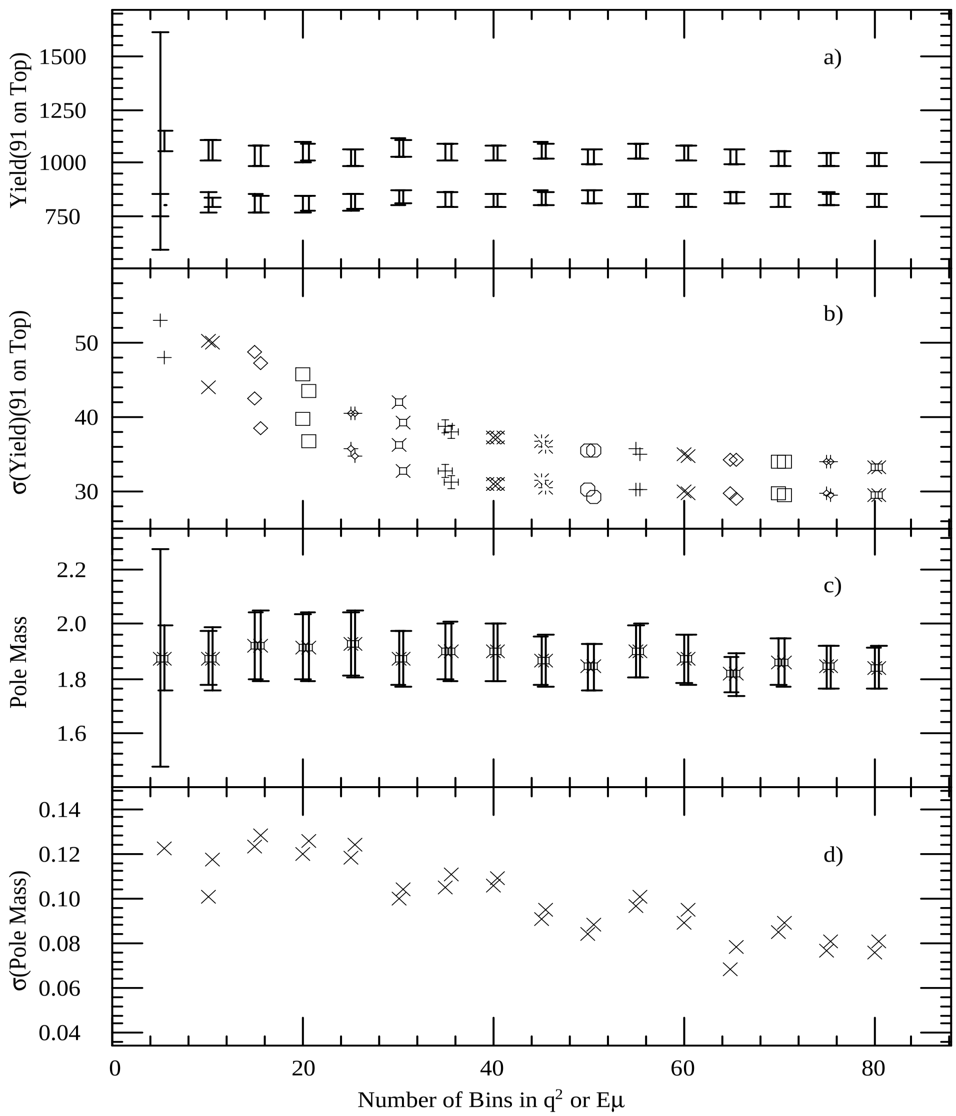

Figure 5.4.1 Bin choice behavior. The upper error bars in a) represent the fit to the 1991 data set for error calculated by two different techniques, the lower error bars represent fits to the 1990 data. The symbols in b) are the magnitude of the error bars in a)(upper symbols are 1991 again). The points and error bars in c) represent the average pole mass for 1990 and 1991 data with the error calculated two different ways. The points in d) represent the magnitude of the error bars in c). Note the decrease in the error with only small shifts in the final result as the number of bins is increased.

5.4.3 The D^* and Non–D^* Analyses

The D^* analysis has much better signal to noise than the non-tag analysis. By comparing the two analyses we can see if the results are consistent.

The results from the systematic studies and from analyzing the high D^0 momentum solution are summarized in Table 5.4.1.

Table 5.4.1 Comparison of Techniques, $D*$ and Non–$D*$ Analyses

Measurement	$D*$	Non–$D*$ Low P	Non–$D*$ High P
$\frac{BR(D^0 \to K^- \mu^+ \nu_\mu)}{BR(D^0 \to K^- \pi^+)}$	$0.84 \pm 0.08 \pm 0.03$	$0.852 \pm 0.034 \pm 0.028$	$0.845 \pm 0.034 \pm 0.029$
m_{pole} GeV/c^2	$2.01^{+0.32+0.09}_{-0.18-0.10}$	$1.87^{+0.11+0.07}_{-0.08-0.06}$	$1.84^{+0.10+0.16}_{-0.08-0.09}$

We find that all the results are consistent. We choose to include the differences as variations in the fit technique rather than an actual systematic shift in the simulation of the experiment. We evaluate actual shifts in the simulation in the section "Combining the Sources of Systematic Error." The source of the additional systematic error for the high D^0 momentum solution pole mass estimate is explained in the section "Information and D^0 Momentum Solution Choice."

5.4.4 Mini Monte Carlo

If we used a function to fit the data, it would be a simple task to take the final results of our fit and generate many ensembles of the fit function as if we are generating lots of Monte Carlo. The idea is to fit the separate generated data sets and see if the median value and spread in the returned results matches those returned by the fitter for the data. We can also look at the spread of likelihoods to see if the likelihood returned by the fit to the data is reasonable.

In practice, it is an easy task to Poisson fluctuate the number of events in a given histogram bin of the fit histogram and use the fluctuated histograms to test the fit. We cannot assess goodness of fit in this way since the fit and data histograms are correlated. To test goodness of fit, we need to develop a functional form of the fit histogram and generate a separate fit histogram and data histograms. We can then compare the results of our completely synthetic data sets to our fit histogram fluctuated ones.

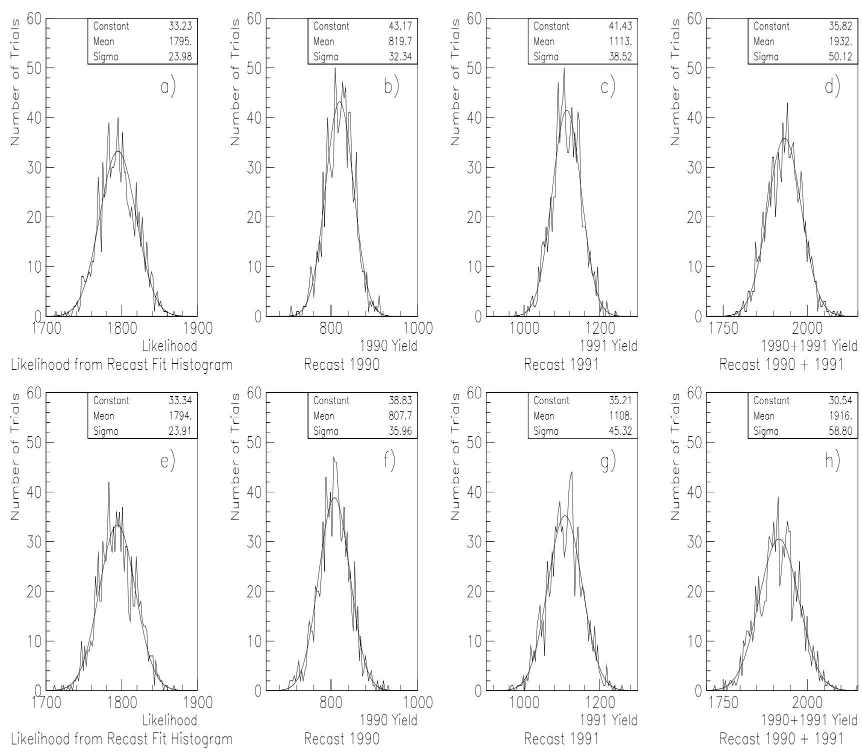

Figure 5.4.2 Expected centroid and spread of the yield estimate returned by the fit for a Poisson fluctuated fit histogram. The standard fit is represented by plots a)–d), and the fit which includes systematic error directly in the fit is represented by plots e)–h). Note that the spread of likelihoods is the same for each test and that no correlation between results is indicated. A correlation between parameters is expected if the spreads in the individual yields do not translate to the spread of the addition of the individual yields.

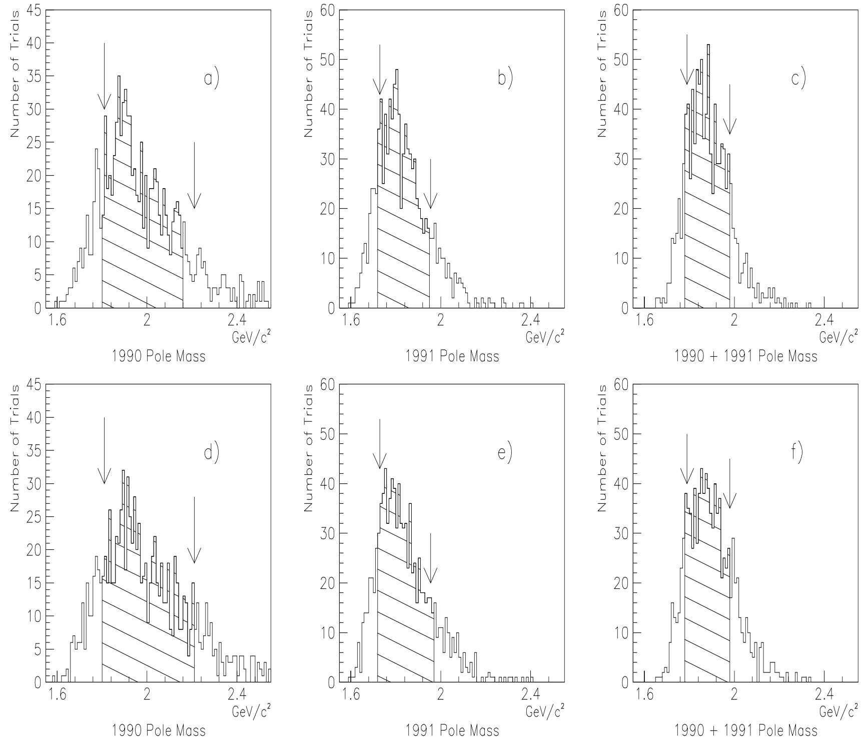

Figure 5.4.3 Expected centroid and spread of M_{pole} returned by the fit for a Poisson fluctuated fit histogram. The fit results for the standard fit, a)–c), and the fit which includes systematic error directly in the fit, d)–f) are shown. The striped portions of the histograms contain the middle 68.3%($\pm 1\sigma$) potion of the distribution, and the arrows represent the 1σ error bounds returned by the fit. The 1σ errors are well reproduced in both c) and f).

In Figures 5.4.2 and 5.4.3 we see the results of the bin fluctuated test. The comparison between the yield results of the fit to the data and the fit histogram fluctuated test can be found in Table 5.4.2. The numbers in parentheses represent an alternate fit technique that incorporates sources of systematic error in the fit(see the section "Alternate Fit Method"). The agreement between the M_{pole} results is good as seen in Figure 5.4.3.

The test shows us that the fit delivers errors that tend to be conservative for the yield using the alternate fit technique. The increase in the error is possibly due to resolution effects not handled in the Monte Carlo(explained shortly) but is more likely due to correlations between any of the 10 parameters used in the fit that are not simulated with this simple model, so we choose to quote the more conservative error. If we look at the spread of returned errors rather than the spread of returned parameters (see Table 5.4.3), we confirm that there is an increase in the error due to correlations with the other parameters used in the fit, and we are satisfied that we get an estimate of the influence of other parameters used in the fit on the final result.

Table 5.4.2 Comparison of Fit and Fluctuated Fit Histogram Trials

Measurement	Fit	σFit	Fluctuated Centroid	Fluctuated Spread
Yield(1990)	819(797)	$\pm$31(39)	820(808)	$\pm$32(36)
Yield(1991)	1112(1099)	$\pm$39(50)	1113(1108)	$\pm$39(45)

Table 5.4.3 Comparison of Fit and Fluctuated Fit Histogram Errors

Measurement	σFit	Fluctuated Error Centroid
Yield(1990)	$\pm$31(39)	$\pm$33(39)
Yield(1991)	$\pm$39(50)	$\pm$41(50)

Figure 5.4.4 is the displayed results of the synthetic generator. The salient features of the plot are the shift in the likelihood centroid for the uncorrelated ensembles relative to the correlated ones, the agreement in the spread and centroid of the return parameters for the two tests and the likelihood of our fit to the data compared to the centroid and spread of the uncorrelated ensembles test.

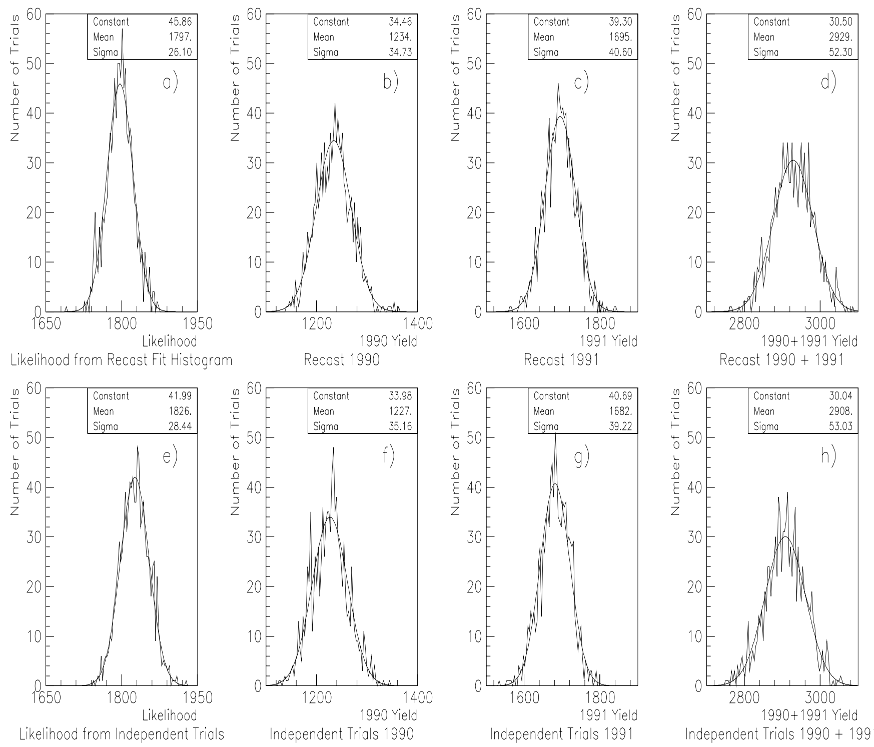

Figure 5.4.4 The results of the synthetic data sets fit. Notice that the spreads in the parameters remain unchanged as we change from the Poisson fluctuated method to the independent trials method. Also note the increase in the centroid of the likelihood spread as we use the independent trials method.

Roughly 99.5% of the spread in the uncorrelated ensemble test lies below our result for the fit to the data. This estimate is made on the assumption that there is no resolution mismatch between data and Monte Carlo. We have seen that qualitative agreement is good between data and Monte Carlo(Figure 5.1.4), but there is evidence for resolution mismatch in our DCL test(Figure 5.3.3). If we introduce additional fluctuations or a shift in our synthetic data set generator, the centroid of the likelihood increases, the errors increase slightly and our confidence level increases.

To test this hypothesis, we compare the σ's returned from a Gaussian fit to the distributions in Figure 5.1.4. We find that the difference between data and Monte Carlo is $5 \pm 2\%$. A 5% added fluctuation to q^2 and a 5% added fluctuation to E_μ(q^2 and E_μ fluctuations are handled completely independently) increases the centroid of the synthetic likelihoods from 1826 to 1843, increases the spread(σ) of likelihoods from 28.44 to 29.8, increases the 1991 yield sigma from 38 to 42 and leaves the 1990 yield sigma invariant. Since our fit to the data returns a likelihood of 1900, roughly 97% of the synthetic likelihoods lies below our signal with this estimate of resolution effects. This indicates that the 0.5% confidence level found using the unfluctuated data sets is an acceptable one for our fit.

To make sure that we are not biasing the assessment of the fit a separate goodness of fit test is performed. We sum bins in the data histogram together until the bin population is sufficient, sufficient being at least 10 events, to perform a simple χ^2 test. Each group of summed bins is considered a degree of freedom, and we can calculate a confidence level for the fit. Several different summing schemes were tried to remove the possible bias from a single method.

Studying the results in Figure 5.4.5 gives us a feel for the validity of this test. One can see that for some cuts the confidence level is low; other cuts have spreads over the whole range of confidence level indicating that our fit is reasonable. The spread in confidence levels for the final fit result is grouped below 50% but is an acceptable representation of the data by the fit histogram. This test is a direct test using the data and the fit information and does not rely on a synthetic representation of the data.

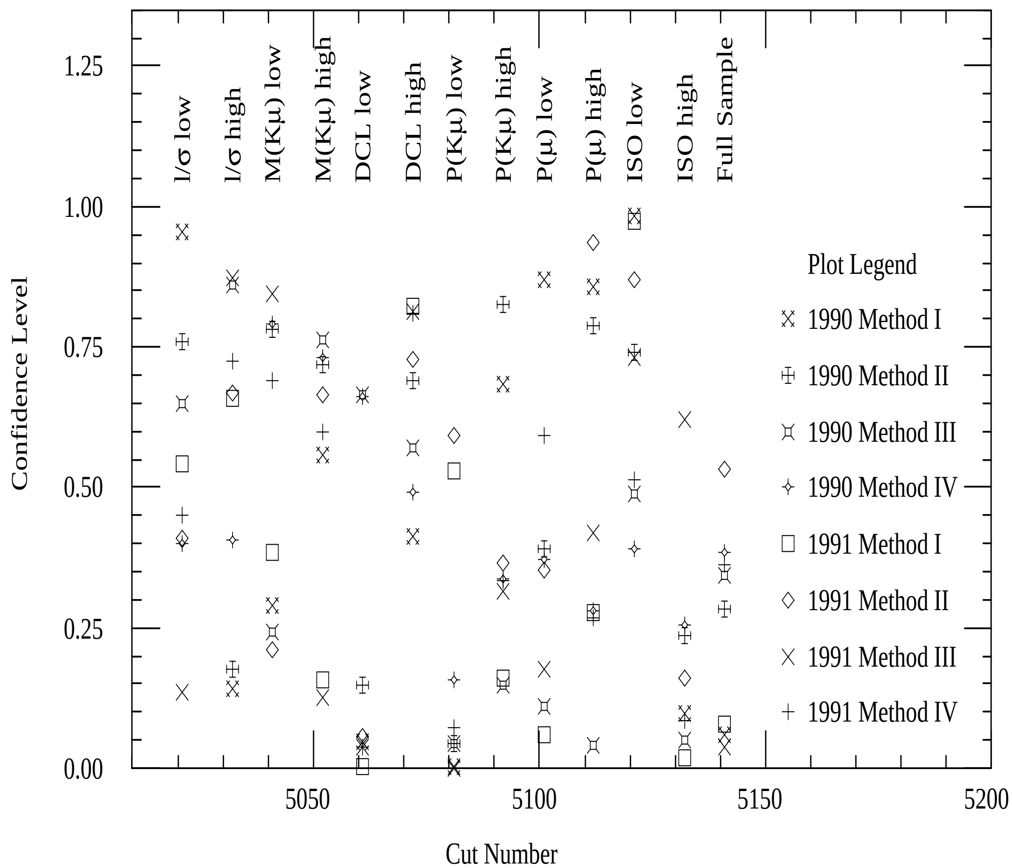

Figure 5.4.5 Pseudo χ^2 test. Bins with low populations are grouped together to form groups. Each group is then a degree of freedom, and a simple χ^2 test is performed(see text). Each grouping method is shown as a different symbol.

5.4.5 Alternate Fit Method

The previous sections should convince us that the study of systematic error is tedious and demanding. If there was a way to include some of our systematic error automatically in our fit, we could do more fits in a shorter time. By including uncertainty in the fit from systematic sources, we also have a check on the statistical validity of our previous result. Is the minimum of the negative log likelihood real or have we somehow manufactured it by the quantities we input into the fit function?

On a suggestion from Jim Wiss,[52] we include some systematic quantities in the fit itself to test our assessment of systematic errors and give us confidence that we are really seeing a signal. In essence, the likelihood changes from:

$$\mathcal{L} = \prod_{bins_i} \frac{n_i^{s_i} e^{-n_i}}{s_i!} = P(s,n) \tag{5.4.1}$$

to

$$\begin{aligned} \mathcal{L} = P(s,n)exp(-.5\left(\frac{MISID - MISID_{expected}}{\sigma_{MISID_{expected}}}\right)^2) \\ \prod_{j=1}^{3} exp(-.5\left(\frac{f_j - f_{expected}}{\sigma_{expected}}\right)^2) \end{aligned} \tag{5.4.2}$$

where we vary $MISID$ and the measured values used to estimate the fraction of each semileptonic background f_j around the expected values weighting with the error on the expected values. Since the muon misidentification representation is not shared between 1990 and 1991, we again put in separate terms for $MISID$ in 1990 and 1991.

The statistical error returned by the fit should be a sum in quadrature of the systematic error from $MISID$ and the f_j's. We find that this method faithfully reproduces the values we found by putting $MISID$ and the f_j's shifts in by hand. The results of the test can be found in Table 5.4.4. There is further justification for keeping our conservative errors returned by the fit as compared to the synthetic error determination, and we avoid folding in variations due to the fitting procedure for each fit used to determine the systematic error in the standard procedure.

Table 5.4.4 Alternate Fit Method Compared to Old Method

Quantity	New Fit Value	Old Fit Value
$\frac{BR(D^0 \to K^- \mu^+ \nu_\mu)}{BR(D^0 \to K^- \pi^+)}$	0.852	0.867
$\delta_{statistical}\ \frac{BR(D^0 \to K^- \mu^+ \nu_\mu)}{BR(D^0 \to K^- \pi^+)}$	0.034	0.029
$\delta_{systematic}\ \frac{BR(D^0 \to K^- \mu^+ \nu_\mu)}{BR(D^0 \to K^- \pi^+)}$	0.000	0.022
$\sqrt{\delta^2_{sys.} + \delta^2_{stat.}}$	0.034	0.036
m_{pole}	1.87	1.86
$\delta_{statistical} m_{pole}$	$^{+0.11}_{-0.08}$	$^{+0.10}_{-0.08}$
$\delta_{systematic} m_{pole}$	0.0	± 0.04
$\sqrt{\delta^2_{sys.} + \delta^2_{stat.}}$	$^{+0.11}_{-0.08}$	$^{+0.11}_{-0.09}$

The convenience of this method cannot be overstated. We use this fit for the systematic studies using the split samples approach. This method for determining systematic error due to variations in our representation of the data is explained in the next section.

5.5 Combining the Sources of Systematic Error

We have located the sources of systematic error and wish to combine them. To use the qualitative tests of the data, we take the data used for the tests in "Checks Using the Data" and form the results into statistically separate samples. Figures 5.5.1– 5.5.6 are plots of the results of fits to these samples and Table 5.5.1 lists the cuts used to make each sample.

Table 5.5.1 Split Sample Criteria

Samples(4)	Requirements
l/σ	1990(1991) $l/\sigma < 12$, 1990(1991) $l/\sigma \geq 12$
$M(K\mu)$ GeV/c^2	1990(1991) $M(K\mu) < 1.28$, 1990(1991) $M(K\mu) \geq 1.28$
DCL	1990(1991) $DCL < 0.52$, 1990(1991) $DCL \geq 0.52$
$P(K)$ GeV/c	1990(1991) $P(K) < 32$, 1990(1991) $P(K) \geq 32$
$P(\mu)$ GeV/c	1990(1991) $P(\mu) < 33$, 1990(1991) $P(\mu) \geq 33$
$ISO3$	1990(1991) $ISO3 < 0.01$, 1990(1991) $ISO3 \geq 0.01$

We assess any additional error using the method[53] outlined in "Techniques for the Resonance Analysis of Three Body D Meson Decays". Briefly, we take the N statistically independent results r_N and find the error indicated by the expression:

$$\sigma_{extra} = \sqrt{\frac{< r^2 > - < r >^2}{N-1}} \tag{5.5.1}$$

where

$$< r >= \frac{\sum_{i=1}^{N} r_i/\sigma_i^2}{\sum_{i=1}^{N} 1/\sigma_i^2} \tag{5.5.2}$$

and

$$\sigma_r = \sqrt{\frac{1}{\sum_{i=1}^{N} 1/\sigma_i^2}}^{\,-1}. \tag{5.5.3}$$

If $\sigma_{extra} > \sigma_r$ we say that $\sigma_{sys} = \sqrt{\sigma_{extra}^2 - \sigma_r^2}$, and if $\sigma_{extra} < \sigma_r$ we say that $\sigma_{sys} = 0$.

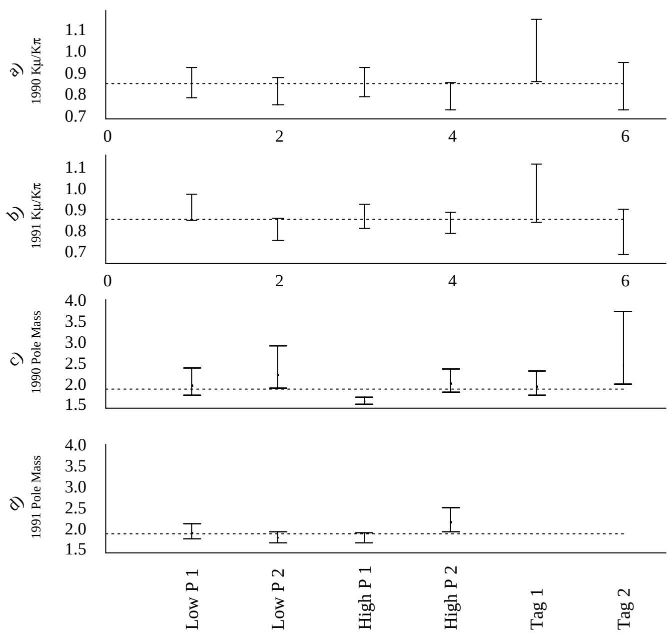

Figure 5.5.1 The split samples in l/σ used for the systematic analysis. The branching ratio variations are shown for each(P1 and P2) l/σ sample in a) for the 1990 low D^0 momentum solution, the 1990 high D^0 momentum and the 1990 tag analysis and b) for the 1991 low D^0 momentum solution, the 1991 high D^0 momentum and the 1991 tag analysis. The pole mass variations are shown for each(P1 and P2) l/σ sample in c) for the 1990 low D^0 momentum solution, the 1990 high D^0 momentum and the combined 1990 and 1991 tag analysis and d) for the 1991 low D^0 momentum solution and the 1991 high D^0 momentum solution.

We have to be careful computing σ_r. If we use the alternate fit technique, including all the uncertainties mentioned in the section "Quantities Used in the Fit", presumably we have accounted for the all the sources of extra error that we know *a priori*. If we use the more traditional method to fit, keeping a running tally of uncertainties mentioned in the section "Quantities Used in

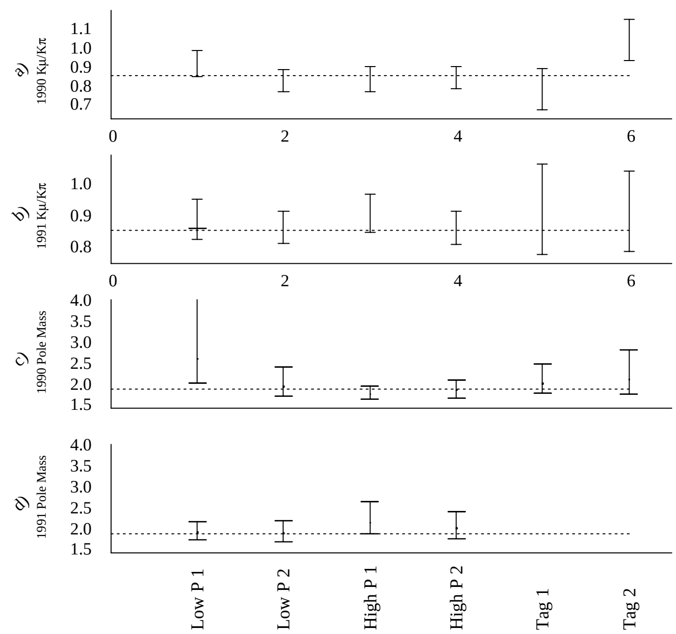

Figure 5.5.2 The $M(K\mu)$ split samples used for the systematic analysis. The description of the samples are as in Figure 5.5.1.

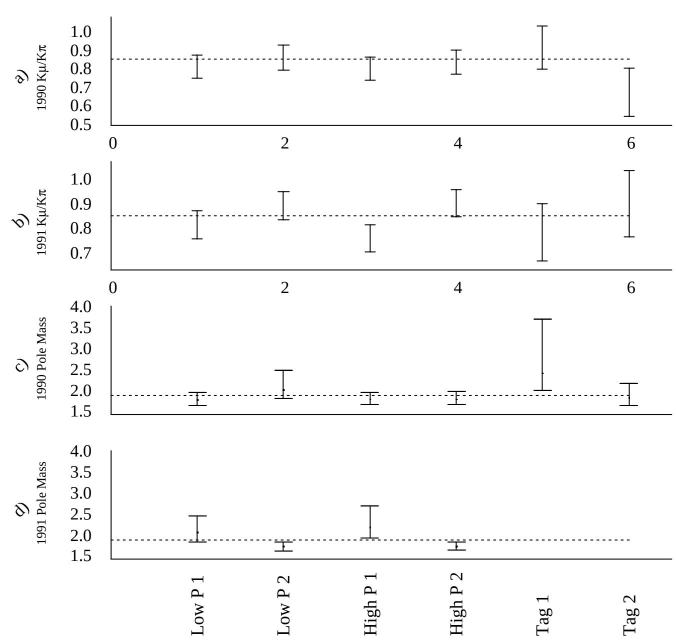

Figure 5.5.3 The DCL split samples used for the systematic analysis. The description of the samples are as in Figure 5.5.1.

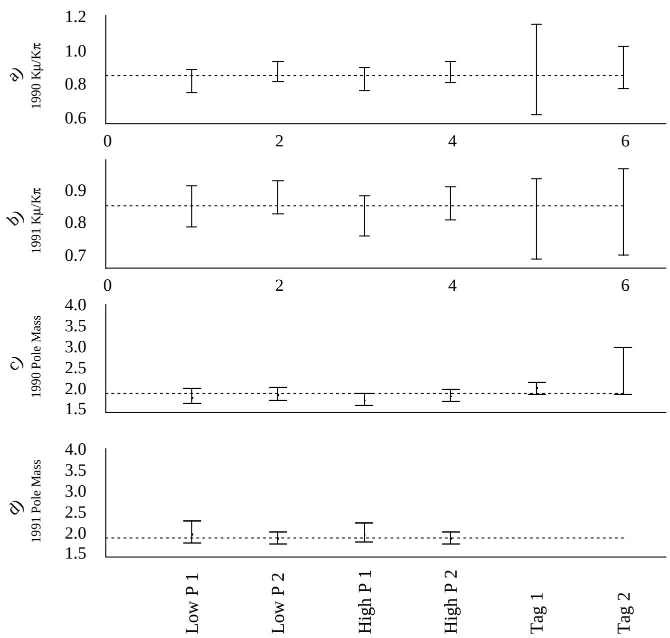

Figure 5.5.4 The $P(K)$ split samples used for the systematic analysis. The description of the samples are as in Figure 5.5.1.

the Fit" as a separate error, we modify σ_{sys} by

$$\sigma'_{sys} = \sqrt{\sigma^2_{sys} - \sum_{j=1}^{\#\ sources} \sigma^2_j}. \tag{5.5.4}$$

There is also the error associated with the fit. We have a technique for adding these shifts together as well. Basically, we assume the σ associated with each fit variant(v) is the same, and since the fit is an acceptable one as shown previously, we take $\chi^2 = \#\ fit\ variants\ (n) - 1$ and compute:

$$\sigma_{fit\ variant} = \sqrt{\frac{\sum_{k=1}^{n} {v_k}^2 - n < v >^2}{n-1}}. \tag{5.5.5}$$

We see no evidence for additional error in the branching ratio or the pole mass. Any variation in the low D^0 momentum solution used for the branching

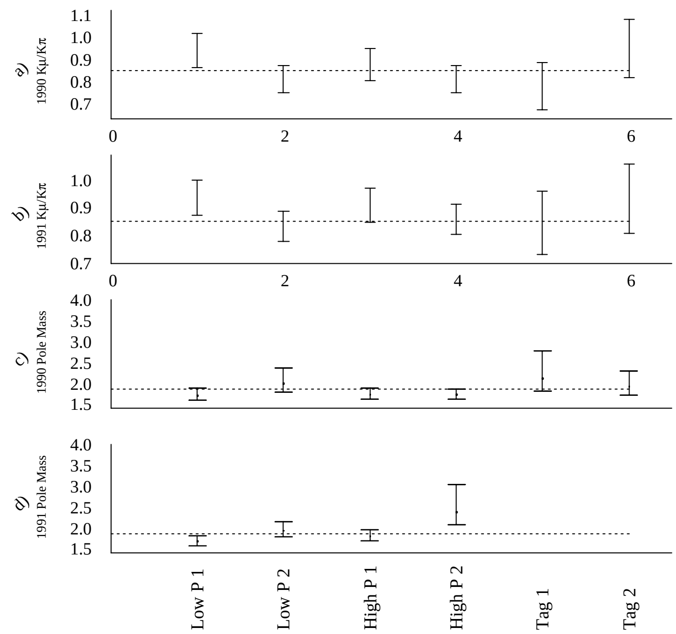

Figure 5.5.5 The $P(\mu)$ split samples used for the systematic analysis. The description of the samples are as in Figure 5.5.1.

ratio is not present in the high D^0 momentum solution result for the branching ratio, so we attribute these shifts to statistical fluctuations. The additional error seen in the high D^0 momentum solution result for the pole mass is due to a resolution effect, and since there is no evidence for additional error in the low D^0 momentum solution result for the pole mass, we attribute no additional error to this estimate. The tag analysis shows no evidence for additional error either.

We have combined all the sources of systematic error using the alternate fit method for the non–tag analysis in Table 5.5.2.

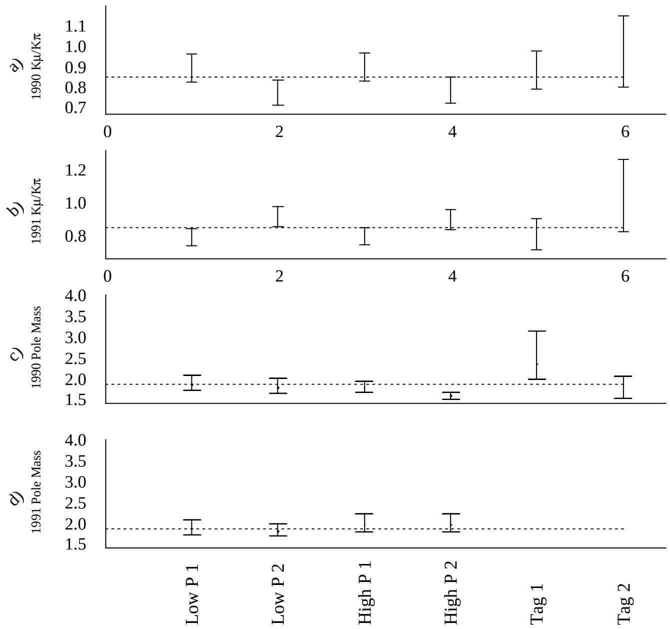

Figure 5.5.6 The total isolation split samples used for the systematic analysis. The description of the samples are as in Figure 5.5.1. Note that the apparent systematic in the branching ration in the low D^0 momentum solution is cancelled by the lack of a similar shift in the high D^0 momentum solution.

Table 5.5.2 Sources of Systematic Error

Systematic	δ_{sys}^{BR}	$\delta_{sys}^{M_p}$
Variation from split samples	± 0.0	± 0.0
$K^*\mu\nu(R_v, R_2)$	± 0.005	± 0.01
muon efficiency	± 0.017	± 0.0
Fit variation(from split samples)	± 0.013	$^{+0.066}_{-0.054}$
f_-/f_+ choice	± 0.017	± 0.01
Synthetic data test	± 0.0	± 0.0
TOTAL σ_{stat}	± 0.034	$^{+0.11}_{-0.08}$
TOTAL σ_{sys}	± 0.028	$^{+0.07}_{-0.06}$

5.6 Information and D^0 Momentum Solution Choice

We have some idea of the distribution of the decay daughters in the D^0 center of mass frame from the matrix element and the model of the form factor. The Cramer–Rao[54] inequality can be used to determine areas of high and low information density for measured quantities. Briefly, the minimum expected variance(Var_{min}) expected from measuring a quantity v distributed via the normalized probability distribution $P(x, v)$ for n events is:

$$\frac{1}{nVar_{min}} = \int \left(\frac{\partial P}{\partial v}\right)^2 \frac{1}{P} dx, \tag{5.6.1}$$

and by looking at the distribution:

$$Information\ density = \left(\frac{\partial P}{\partial v}\right)^2 \frac{1}{P} \tag{5.6.2}$$

we get an idea where the information used to measure the quantity, v, is located(try it on a Gaussian distribution!). For this analysis the probability distribution is the matrix element and form factor(Equation (1.5.7)), and the measured quantity is the pole mass. Thus, we look for the D^0 momentum solution that has the least inherent variance(best resolution) in the region of highest information density.

In Figure 5.6.1 we show the calculated M_{pole} information density, and in Figure 5.6.2 we show the resolution of each D^0 momentum solution for the cases when there are two solutions. We see substantial evidence that the correct solution choice for measuring M_{pole} is the low D^0 momentum solution.

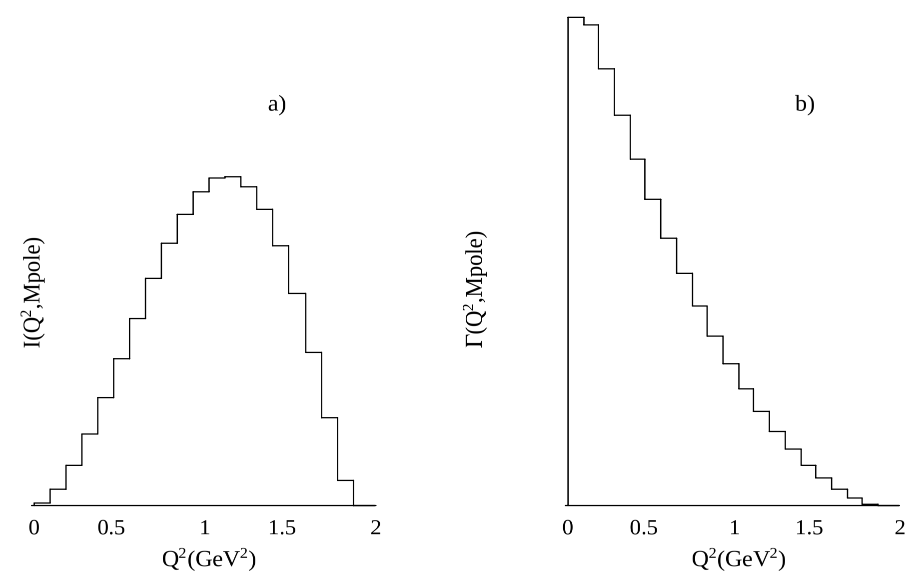

Figure 5.6.1 The information density for a) measuring M_{pole} using the distribution of generated events in q^2 and the matrix element with the form factor versus q^2 in b). Note the region of highest information density is between 0.9 GeV^2 and 1.6 GeV^2.

We can verify that these effects occur in the data by comparing the split sample M_{pole} estimates for the high and low D^0 momentum solutions. We see in Table 5.4.1 that a systematic error is indicated for the high momentum D^0 solution measurement of M_{pole}.

We have no similar *a–priori* expectations for the measurement of the yield, and we see no systematic contribution to the final branching ratio result using the high momentum D^0 solution.

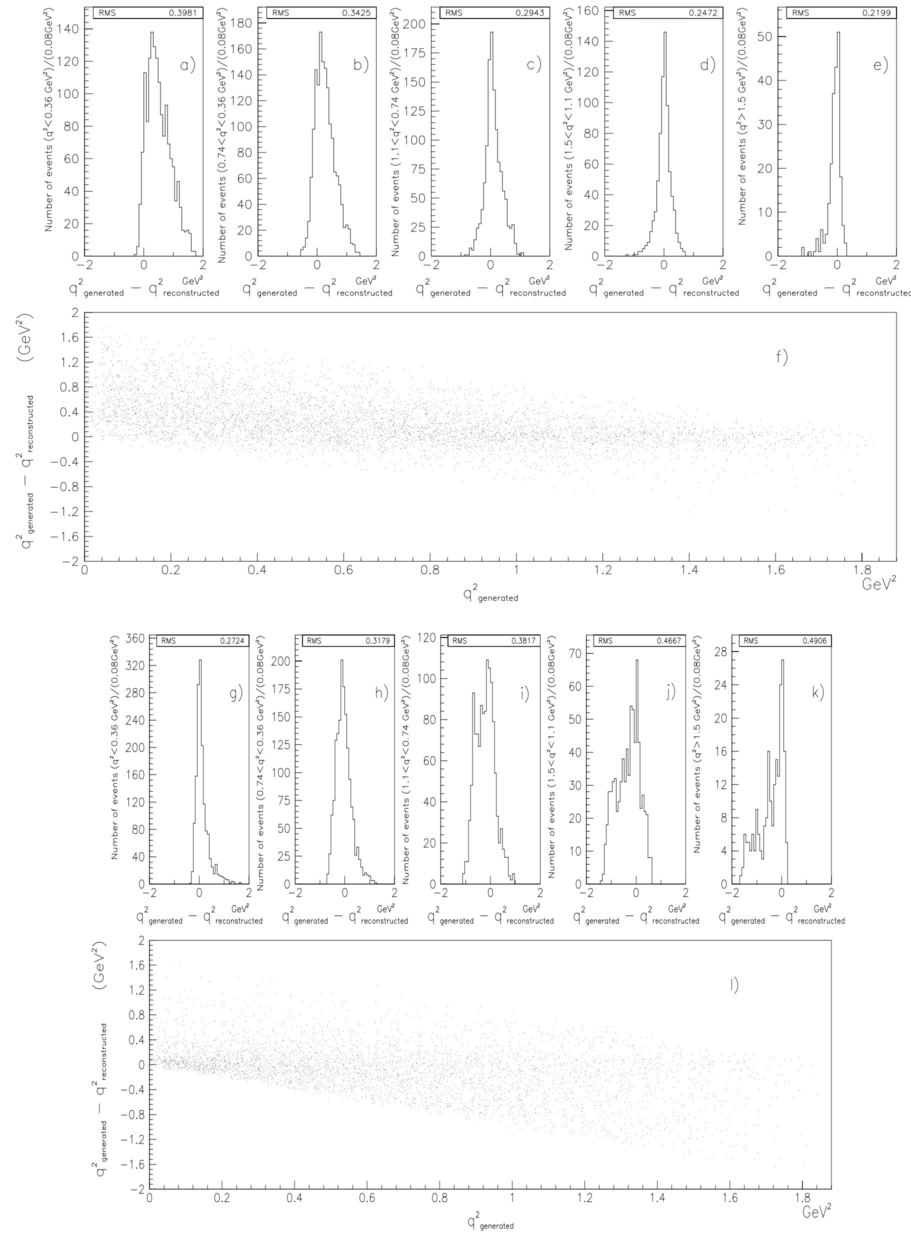

Figure 5.6.2 The behavior of the q^2 resolution for different cuts in generated q^2, a)–e) and g)–k), and versus generated q^2, f) and l), for the low D^0 momentum solution, a)–f), and the hi D^0 momentum solution, g)–k). Note that in each case the solution is unique(low momentum$\neq$ hi momentum), and that the low momentum solution has better resolution in the region of highest M_{pole} information density as shown in Figure 5.6.1. The boxed quantity above each cut plot is the r.m.s. spread of the q^2's in the plot.

5.7 The Systematic Error for $\frac{BR(D^0 \to K^{*-}\mu^+\nu_\mu)}{BR(D^0 \to K^-\mu^+\nu_\mu)}$

The error in this estimate is dominated by our measurement of the relative rates of $D^+ \to \overline{K}^0 \mu^+\nu_\mu$ and $D^+ \to K^-\pi^+\pi^+$. The method presented in the technique section will be useful when the 1991 data sample is added to our estimate. Since a 10% change in the ratio $\frac{BR(D^0 \to K^{*-}\mu^+\nu_\mu)}{(D^0 \to K^-\mu^+\nu_\mu)}$ results in a 1% change in $\frac{BR(D^0 \to K^-\mu^+\nu_\mu)}{(D^0 \to K^-\pi^+)}$, we quote a simple ratio neglecting any correlation present. Thus, the relative rates of $BR(D^0 \to K^{*-}\mu^+\nu_\mu)$ and $BR(D^0 \to K^-\mu^+\nu_\mu)$ has the same systematic error as does our measurement of $\frac{BR(D^0 \to K^-\mu^+\nu_\mu)}{(D^0 \to K^-\pi^+)}$.

In Figure 5.7.1 we show the variation of the measurement of $\frac{BR(D^0 \to K^{*-}\mu^+\nu_\mu)}{BR(D^0 \to K^-\mu^+\nu_\mu)}$ using the method outlined in the technique section. All shifts are due to variations in the parameter representing the $\frac{BR(D^0 \to K^{*-}\mu^+\nu_\mu)}{BR(D^0 \to K^-\pi^+)}$ used in the fit. Note that the error on this quantity is only slightly changed by a decrease of events in each split sample indicating that other quantities in the fit dominate the error.

5.8 The Systematic Error for f_-/f_+

We looked at the same split samples for this measurement that we used for the other measurements. We find that the tag sample gives the best result. There is a large systematic variation in $P\mu$ for the non–tag analysis that is presumably due to momentum dependence of the generated D^0. We also find that it is unnecessary to relax the cut in $M(K\mu)$ in the tag sample as the systematic error increases when we do so. The sample used for the systematic study was fit using the same method for the other systematic studies, and the majority of the known systematic error is reflected in the statistical error. The additional systematic error in both samples is estimated using the split samples and the fit variations among the split samples. Figure 5.8.1 is the

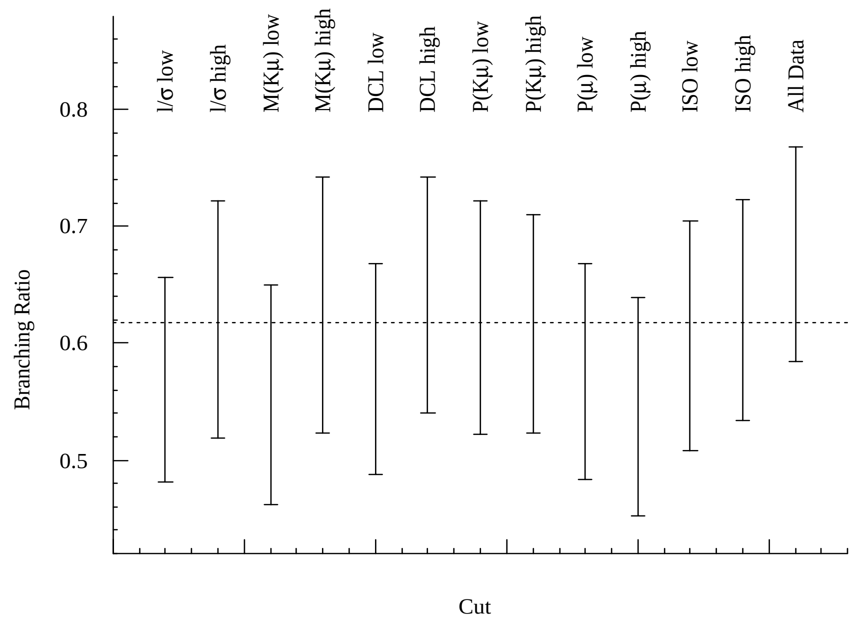

Figure 5.7.1 The variation of $\frac{BR(D^0 \to K^{*-}\mu^+\nu_\mu)}{(D^0 \to K^-\mu^+\nu_\mu)}$ with different cuts. Variations are due to shifts in the $\frac{BR(D^0 \to K^{*-}\mu^+\nu_\mu)}{(D^0 \to K^-\pi^+)}$ constraint used in the fit. Our final result is added to the plot as a dotted line. Notice that the error on each measurement changes little with each cut indicating that the error in this measurement is not sensitive to the fluctuations in our estimate of $\frac{BR(D^0 \to K^-\mu^+\nu_\mu)}{(D^0 \to K^-\pi^+)}$.

data used in the systematic study, and Table 5.8.1 is a summary of our result and error analysis.

We include a measurement of M_{pole} and f_-/f_+ fit simultaneously. Since f_- and M_{pole} have some degree of correlation, any variations in f_- transfer to M_{pole}(and likewise) and increase the uncertainty. In the tag sample, the error prohibits a meaningful estimate. In the non–tag sample we find that $M_{pole} = 2.16^{+0.63+0.25}_{-0.27-0.16}$ and $f_-/f_+ = 4.1 \pm 3.0 \pm 5.1$ when both are fit simultaneously.

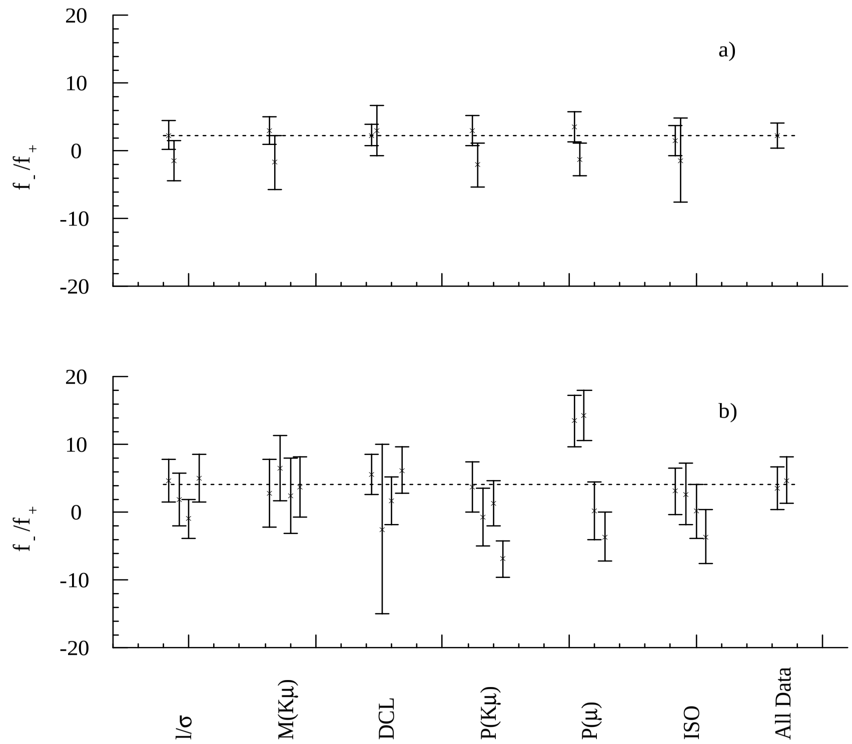

Figure 5.8.1 The variation of the f_-/f_+ measurements using different cuts for a), the tag(with $M(K\mu)$ mass cut) sample and b), the non–tag sample. The cuts separate the data into roughly half samples using the same cuts that were used for the branching ratio and M_{pole} measurements. Note that the tag sample is not separated into 1990 and 1991 samples. The result for each sample is included as a dotted line. The instability of the non–tag analysis for this quantity is apparent in b).

Table 5.8.1 f_-/f_+ Results

Sample	f_-/f_+	statistical error	systematic error
Tag($M(K\mu)$ mass cut)	2.3	±1.9	±1.8
Tag(no mass cut)	2.2	±2.0	±1.9
Non–Tag	4.2	±2.0	±5.0

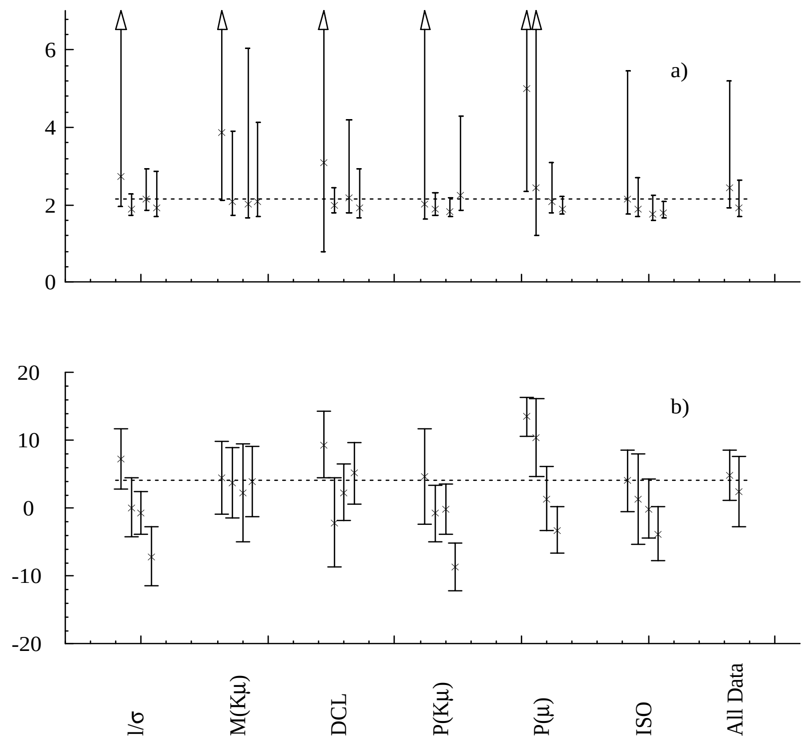

Figure 5.8.2 The variation of a), M_{pole}, and b), f_-/f_+, when both are fit simultaneously using the non–tag sample. As in Figure 5.8.1 the cuts separate the data into roughly half samples using the same cuts that were used for the branching ratio and previous M_{pole} measurements. The result for each sample is included as a dotted line. The instability of the f_-/f_+ measurement remains.

The systematic error is estimated as before(see Figure 5.8.2) using split sample variations. Note that this result is in agreement with our previous estimates of f_- and M_{pole}. The variation in the branching ratio for this measurement as compared to the value measured with $f_-/f_+ = 0$ is 1%. We do not include this variation in our measurement of branching ratios.

CHAPTER 6

CONCLUSIONS

We have analyzed the semimuonic charm decay channel $D^0 \to K^-\mu^+\nu_\mu$. The ratios $\frac{BR(D^0 \to K^-\mu^+\nu_\mu)}{BR(D^0 \to K^-\pi^+)}$ and $\frac{BR(D^0 \to K^{*-}\mu^+\nu_\mu)}{BR(D^0 \to K^-\mu^+\nu_\mu)}$, the ratio of form factors f_-/f_+ and the pole mass associated with this decay channel have been determined. Each result represents the world's best measurement.

6.1 Overview

The results from the analysis chapter and the systematics chapter are combined in this chapter. We have determined the relative rates of $D^0 \to K^-\mu^+\nu_\mu$ to $D^0 \to K^{*-}\mu^+\nu_\mu$ and of $D^0 \to K^-\mu^+\nu_\mu$ to $D^0 \to K^-\pi^+$. We also find the pole mass associated with the vector meson model and the strength of the $f_\pm$ form factors. The results are compared to other analyses and theory.

6.2 Final Results

We quote the final results(see Table 6.2.1) based on the fit used in the systematics chapter that includes the variations of measured quantities(see the Appendix) directly in the fit.

We combine our pole mass measurement, our branching ratio measurement, the expression for the rate , $(D^0 \to K^-\mu^+\nu_\mu))$, the CLEO[34] measurement of $BR(D^0 \to K^-\pi^+)$, the PDG[11] value of $V_{cs}(0.9745)$ and our measurement of the D^0 lifetime[28] to get estimates for $f_+(0)$ and , $(D^0 \to K^-\mu^+\nu_\mu)$.

Table 6.2.1 Final Results

Measured Quantity	Value	Statistical error	Systematic error
$\frac{BR(D^0 \to K^- \mu^+ \nu_\mu)}{BR(D^0 \to K^- \pi^+)}$	0.852	± 0.034	± 0.028
Pole Mass(M_{pole})	1.87 (GeV/c^2)	$^{+0.11}_{-0.08}$	$^{+0.07}_{-0.06}$
$\frac{BR(D^0 \to K^{*-} \mu^+ \nu_\mu)}{BR(D^0 \to K^- \mu^+ \nu_\mu)}$	0.62	± 0.11	± 0.02
f_- / f_+	2.3	± 1.9	± 1.8
, $(D^0 \to K^- \mu^+ \nu_\mu)$	$8.07(\times 10^{10}/sec.)$	± 0.52	± 0.27
$f_+(0)$	0.716	± 0.029	± 0.019

6.3 Comparison to other Experiments and Theory

Table 6.3.1 contains results from experiments. Note that the CLEO[56,23] results are combined electron and muon measurements except where noted. The measurement made in reference [57] is made by normalizing to the total inclusive rate instead of $D^0 \to K^- \pi^+$.

Table 6.3.1 Other Experiments

Reference	$\frac{BR(D^0 \to K^- l^+ \nu_l)}{BR(D^0 \to K^- \pi^+)}$	Pole Mass(M_{pole})	$\frac{BR(D^0 \to K^{*-} l^+ \nu_l)}{BR(D^0 \to K^- l^+ \nu_l)}$
[56](e, μ)	$0.79 \pm 0.08 \pm 0.09(\mu)$	$2.0^{+0.4+0.3}_{-0.2-0.2}$	$0.51 \pm 0.18 \pm .06$
[23](e, μ)	$0.978 \pm 0.027 \pm 0.044$	$2.00 \pm 0.12 \pm 0.18$	0.62 ± 0.08
[22](e)	$0.91 \pm 0.07 \pm 0.11$	$2.1^{+0.4}_{-0.2} \pm 0.2$	0.55 ± 0.14
[24](μ)	$0.82 \pm 0.13 \pm 0.13$	(–)	$0.59 \pm 0.10 \pm 0.13$

Reference	f_- / f_+	, $(D^0 \to K^- l^+ \nu_\mu) 10^{10}/sec$	$f_+(0)$
[56](e, μ)	(–)	(–)	$0.81 \pm 0.03 \pm 0.06$
[23](e, μ)	(–)	$9.1 \pm 0.3 \pm 0.6$	$0.77 \pm 0.01 \pm 0.04$
[22]e	(–)	$9.1 \pm 1.1 \pm 1.4$	$0.79 \pm 0.05 \pm 0.06$
[57](μ)	(–)	$5.6 \pm 0.9 \pm 1.2$	(–)

Table 6.3.2 contains estimates from theory. For the theory estimates, we requote some of the values from references [40] and [55]. Note that Amundson and Rosner[60] indicate that higher order corrections lower the theoretical estimates of $\frac{BR(D^0 \to K^{*-} l^+ \nu_l)}{BR(D^0 \to K^- l^+ \nu_l)}$.

Table 6.3.2 Theory Estimates

Reference	$f_+(0)$	f_-/f_+	$\frac{BR(D^0 \to K^{*-} l^+ \nu_l)}{BR(D^0 \to K^- l^+ \nu_l)}$
Simple Calculation(Chapter 1)	(–)	(-0.7)	(–)
[40]	0.90 ± 0.22	-1.2 ± 0.5	(–)
[44]	0.76	-0.46	0.87
[41, 42, 43]	0.77	-0.60	$1.34, 1.14$
[45,46]	0.76	-0.46	0.87
[58]	$0.56 \to 0.76$	$-.36 \to -1.07$	(–)
[59]	$0.6^{+0.15}_{-.10}$	(–)	0.5 ± 0.15

Our result for the branching ratio $\frac{BR(D^0 \to K^- \mu^+ \nu_\mu)}{BR(D^0 \to K^- \pi^+)}$ has comparable error to the world's best measurement of $\frac{BR(D^0 \to K^- e^+ \nu_e)}{BR(D^0 \to K^- \pi^+)}$.[23] Our pole mass measurement has better errors than the previous best measurement.[23] This is probably because the analysis in [23] has a substantially higher cut in $M(K\mu)$ which removes q^2 events from the region of high M_{pole} information density.

We see that our results for all quantities are in reasonable agreement with what is measured by other experiments. The possible exception is the difference between the two best measurements for $\frac{BR(D^0 \to K^- l^+ \nu_l)}{BR(D^0 \to K^- \pi^+)}$. Accounting for the expected difference[37] of 3% and including statistical and systematic errors, the difference is about 1.5σ. If we compare using statistical differences only and the expected difference of 3%, we see a difference of 2.3σ. More statistics are needed to determine if the difference, if any, is significant.

We confirm the low rate of $D^0 \to K^{*-}l^+\nu_l$ relative to $D^0 \to K^-l^+\nu_l$ seen by other experiments, but can make no other quantitative discrimination between theoretical models since either our error is too large(f_-), the error in theory is large,[40,58,59] or theory and experiment agree. We quote a 90% confidence level region for f_-/f_+ of $-2.0 < f_-/f_+ < 6.6$, which is agreement with theoretical predictions.

6.4 Final Remarks

We have demonstrated that analyzing the non–tag sample substantially increases our statistics with little loss in precision except for the measurement of f_-/f_+. Future experiments will either need a factor of 100 in statistics, a substantial decrease in the backgrounds, or better resolution to make a useful measurement of f_-/f_+.

Many of the contributions to systematic error in this measurement can be reduced in a future experiment or by further analysis. The muon system contributes the most systematic error to this analysis, and the easiest way to reduce this contribution is to return to the 1990 configuration of the inner muon system. The other large contributors to the systematic error, the ratio of production of D^+ and D^0 and the ratio $\frac{BR(D^+ \to K^{*0}\mu^+\nu_\mu)}{BR(D^+ \to K^-\pi^+\pi^+\pi^-)}$, can be reduced with an analysis of the entire E687 data set. It is clear that more data will help the results presented in this thesis, but more work is needed by other experiments to claim that their results are limited by statistics.

The next phase of Experiment E687, E831 plans a 40 fold increase in statistics with better resolution and less background. This analysis has laid the groundwork for the high precision measurement possible with that data, and the techniques described in this thesis will be useful for increasing the statistics of Cabibbo suppressed semimuonic decays like $D^0 \to \pi^-\mu^+\nu_\mu$ and for reanalyzing the decays $D^+ \to K^{*0}\mu^+\nu_\mu$ and $D^0 \to K^{*-}\mu^+\nu_\mu$.

REFERENCES

1. CDF Collaboration, F. Abe *et al.*, Phys. Rev. D **50**, 2966 (1994).

2. See R. Kronig and V. F. Weisskopf, eds., *Collected Scientific Papers by Wolfgang Pauli*, Vol. II, Wiley–Interscience, New York 1964, p. 1316.

3. E. Fermi, Z. Physik **88**, 161 (1934).

4. T. D. Lee and C. N. Yang, Phys. Rev. **104**, 254 (1956).

5. C. S. Wu, E. Ambler, R.W. Hayward, D. D. Hoppes, and R. P. Hudson, Phys. Rev. **105**, 1413 (1957).

6. H. Frauenfelder, R. Bobone, E. von Goeler, N. Levine, H. R. Lewis, R. N. Peacock, A. Rossi, and G. De Pasquali, Phys. Rev. **106**, 386 (1957).

7. M. Goldhaber, L. Grodzins, and A. W. Sunyar, Phys. Rev. **109**, 1015 (1958).

8. H. Yukawa, Proc. Phys. Math. Soc. Japan **17**, 48 (1935).

9. M. Gell–Mann, Phys. Letters **8**, 214(1964).

10. G. Zweig, CERN Report 8182/Th. 401 (1964) (unpublished).

11. Particle Data Group, K. Hikasa *et al.*, Phys. Rev. D **45**, No. 11, Pt. II (1992).

12. N. Cabibbo, Phys. Rev. Lett. **10**, 531 (1963).

13. M. Kobayashi and T. Maskawa, Prog. Theor. Phys. **49**, 652 (1973).

14. S. Gasiorowicz, *Elementary Particle Physics*, John Wiley and Sons, Inc. New York 1967, p. 569.

15. L. Jauneau, in *Methods in Subnuclear Physics*, ed. M. Nicolic, Gordon and Brach, New York 1969, p. 125.

16. P. L. Frabetti *et al.*, Nucl. Instr. and Meth. in Phys. Res., sect. A **320**, 519 (1992).

17. G. Alimonti *et al.*, Nucl. Instr. and Meth. in Phys. Res., sect. A **314**, 411 (1992).

18. C. J. Dallapiccola, Ph. D. Thesis, University of Colorado at Boulder, (1993) (uupublished).

19. Sjostrand, Torbjorn, Comp. Phys. Commun., **82**, 74 (1994).

20. T. Murphy *et al.*, Nucl. Instr. and Meth. in Phys. Res., sect. A **251**, 478 (1986).

21. J. E. B. O' Reilly, Private Communication, (1994).

22. E691 Collab., J. C. Anjos *et al.*, Phys. Rev. Lett. **62**, 1587 (1989).

23. CLEO Collab., A. Bean *et al.*, Phys. Lett. **B317**, 647 (1993).

24. E687 Collab., P. L. Frabetti *et al.*, Phys. Lett. **B315**, 203 (1993).

25. E687 Collab., P. L. Frabetti *et al.*, Phys. Lett. **B313**, 253 (1993).

26. R. Culbertson and J. Wiss, *R_v and R_2 Systematics Studies*, E687 internal memo, (1993) (unpublished).

27. R. Culbertson, Ph. D. Thesis, University of Illinois at Urbana–Champaign, (1993) (unpublished).

28. E687 Collab., P. L. Frabetti *et al.*, Phys. Lett. **B323**, 459 (1994).

29. E687 Collab., P. L. Frabetti *et al.*, Phys. Rev. Lett. **71**, 827 (1993).

30. G. Jaross, Ph. D. Thesis, University of Illinois at Urbana–Champaign, (1991) (unpublished).

31. F. James and M. Roos, Computer Physics Commun. 10, 343 (1975).

32. E687 Collab., P. L. Frabetti *et al.*, Phys. Lett. **B307**, 262 (1993).

33. CLEO Collab., R. Balest *et al.*, Phys. Rev. Lett. **72**, 2328 (1994).

34. CLEO Collab., D. S. Akerib *et al.*, Phys. Rev. Lett. **71**, 3070 (1993).

35. E687 Collab., P. L. Frabetti *et al.*, Phys. Lett. **B308**, 193 (1993).

36. E691 Collab., J. C. Anjos *et al.*, Phys. Rev. Lett. **67**, 1507 (1991).

37. J. G. Körner and G. A. Schuler, Z. Physik **C46**, 93 (1990).

38. E653 Collab., K. Kodama *et al.*, Phys. Lett. **B286**, 187 (1992).

39. E653 Collab., K. Kodama *et al.*, Phys. Lett. **B309**, 483 (1993).

40. C. W. Bernard, A. X. El–Khadra and A. Soni, Phys. Rev. **D43**, 2140 (1991).

41. B. Grinstein, N. Isgur, D. Scora and M. Wise, Phys. Rev. **D39**, 799 (1989).

42. T. Altomari and L. Wolfenstein, Phys. Rev. Lett. **58**, 1583 (1987).

43. T. Altomari and L. Wolfenstein, Phys. Rev. **D37**, 681 (1988).

44. M. Bauer, B. Stech and M. Wirbel, Z. Phys. C **29**, 637 (1985).

45. J. G. Körner and G. A. Schuler, Z. Phys. C **38**, 511 (1988).

46. J. G. Körner and G. A. Schuler, Phys. Lett. B **231**, 306 (1989).

47. E691 Collab., J. C. Anjos *et al.*, Phys. Rev. **D45** R2177 (1992).

48. E653 Collab., K. Kodama *et al.*, Phys. Lett. **B313**, 260 (1993).

49. Particle Data Group, L. Montanet *et al.*, Phys. Rev. D **50**, No. 3, Pt. I (1994).

50. R. Culbertson, $PostHocNoMore?$,E687 internal memo, (1994) (unpublished).

51. Steve Culy, Private Communication, (1992).

52. Jim Wiss, Private Communication, (1994).

53. E687 Collab., P. L. Frabetti *et al.* *“Techniques for the Resonance Analysis of Three Body D Meson Decays”*, to be submitted to Nucl. Instr. and Meth. in Phys. Res., sect. A.

54. See Hoel, Paul, G. *Introduction to Mathematical Statistics*, John Wiley and Sons, Inc. New York 1971, p. 362.

55. S. Stone, in *Heavy Flavors*, edited by A. J. Buras and H. Linder, World Scientific, Singapore 1992, p. 334.

56. CLEO Collab., G. Crawford *et al.*, Phys. Rev. D **44**, 3394 (1991).

57. E653 Collab., K. Kodama *et al.*, Phys. Rev. Lett. **66**, 1819 (1991).

58. R. Gupta, T, Bhattacharya and D.Daniel (Los Alamos), LA–UR–93–3580, Oct. (1993)

59. P. Ball, V. M. Braun and H.G. Dosch, Phys. Rev. D **44**, 3567 (1991)

60. J. F. Amundson and J. L. Rosner, Phys. Rev. D **47**, 1951 (1993)

APPENDIX A

Table A.1 is a list of quantities determined for this thesis, and Table A.2 is a list of other measurements used in this analysis.

Table A.1 Quantites Determined for this Analysis

Quantity	Value(1990/1991)	Reference
$D^0 \to K^-\mu^+\nu_\mu$ efficiency tag	0.0121/0.00597	this thesis
$D^0 \to K^-\mu^+\nu_\mu$ efficiency non–tag	0.0149/0.00823	this thesis
$D^0 \to K^-\pi^+$ efficiency tag	0.02346/0.02125	this thesis
$D^0 \to K^-\pi^+$ efficiency non–tag	0.02715/0.02446	this thesis
$D^0 \to K^-\mu^+\nu_\mu$ yield tag	194.5/231.7	this thesis
$D^0 \to K^-\mu^+\nu_\mu$ yield non–tag	797.0/1099.8	this thesis
$D^0 \to K^-\pi^+$ yield tag	446.3/971.5	this thesis
$D^0 \to K^-\pi^+$ yield non–tag	1719.7/3821.5	this thesis
$D^0 \to K^-\mu^+\nu_\mu$ δyield$_{statistical}$ tag	16.3/22.1	this thesis
$D^0 \to K^-\mu^+\nu_\mu$ δyield$_{statistical}$ non–tag	38.5/50.0	this thesis
$D^0 \to K^-\pi^+$ δyield$_{statistical}$ tag	21.0/33.6	this thesis
$D^0 \to K^-\pi^+$ δyield$_{statistical}$ non–tag	57.7/86.1	this thesis

Table A.2 Quantites Used in this Analysis

Quantity	Value	Reference
$\frac{BR(D^0 \to K^{*-}\mu^+\nu_\mu)}{BR(D^0 \to K^-\mu^+\nu_\mu)}$	0.60 ± 0.06	[32,23,36]
$\frac{\Gamma(D^+ \to K^{*0}\mu^+\nu_\mu)}{\Gamma(D_s^+ \to K^-\mu^+\nu_\mu)}$	1.11 ± 0.13	[25]
M_{pole}(for f_-/f_+)	2.0 ± 0.22	[23]
$\frac{Production(D^+)}{Production(D^0)}$	0.42 ± 0.05	[30]
D^+ lifetime	1.048 ± 0.019	[28]
D^0 lifetime	0.413 ± 0.005	[28]
D_s^+ lifetime	0.475 ± 0.021	[29]
R_v for $D^+ \to K^{*-}\mu^+\nu_\mu$ simulation	1.88 ± 0.27	[32, 32]
R_2 for $D^+ \to K^{*-}\mu^+\nu_\mu$ simulation	0.80 ± 0.16	[32, 32]
Particle Masses except where fitted for	GeV/c^2	[11]
$D^+ \to K^{*0}\mu^+\nu_\mu$ yield (for D_s^+ Prod.)	302 ± 26	[26]
$D^+ \to K^{*0}\mu^+\nu_\mu$ efficiency (for D_s^+ Prod.)	0.02237	[27]
$D_s^+ \to \phi\mu^+\nu_\mu$ yield (for D_s^+ Prod.)	44 ± 9	[27]
$D_s^+ \to \phi\mu^+\nu_\mu$ efficiency (for D_s^+ Prod.)	0.02595	[27]
$BR(D^+ \to K^-\pi^+\pi^+\pi^-)$	0.093 ± 0.01	[33]
$BR(D^0 \to K^-\pi^+)$	0.0391 ± 0.0019	[34]

ERRATA

In Table 5.4.1 note that the following quantity is amended:

Errata Table 5.4.1 Comparison of Techniques, $D*$ and Non–$D*$ Analyses

Measurement	$D*$
$\frac{BR(D^0 \to K^- \mu^+ \nu_\mu)}{BR(D^0 \to K^- \pi^+)}$	$0.84 \pm 0.06 \pm 0.03$

This is a calculational mistake.

In Table 6.2.1 note that the following quantity is amended:

Errata Table 6.2.1 Final Results

Measured Quantity	Value	Statistical error	Systematic error
$f_+(0)$	0.71	± 0.03	± 0.02

The integral of the rate expression was originally done with $f_-/f_+ = -1$, but since the standard measurement is made with $f_-/f_+ = 0$, we amend this final result accordingly.